UNIVERSIDADE DE LISBOA

Faculdade de Medicina de Lisboa

Cortico-hippocampal interactions as a neural substrate for the retrieval of contextual memories in choice behavior

Emanuel Ferreira Fernandes

Orientador: Professor Doutor Armando Miguel Caseiro Pires Remondes

Tese especialmente elaborada para obtenção do grau de Doutor em Ciências Biomédicas, Especialidade em Neurociências

2020

UNIVERSIDADE DE LISBOA

Faculdade de Medicina de Lisboa

Cortico-hippocampal interactions as a neural substrate for the retrieval of contextual memories in choice behavior

Emanuel Ferreira Fernandes

Orientador: Professor Doutor Armando Miguel Caseiro Pires Remondes

Tese especialmente elaborada para obtenção do grau de Doutor em Ciências Biomédicas, Especialidade em Neurociências

Júri: Presidente: Doutor João Eurico Cortez Cabral da Fonseca, Professor Catedrático e Vice-Presidente do Conselho Científico da Faculdade de Medicina da Universidade de Lisboa

Vogais: Doctor Valerie Ego-Stengel, Investigador no Paris-Saclay Institute of Neurosciences da Université Paris-Saclay;

Doutor João Miguel Peça Lima Novo Silvestre, Investigador Principal do Centro de Neurociências e Biologia Celular da Universidade de Coimbra;

Doutora Ana Maria Ferreira de Sousa Sebastião, Professora Catedrática da Faculdade de Medicina da Universidade de Lisboa;

Doutor Alexandre Valério de Mendonça, Professor Catedrático Convidado da Faculdade de Medicina da Universidade de Lisboa;

Doutora Luísa Maria Vaqueiro Lopes, Professora Associada Convidada da Faculdade de Medicina da Universidade de Lisboa;

Doutor Armando Miguel Caseiro Pires Remondes, Professor Auxiliar Convidado da Faculdade de Medicina da Universidade de Lisboa.

Instituição Financiadora: Fundação para a Ciência e Tecnologia PD/BD/105843/2014

2020

A impressão desta tese foi aprovada pelo Conselho Científico da Faculdade de Medicina de Lisboa em reunião de 19 de Fevereiro de 2019.

As opiniões expressas nesta publicação são da exclusiva responsabilidade do seu autor.

The experimental work herein described was performed at Instituto de Medicina Molecular João Lobo Antunes – Faculdade de Medicina da Universidade de Lisboa, under the supervision of Armando Miguel Caseiro Pires Remondes, DVM Ph.D.

“I was born not knowing and have had only a little time to change that here and there”

Richard Feynman

ABSTRACT

Spatial working memory, the retention and use of behaviorally relevant spatial cues on a timescale of seconds, depends on complex, finely tuned interactions between hippocampus and the cortical regions anterior cingulate (ACC) and retrosplenial cortices (RSC), together hereby named medial mesocortex (MMC). In this circuit, the processing of hippocampal contextual information is hypothesized to follow a directional stream, from hippocampus to cortex, providing depolarizing drive to MMC neurons. The functional circuitry underlying these interactions and the necessity of such interactions for spatial working memory have not been established.

Using retrograde and anterograde tracings, we reported the existence of a HIPP-MMC monosynaptic connection, and we characterized its topographic organization along the MMC. ACC is mainly targeted by the *stratum pyramidale* of dorso-intermediate HIPP (diHIPP), whereas RSC is targeted by pyramidal and non-pyramidal *strata* of diHIPP. In RSC, the hippocampal projection includes long-range GABAergic cells located at the border between *stratum radiatum* and *stratum lacunosum-moleculare*. Glutamatergic axons arising from diHIPP show sparse distribution and do not show preference for specific layers in the ACC. Contrarily, the glutamatergic axons arising from diHIPP project heavily to the superficial layers of RSC, particularly to layers 3 and 4, whereas the long-range GABAergic cells targeting RSC project mainly to layer 1.

Using optogenetics, *in vitro* electrophysiology and sequential pharmacology, we showed that such hippocampal projections establish *bona fide* synapses throughout MMC cortical layers, and their differential targeting of ACC and RSC translates into a functional dichotomy at the microcircuit level. Specifically, the diffuse and excitatory hippocampal inputs to ACC evoke stronger potentials around layer 5, known for harboring large pyramids projecting descending axons to the basal ganglia, whereas the excitatory and inhibitory hippocampal inputs to RSC evoke stronger potentials in superficial layers (L1-3), where RSC sends and receives most corticocortical connections.

By using *in vivo* multi-site recordings, we further showed that the spontaneous activity patterns in the HIPP and MMC of the awake-behaving rat follow what would be expected from the above-described connectivity. First, epochs of increased spiking from HIPP are accompanied by short-term increases in MMC areas, with increased levels generally

preceding and following the trigger point, which is indicative of complex time-dependent cross-talk between these regions. Second, such increases are somewhat clearer in the anteriormost regions of MMC, implying that the presence of inhibitory in parallel with excitatory HIPP inputs to RSC modulates the cortical response *in vivo* in ways yet unexplored. Our data also showed that MMC spiking responses to HIPP have an oscillatory component, favoring frequencies known to play a significant role in hippocampal-cortical functions, and the strength of the oscillatory alignment to the HIPP rhythms increases as we move caudally along the MMC divisions, with the posteriormost RSC regions significantly more engaged to the hippocampal oscillations, under general wakefulness conditions.

Our findings established the functional circuitry supporting HIPP-MMC interactions, and uncovered an underlying gradient of hippocampal inputs to the MMC. The intimate connection between RSC and HIPP, whereupon RSC receives inputs from all HIPP layers, excitatory and inhibitory, and shows increased hippocampal entrainment, is consistent with the known functional similarity of RSC and HIPP. ACC, on the other hand, receives diffuse, sparse and exclusively excitatory input from HIPP and the stronger potentials are evoked in layer 5, known to project to the basal ganglia, consistent with its role in behavior control.

Key words: Hippocampus, Medial Mesocortex, Anatomical Tracing, Electrophysiology, Spatial Working Memory

RESUMO

A memória de trabalho espacial, que consiste na retenção e manipulação de informação espacial por curtos períodos de tempo, tipicamente por períodos de segundos, é uma capacidade fundamental para a realização de comportamentos adaptativos. Uma vez que a memória de trabalho espacial é assegurada por diversas regiões cerebrais interligadas, que interagem em diferentes escalas temporais, o circuito funcional que suporta a memória de trabalho espacial permanece pouco esclarecido. Estudos anteriores sugerem, contudo, o envolvimento do hipocampo e dos córtices cingulado anterior (ACC) e retrosplénico (RSC), designados coletivamente como mesocórtex medial. A interação entre o hipocampo e as regiões do mesocórtex medial foi, de facto, reportada durante a execução de tarefas, que envolveram a memória de trabalho espacial, em diversos estudos com roedores, e lesões no hipocampo ou mesocórtex medial em roedores traduzem-se numa diminuição do seu desempenho nessas tarefas comportamentais. A hipótese dominante sugere, pois, que a memória de trabalho espacial requer fluxo direcional de informação contextual do hipocampo para o córtex e que o hipocampo atua como *driver* da despolarização dos neurónios do mesocórtex medial. O circuito funcional que suporta esta interação e a necessidade da mesma para a memória de trabalho espacial permanecem, contudo, por estabelecer.

Através de técnicas de *tracing* retrógrado e anterógrado, demonstrámos a existência de uma conexão monossináptica entre o hipocampo e o mesocórtex medial e caracterizámos a sua organização topológica. Os nossos resultados suportam a noção de proximidades funcionais distintas entre o hipocampo e o RSC ou ACC. Embora todo o mesocórtex medial receba *input* monossináptico do hipocampo, cada divisão (RSC ou ACC) recebe um *input* distinto e com uma distribuição laminar específica. A projeção do hipocampo para o RSC inclui axónios glutamatérgicos provenientes de neurónios piramidais e não-piramidais, que convergem para as camadas superficiais (1-4) do RSC, e axónios GABAérgicos, provenientes de neurónios inibitórios de projeção longa localizados na fronteira entre o *stratum radiatum* e o *stratum lacunosum-moleculare* do hipocampo dorso-intermédio, que convergem para a camada 1 do RSC. A projeção densa do hipocampo para o RSC, com origem em todos os *strata* do hipocampo, é consistente com a sua interdependência funcional e propriedades de codificação, já que os neurónios do

RSC alteram o seu padrão de atividade em caso de lesão no hipocampo, pois respondem a variáveis visuais-espaciais e apresentam seletividade espacial semelhante aos neurónios do hipocampo. Contrariamente ao RSC, a projeção do hipocampo para o ACC é difusa, não convergindo para camadas corticais específicas, e apenas inclui axónios glutamatérgicos com origem em neurónios piramidais do hipocampo dorso-intermédio, cujo principal correlato comportamental é a posição do animal no espaço, necessária para o controlo executivo e para a codificação da representação interna da tarefa (*task space*). Através do recurso a eletrofisiologia *in vitro* (MEA2100®) combinada com optogenética e farmacologia sequencial, isolámos respostas sinápticas significativas em todas as divisões do mesocórtex medial em resultado da estimulação dos terminais do hipocampo, e descobrimos que as respostas são sensíveis a inibidores seletivos dos canais AMPA, NMDA e $GABA_A$, comportando-se como sinapses funcionais e fidedignas. A distribuição anatómica das respostas eletrofisiológicas no mesocórtex medial mostrou-se consistente com a distribuição anatómica das projeções do hipocampo acima descrita. Estes resultados fornecem nova evidência para uma velha controvérsia. Estudos anteriores sugerem a ausência de *input* do hipocampo dorsal para o ACC, outros a sua presença, e alguns autores reportam que a maioria das projeções do hipocampo para o RSC têm origem no subículo dorsal ou em neurónios na fronteira entre o subículo e CA1. Através da análise sistemática da conectividade entre o hipocampo e o mesocórtex medial, apresentámos a primeira análise quantitativa do *input* do hipocampo para as divisões do mesocórtex medial. Os nossos resultados demonstram que o hipocampo e o mesocórtex medial estão efetivamente ligados de forma direta por uma população de neurónios do hipocampo dorso-intermédio, seguindo um gradiente póstero-anterior, através do qual uma projeção densa, dupla (excitatória e inibitória) e direcionada para camadas corticais específicas é convertida progressivamente numa projeção esparsa, excitatória e difusa. Estas observações sugerem que a atividade do hipocampo informa o ACC e o RSC em diferentes fases. O RSC recebe *input* do hipocampo proveniente de múltiplos *strata* direcionado para as camadas superficiais (1-4), camadas em que o RSC recebe e envia a maioria das projeções córtico-corticais, enquanto o ACC recebe *input* exclusivamente de neurónios piramidais e estes evocam respostas de maior amplitude na camada 5, composta por neurónios piramidais que enviam axónios descendentes para o estriado e

outras estruturas subcorticais, em acordo com a função executiva e de controlo comportamental imputada ao ACC.

Através de registos eletrofisiológicos *in vivo*, mostrámos, por fim, que os padrões de atividade espontânea no hipocampo e mesocórtex medial em ratos não restringidos são consistentes com a conectividade acima descrita. Períodos com maior frequência de potenciais de ação no hipocampo são acompanhados por aumentos de curta duração na frequência de potenciais de ação nas divisões do mesocórtex medial. Dado que o aumento da atividade no mesocórtex medial antecede e sucede o aumento da atividade no hipocampo, este resultado sugere uma comunicação temporalmente complexa entre as duas regiões. Adicionalmente, o aumento da frequência de potenciais de ação descrito é mais evidente nas porções anteriores do mesocórtex medial, o que sugere que a presença de projeções inibitórias exclusivamente entre o hipocampo e o RSC têm um efeito modulatório *in vivo*. Finalmente, as respostas do mesocórtex medial ao hipocampo apresentam uma componente oscilatória, favorecendo frequências que desempenham um papel significativo nas interações hipocampo-corticais. Contrariamente ao aumento da frequência de potenciais de ação no mesocórtex medial, desencadeado pela atividade do hipocampo, o alinhamento entre as oscilações do mesocórtex medial e os ritmos do hipocampo aumenta gradualmente ao longo das divisões do mesocórtex medial, atingindo a maior coerência no RSC. Esta observação é consistente com o facto de o RSC receber um *input* denso do hipocampo, que inclui axónios excitatórios e inibitórios e, esta é especialmente relevante uma vez que as projeções inibitórias têm sido consideradas os principais efectores das oscilações gama e da sincronização dos ritmos gama entre áreas cerebrais distantes, ambos reportados em tarefas comportamentais que requerem memória de trabalho espacial.

O presente trabalho estabelece, desta forma, o circuito funcional que suporta a interação entre o hipocampo e o mesocórtex medial, tendo revelado um gradiente estrutural e funcional subjacente a esse circuito. O RSC recebe uma projeção densa, dupla (excitatória e inibitória) e proveniente de todas as camadas do hipocampo, que se traduz numa maior coerência entre as oscilações do RSC e os ritmos do hipocampo. Estas observações sugerem uma proximidade funcional entre o RSC e o hipocampo, participando ambos no processamento de informação contextual para auxiliar à navegação espacial. O ACC, por outro lado, recebe uma projeção esparsa, exclusivamente excitatória e proveniente do

stratum pyramidale, que evoca potenciais de maior amplitude na camada 5. Atendendo a que a camada 5 é conhecida por enviar projeções descendentes para os gânglios da base, estas observações são consistentes com a função de controlo executivo e inibição de respostas habituais imputada ao ACC.

Palavras-chave: Hipocampo, Mesocórtex Medial, *Tracing* Anatómico, Eletrofisiologia, Memória de Trabalho Espacial

PUBLICATIONS RELATED TO THIS DISSERTATION

- **Ferreira-Fernandes**, E., Pinto-Correia, B., Quintino, C., Remondes, M., 2019. **A gradient of hippocampal inputs to the the medial mesocortex.** *Cell Reports*, 29(10), pp.3266-3279.e3.

Table of Contents

ABBREVIATIONS LIST

AAV - adeno-associated virus

ACC - anterior cingulate cortex

aCSF - artificial cerebrospinal fluid

BSA - bovine serum albumin

CG - cingulate cortex

CNO - clozapine N-oxide

CTB - Cholera Toxin β-subunit

DG - dentate gyrus

DGAV - Direcção-Geral de Alimentação e Veterinária

DNMTP - delayed non-matching-to-place

DPSS - diode-pumped solid-state

DREADD - design receptors exclusively activated by designer drugs

hChR2 – human channelrodhopsin-2

HIPP - hippocampus

ISI - inter-stimulus interval

LATB - labeled axons with terminal boutons

LFP - local field potential

LRIP - long-range inhibitory projecting

MCC – midcingulate cortex

MEA - multi-electrode array

MMC - medial mesocortex

MUA – multi-unit activity

PBS - phosphate buffered saline

PFA - paraformaldehyde

PHA-L - *Phaseolus vulgaris*-leucoagglutinin

Pyr - pyramidal

REM - rapid eye movement

RS - rabbit serum

RSC - retrosplenial cortex

RT - room temperature

SCT - subiculo-cingulate tract

SL - *stratum lacunosum*

SM - *stratum moleculare*

SO - *stratum oriens*

SP - *stratum pyramidale*

SR - *stratum radiatum*

SWM - Spatial working memory

SWR - sharp-wave ripples

TiN - titanium nitride

UNC - University of North Carolina

I

Introduction

I. INTRODUCTION

"The question I am going to discuss is the very straightforward and specific one of "why rats turn the way they do, at a given choice-point in a given maze at a given stage of learning."

Edward Tolman *in* The Determiners of Behavior at a Choice Point

Imagine yourself in a familiar city, looking for a particular shop you never visited before. You naturally ask someone for directions. A person approaches you and says "Oh! To go to that shop you should continue in this street. Don't turn in the first crossing. In the second crossing, you should turn left. After fifty meters you will find another crossing. There, you should turn right. The shop you are looking for is the third building on your left side, near the entrance for the subway." While you walk, you keep rehearsing the instructions, and make your turns accordingly. Eventually, you end up finding the shop, as long as you don't forget any piece of information. Interestingly, once you accomplish the task, you might or might not remember those instructions latter. While moments like this might be common in our lives, it is remarkable (and poorly understood) how we encode, maintain, and use such instructions to guide our actions, for a short-period of time, in attempting to reach a goal. Experts would say we used working memory to support goal-directed behaviors. It is also remarkable that we have a (more or less complete) mental image of that familiar city, so we can plan ways of reaching specific locations. Experts would say we have a cognitive map of the city that we can use to assist goal-directed behaviors.

"They turn the way they do because they have on the preceding trials met this same choice-point together with such and such further objects or situations, down the one path and down the other, for such and such a number of preceding trials."

Edward Tolman *in* The Determiners of Behavior at a Choice Point

While it is well accepted that memory guides most of our choices, the neural mechanism by which memory is used during spatial navigation remains unknown. This dissertation aims, therefore, at increasing the understanding of the neural mechanism by which spatial memory is used at the service of goal-directed behaviors. More specifically, the core hypothesis of this work is that the interaction between the hippocampus (HIPP) and the cingulate (CG) and retrosplenial (RSC) cortices, collectively referred as medial mesocortex (MMC), is necessary to support the use of spatial working memory during spatial navigation in the rat. This hypothesis leads to 4 major predictions:

1. There should be hippocampal monosynaptic projections targeting the divisions of the MMC.
2. The hippocampal projections should be functional, evoking post-synaptic potentials in the divisions of the MMC.
3. The neural activity in the HIPP should be correlated with the neural activity in the divisions of the MMC *in vivo*, in a delayed non-matching-to-place (DNMTP) task.
4. The inhibition of the hippocampal projections targeting the divisions of the MMC should impair the performance in a DNMTP task.

Previous studies have already provided data that define the current state of the art of each prediction. In the next 3 sections, I will review such studies and all the background information necessary to understand each prediction, its implications and gaps. Section 1 contains an anatomical description of the HIPP and MMC, and a systematic review of the papers testing the HIPP-MCC structural connectivity, that should be considered before testing Prediction 1. Section 2 contains a functional description of the HIPP-MMC interaction, at the microcircuit level, built upon data from *in vitro* electrophysiology and *in vivo* electrophysiology in the anesthetized rat. These should be considered before testing Prediction 2. Section 3 contains a functional description of the HIPP and MMC in the context of memory, spatial navigation, and goal-directed behavior, using data from *in vivo* electrophysiology in freely-behaving rats. This constitutes the background of Predictions 3 and 4. Each section finishes with the identification of the gaps that led to the research questions and aims of this dissertation.

1. SECTION 1 - THE HIPP-MMC INTERACTION AT THE ANATOMICAL LEVEL

Previous studies reviewed in this section tested the HIPP-MMC structural connectivity, providing evidence of monosynaptic connections between the HIPP and the divisions of the MMC. These connections also seem to display a topographical gradient depending on the specific area of the MMC targeted by the HIPP. These studies were, however, unsystematic, as they dissected the connectivity of each division of the MMC independently, and they were exclusively qualitative. To address these problems, the present dissertation aims at 1) comparing the laminar distribution of the hippocampal populations projecting to the divisions of the MMC; 2) quantifying the hippocampal populations projecting to the divisions of the MMC; 3) comparing the laminar distribution of the hippocampal axons in the divisions of the MMC; and 4) quantifying the hippocampal axons in the divisions of the MMC.

1.1. THE ANATOMY OF THE HIPP

The rat HIPP is an allocortical formation composed by distinct, but closely related brain regions that form a functional system. While there are differences in the literature regarding the exact regions that are considered as part of the HIPP, most of the authors call HIPP the group of brain regions that includes the dentate gyrus (DG), the HIPP proper, and the subiculum. The HIPP proper is further divided in three fields, namely CA1, CA2, and CA3 (to review the hippocampal anatomy, see (Amaral & Witter 1989; Andersen 2007)). The three-dimensional position of the rat HIPP is illustrated in Figure 1. The rostral portion is flanked by the septal nuclei, and the caudal and ventral portions are flanked by the temporal lobe (Amaral & Witter 1989). Morphological, functional, and connectivity data compelled researchers to propose topographical divisions of the HIPP (reviewed in (Moser & Moser 1998; Fanselow & Dong 2010)). As this division lacks consensus and shows variability depending on the studies considered, the present work applies the division proposed in (Dong et al. 2009). Accordingly, the HIPP is divided in three regions,

namely dorsal HIPP, dorsal-intermediate HIPP, and ventral HIPP (for coordinates and landmarks used in this division, see Figure 1).

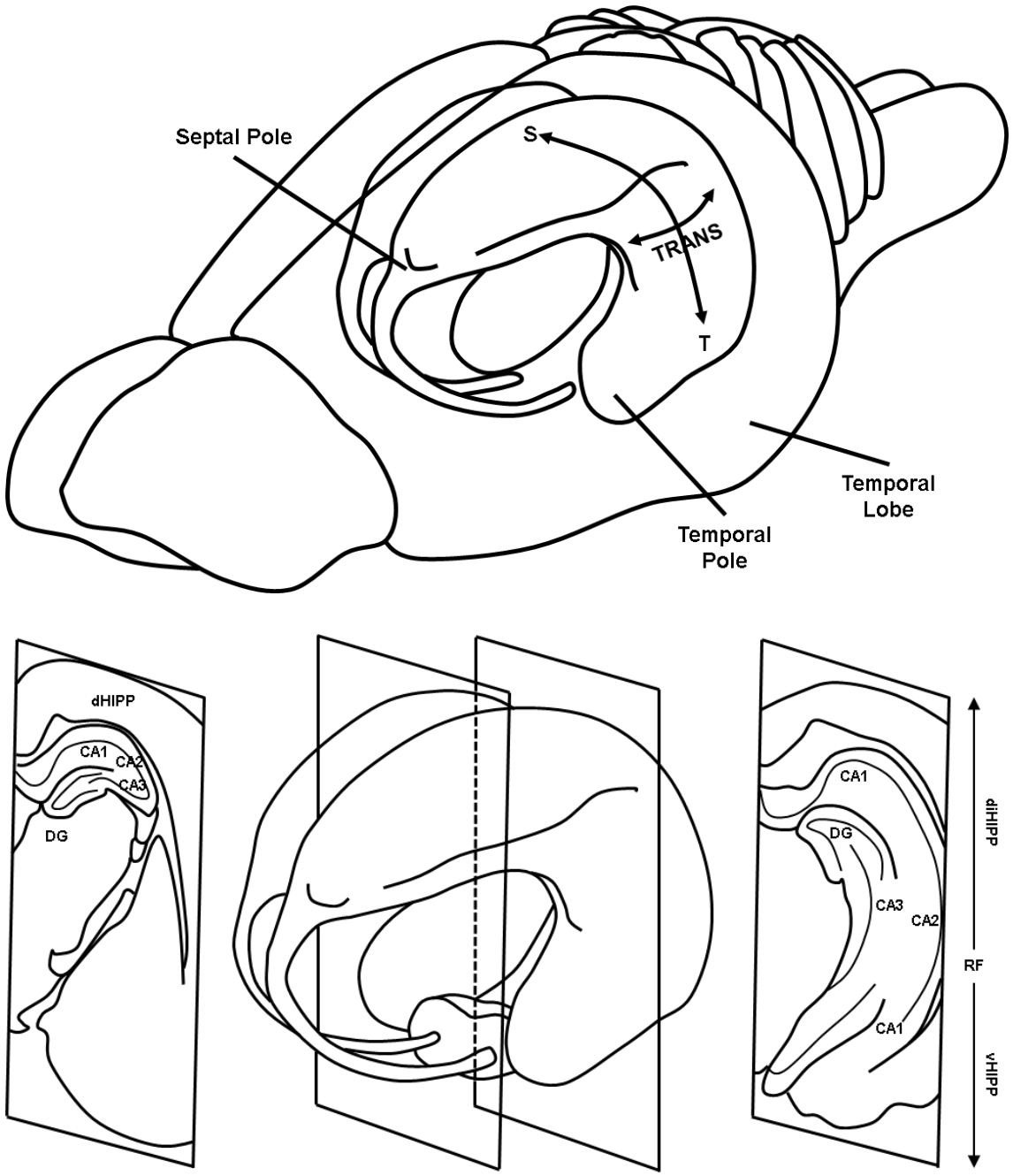

Figure 1 - The anatomy of the rat hippocampus. The HIPP has a long axis, the septotemporal axis, from the septal nuclei (S) to the temporal cortex (T), and a short or transverse axis (TRANS) perpendicular to the septotemporal axis (Amaral & Witter 1989). The HIPP is divided in dorsal HIPP (dHIPP; from -3.0 mm AP to -4.0 mm AP), dorso-intermediate HIPP (diHIPP; from -4.0 mm AP to -6.0 mm AP, above the rhinal fissure, RF), and ventral HIPP (vHIPP; from -4.0 mm AP to -6.0 mm AP, below the rhinal fissure, RF) (Dong et al. 2009).

A distinctive feature of the HIPP is its circuitry (Figure 2) (for review, see (Amaral & Witter 1989; Andersen 2007)). According to the classic hippocampal circuit described by Ramón y Cajal (Ramón y Cajal 1909) and Lorente de Nò (de Nò 1934), the entorhinal cortex (EC) is considered the starting point of the circuit. Neurons located in layer 2 of the EC give rise to a pathway, named perforant path, which terminates in the DG and in CA3, while neurons located in layer 3 of the EC project directly to CA1 and to the subiculum. The second step is the DG, which gives rise to the mossy fibers that project onto CA3, and to associational connections that target other levels of the DG. CA3 cells, in turn, project heavily onto other levels of CA3 and onto CA1. The projection targeting CA1 is called the Schaffer collateral projection. To close the classic circuit, CA1 cells project to the subiculum and to the deep layers of the EC, which project to many of the same cortical areas that initially projected to the EC. In summary, the classic hippocampal circuit includes the trisynaptic circuit EC > DG > CA3 > CA1, which runs in parallel with a direct input from the EC to CA1. CA1 and its major target, the subiculum, are therefore the major output regions of the HIPP.

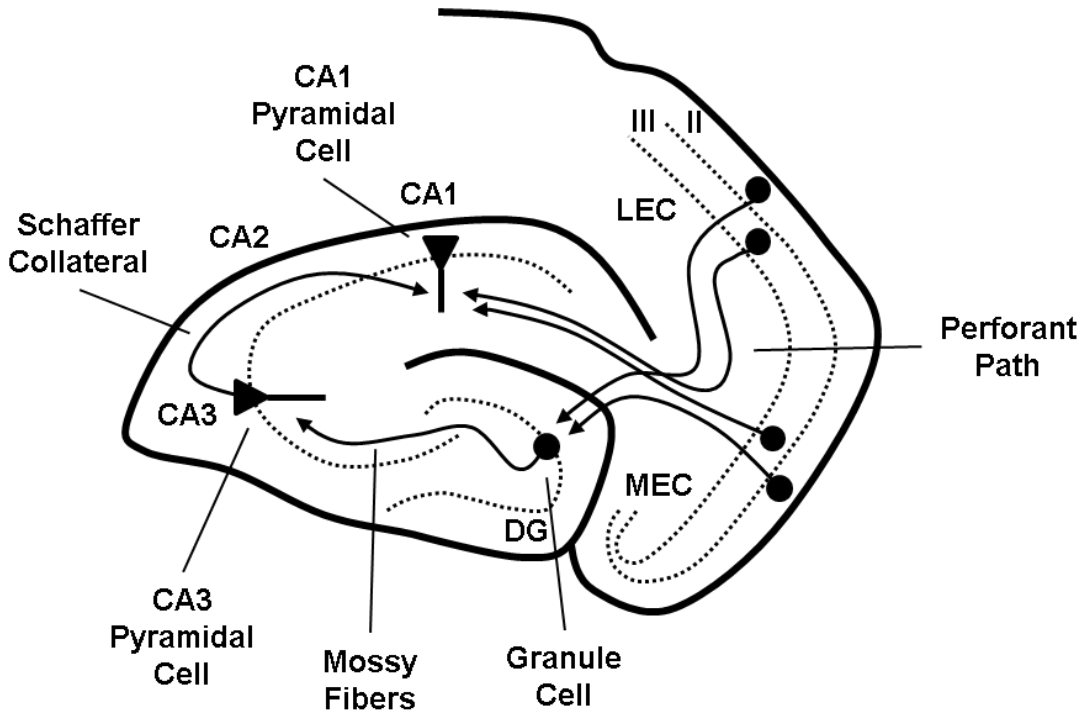

Figure 2 - The entorhinal-hippocampal circuit. The entorhinal-hippocampal circuit includes the trisynaptic loop and a direct entorhinal-hippocampal projection (Amaral & Witter 1989). LEC, lateral entorhinal cortex; MEC, medial entorhinal cortex.

Besides the distinctive anatomy and internal connectivity, the HIPP also shows an unusual laminar composition, with a single layer of densely packed pyramidal cells in CA1, CA2, and CA3, contrasting with the laminar composition of the isocortex, composed of 6 layers (for review on HIPP lamination, see (Andersen 2007)) (Figure 3). Despite lacking the typical cortical layers, CA1, CA2, and CA3 have well defined strata, called *stratum oriens* (SO), *stratum pyramidale* (SP), *stratum radiatum* (SR), *stratum lacunosum* (SL), and *stratum moleculare* (SM). SO is composed of cell bodies of inhibitory O-LM cells and horizontal trilaminar cells, basal dendrites from pyramidal neurons, and septal fibers and commissural fibers from the contralateral HIPP. SP contains the cell bodies of the pyramidal neurons, the principal hippocampal excitatory neurons, and cell bodies of interneurons, including basket cells, bistratified cells, axo-axonic cells, and radial trilaminar cells. SR is composed of proximal, apical dendrites of pyramidal neurons, septal fibers, commissural fibers, and the Schaffer collateral fibers, which correspond to the major monosynaptic projection from CA3 to CA1. Interneurons, specifically basket cells, bistratified cells, and radial trilaminar cells, are also present. SL, often grouped with SM due to its small thickness, is composed of Schaffer collateral fibers and perforant path fibers, which correspond to the major monosynaptic projection from the superficial layers of the EC to the HIPP. SM contains the distal, apical dendrites of pyramidal neurons, and perforant path fibers.

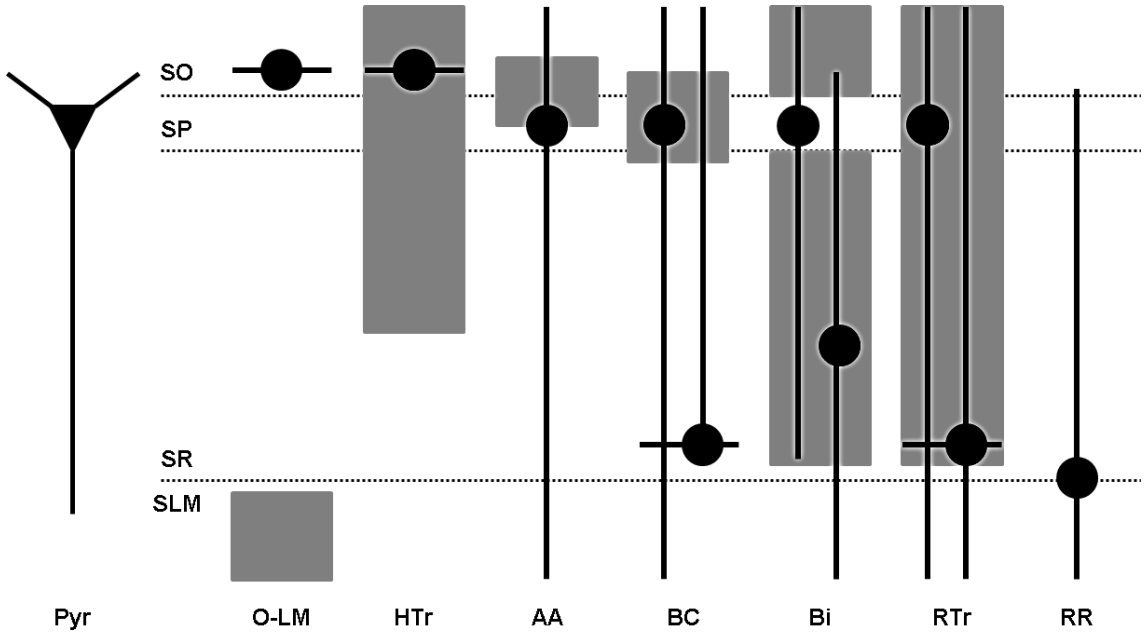

Figure 3 – Laminar distribution of the major hippocampal populations. The HIPP contains three types of pyramidal (Pyr) cells, whose cell body is located in SO (not illustrated), SP, and SR (not illustrated), and they are accompanied by at least 21 classes of interneurons in CA1 (only seven major classes are illustrated). The cell bodies and dendrites of each interneuron are depicted in black, whereas their synaptic terminations occupy the gray regions (Freund & Buzsáki 1996; Klausberger & Somogyi 2008). O-LM, *oriens lacunosum moleculare*; HTr, horizontal trilaminar; AA, axo-axonic; BC, basket cells; Bi, bistratified cell; RTr, radial trilaminar; RR, *radiatum*-retrohippocampal.

1.2. FROM THE HIPP TO THE PAPEZ CIRCUIT

The classic hippocampal circuit finishes at the level of CA1 and the subiculum, which project back to the EC. It was, however, a matter of time until the HIPP was integrated in a more extended brain loop. James Papez (Papez 1937) found that the subiculum also gives rise to a dense pathway, called the fornix, which terminates in the mammillary bodies of the hypothalamus. The mammillary bodies, in turn, give rise to the mammillothalamic tract, targeting the anterior thalamic nucleus, which project to the cingulate gyrus through the internal capsula. The cingulate gyrus projects back to the deep layers of the EC, via cingulum bundle. While the Papez circuit (Figure 4) has been extensively revised and updated (for review, see (Bubb et al. 2017)), it was crucial as it suggested an anatomical relation between the HIPP and the cingulate gyrus in humans.

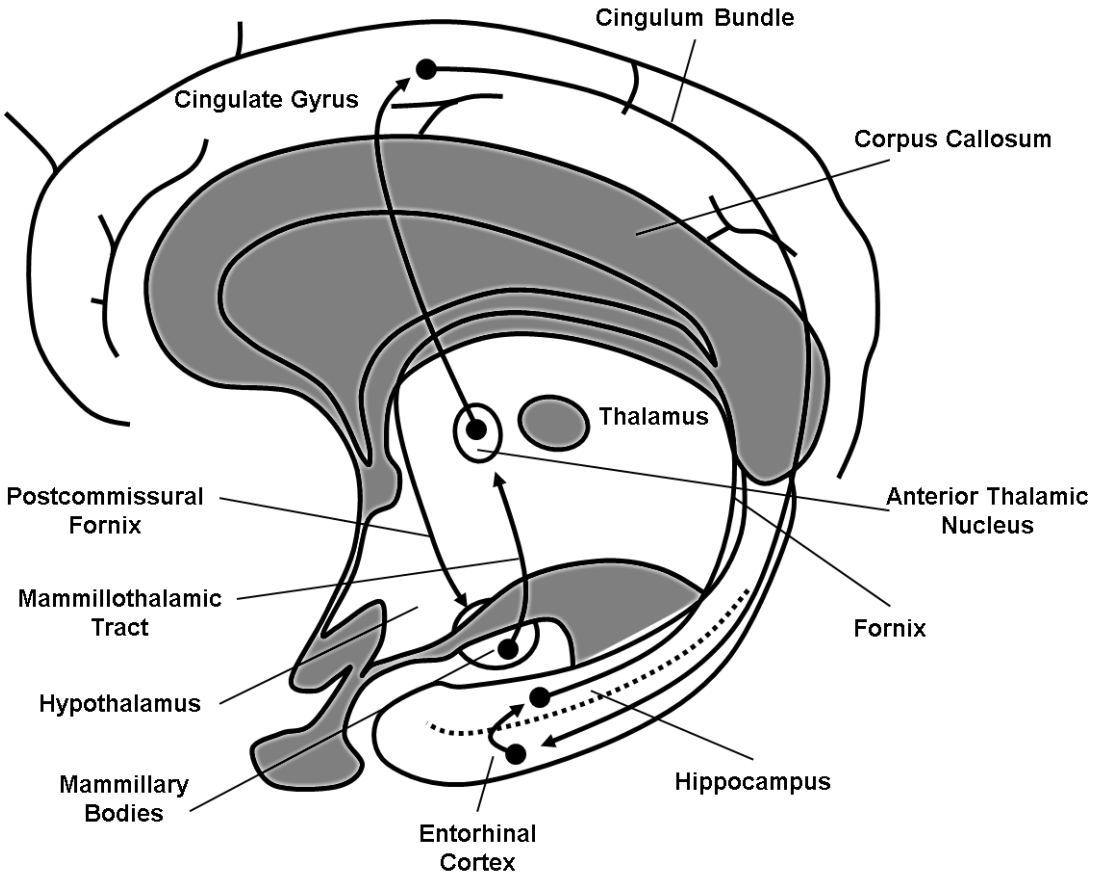

Figure 4 – The anatomy of the Papez circuit.

1.3. THE ANATOMY OF THE MEDIAL MESOCORTEX

While Papez has shown an anatomical relation between the HIPP and the cingulate gyrus in humans, the translation of such finding to the rat model needed attention. The rat has a brain region with considerable homology to the human cingulate gyrus, but there are two major differences (Vogt & Paxinos 2014). First, the rat lacks a true cingulate gyrus, due to the absence of the delimiting sulcus present in primates. Therefore, the rat homolog of the cingulate gyrus is a superficial CG, lying in the medial surface of the rat brain, right above the corpus callosum. Second, the rat lacks a homolog of the posterior cingulate cortex found in primates. Crucially, the posterior portion of the rat cingulate cortex is entirely composed of RSC. To account for these differences and for the changes in the nomenclature that happened in the last decades, the present work applies the most updated nomenclature proposed by Brent Vogt (Vogt & Paxinos 2014). We also

introduced the designation *medial mesocortex* to refer *the whole cingulate cortex of the rat*, since it is part CG and part RSC when compared with the primate homologs. This designation is accurate, as both CG and RSC of the rat are in the *medial* surface of the rat brain, right above the corpus callosum, and are classified as *mesocortex*. Still, some authors consider questionable whether the rat has a true CG (see (Heilbronner & Hayden 2016)), so the demonstration of similarity between areas in different species (rat and primates, in this case) and the use of a common nomenclature throughout this work never implies that areas with the same designation are exactly equivalent between species. It only implies that they share enough similarity to hypothesize common physiological mechanisms.

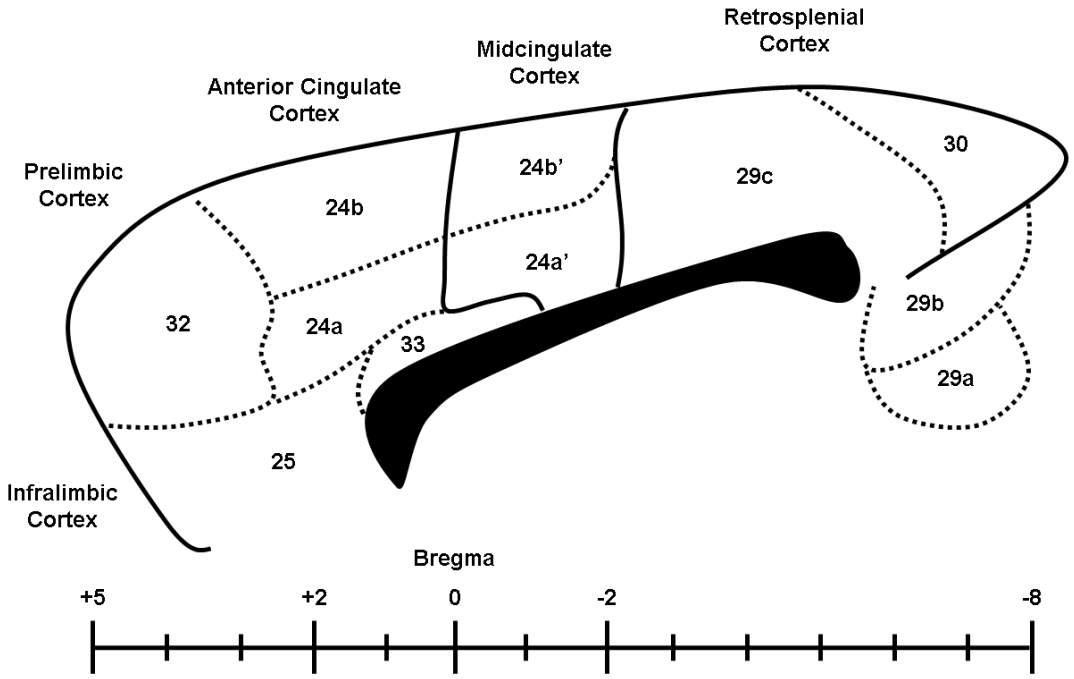

Figure 5 – The anatomy of the MMC. This scheme depicts the organization of the MMC proposed in (Vogt & Paxinos 2014), and used throughout the present dissertation. The MMC starts at +5 mm and extends until -8 mm. The major transitions occur at 0 mm from bregma (ACC to MCC) and at -2 mm from bregma (MCC to RSC). While Brent Vogt considered Brodmann areas 32 and 25 as part of ACC, they are commonly referred to as prelimbic cortex (area 32) and infralimbic cortex (area 25). Broadmann area 33 corresponds to a small and relatively undifferentiated area above the *indusium griseum*.

As depicted in Figure 5, the rostral portion of the MMC extends around the genu of the corpus callosum, whereas the caudal portion extends around the splenium of the corpus callosum. Using Vogt's nomenclature, the MMC is divided in three regions, namely the

anterior cingulate (ACC), which comprises Brodmann areas 25, 32, and 24 (24a and 24b), the midcingulate (MCC), which comprises Brodmann area 24' (24a' and 24b'), and the RSC, which corresponds to Brodmann areas 29 (29a, 29b, and 29c) and 30. According to Vogt, the transition from the ACC to MCC takes place at the bregma, whereas the transition from the MCC to the RSC occurs at -2.0 mm from bregma. The latter transition lacks consensus as Paxinos and Watson place it at -1.8 mm from bregma (Paxinos & Watson 2006). The division of the MMC is supported by structural, connectivity and functional data (for review, see Chapter 22 in (Paxinos 2004)). Together, these references highlight 4 crucial findings. First, the ACC and MCC are agranular regions, as they lack layer 4, whereas the RSC is granular (area 29) and dysgranular (area 30). Second, the MCC transiently expresses oxytocin receptors and neurotrophin-3, and has a particular opioid architecture different from the ACC. Third, each area (25, 32, 24, 24', 29 and 30) and subarea (24a/24b, 24a/24b', and 29/29b/29c) have distinct cytoarchitectures, differing in the number and thickness of the cortical layers, and in the morphology and distribution of the neurons populating those layers. Fourth, each area and subarea show differential connectivity patterns with intra-MMC and extra-MMC targets. Connectivity studies have shown, for instance, that ACC receives prominent input from the amygdala (unlike the MCC), whereas the MCC projects strongly to the pontine nuclei. Other prominent connectivity gradients were found between the divisions of the MMC and the visual cortices, the thalamic nuclei, the EC, and, crucially, the HIPP.

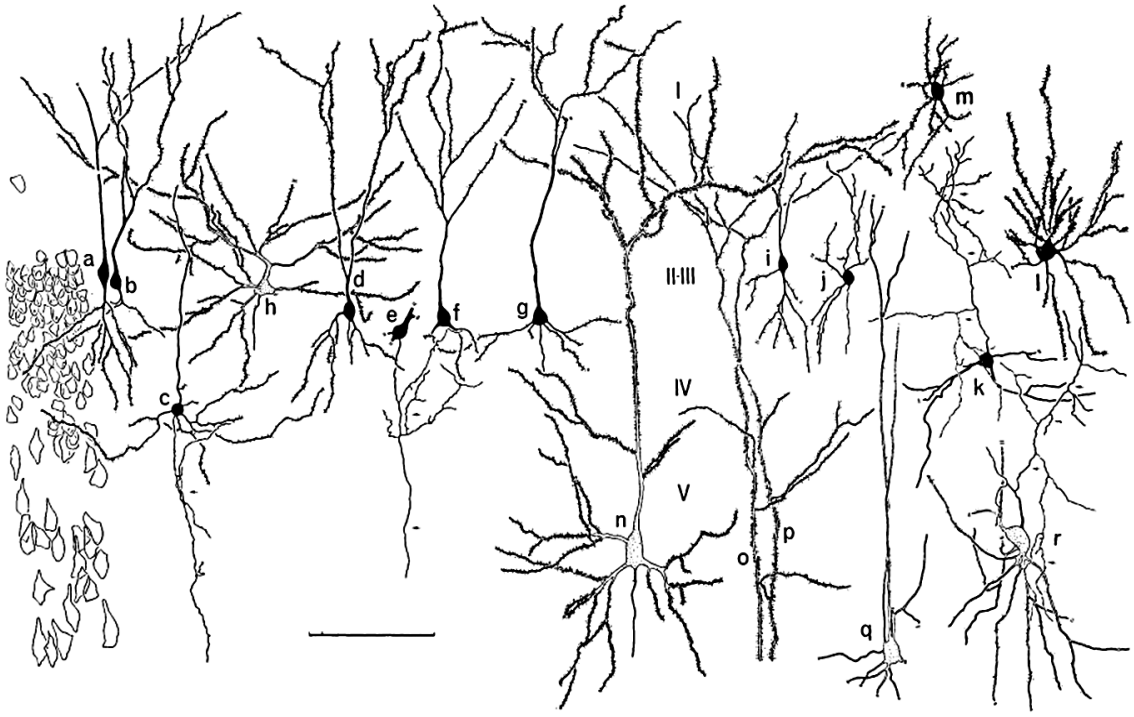

Figure 6 - Laminar distribution of the major neuronal populations in subarea 29c. Roman numerals indicate cortical layers. a and b, fusiform pyramids; c, d, e, f and g, small pyramids; h, medium pyramids; m, small multipolar cell; k, medium multipolar cell; l, large stellate cell; i, small bipolar cell; j, small multipolar cell; n, large pyramid; o and p, apical dendrites of small-medium pyramids of layer 6; q and r, large multipolar cells. Scale bar: 100 µm. Adapted from (Vogt & Peters 1981).

Regarding the morphology and distribution of the neurons populating the MMC, Figure 6 depicts the most prominent neuronal populations of area 29c (Vogt & Peters 1981). These include pyramidal cells with the typical orienting apical dendrite and descending axon entering the white matter, and stellate (non-pyramidal) cells which lack the orienting dendrite and have axons that terminate intracortically without entering the white matter. As depicted in Figure 6, pyramidal cells occur in layers 2-6, and have their apical tufts in layer 1. The major populations of such pyramidal cells are the large pyramids of layer 5, the fusiform pyramids of layer 2-3, and the small and medium pyramids of layers 2-3 and 4. Regarding the stellate cells, they appear as multipolar cells, when dendrites radiate equally around the soma, bipolar cells, when a primary dendrite projects from the upper and lower poles of the soma, and bitufted cells, when tufts of three or more dendrites project from the top and bottom of the soma. As shown in Figure 6, small multipolar cells are more superficial, whereas the medium and large multipolar cells are located primarily in layers 3 and 5. The bitufted cells are most frequent in layers 2 and 3, although they are

also present in layers 5 and 6. The bipolar cells are primarily found in layers 2 and 5. Although Figure 6 is a drawing from subarea 29c, the neuronal populations described are essentially conserved in the remaining subareas of the MMC (Vogt & Peters 1981). Figure 6 will be, therefore, considered the standard circuit of the MMC for the purposes of the present introduction.

1.4. MONOSYNAPTIC HIPP-MMC PROJECTIONS

There is evidence supporting the existence of monosynaptic connections between the HIPP and the divisions of the MMC. These connections display a topographical gradient depending on the specific area of the MMC targeted by the HIPP.

Regarding the ACC, Jay and Witter showed that injection of *Phaseolus vulgaris*-leucoagglutinin (PHA-L) in the proximal part of the subiculum and in CA1, except in the most dorsal part of CA1, resulted in weak labeling of axons in the deep layers of ACC, in the rat (Jay & Witter 1991). Lee A Cenquizca and Swanson further detailed the previous observation (Lee A Cenquizca & Swanson 2007). Injection of PHA-L in the dorsal third of CA1 resulted in sparse labeling of the dorsal tenia tecta, whereas injection in the intermediate levels of CA1 resulted in weak labeling of axons in the deep layers of ACC, in the rat. Crucially, injection in ventral CA1 led to moderate labeling of terminal buttons in deep layers of subarea 24a and 24b, and to light labeling of terminal buttons in superficial layers of subarea 24a. These influential studies used anterograde tracers, but were complemented by two studies with retrograde tracers. Hoover and Vertes reported retrograde labeling of hippocampal cells upon injection of Cholera Toxin β-subunit (CTB) in the ACC of the rat (Hoover & Vertes 2007). More recently, Fillinger and colleagues showed in the mouse that retrograde labeling of hippocampal cells was produced when the injection of CTB was restricted to subarea 24a or rostral subarea 24b, but not when the injection was in caudal subarea 24b (Fillinger et al. 2017).

In the RSC, Finch, Derian and Babb showed that injection of horseradish peroxidase conjugated to wheat germ agglutinin (retrograde tracer) did not result in retrograde labeling of cells in the CA fields, but only in the subiculum (Finch et al. 1984). Contrarily to the previous observation, van Groen and Wyss found retrograde labeling of cells in the

subiculum and in CA1 upon injection of fast blue or fluorogold in subarea 29a (van Groen & Wyss 1990). The cells labeled in CA1 corresponded to «…a small number of pyramidal and nonpyramidal neurons…». Similar experiments were carried out in area 30 and in subarea 29b. Injection of the fast blue or fluorogold in area 30 did not produce labeling of hippocampal neurons (van Groen & Wyss 1992), whereas injection in subarea 29b led to retrograde labeling of «…very small numbers of nonpyramidal neurons…» in dorsal CA1 (van Groen & Wyss 2003). Complementing the previous studies, Lee A Cenquizca and Swanson reported moderate number of labeled axons in areas 29 and 30, specifically in layers 1 to 4, upon injection of PHA-L in the dorsal third of CA1 (Lee A Cenquizca & Swanson 2007). Injection in intermediate CA1 and ventral CA1 led to labeling of a few axons in layer 1 of area 29 and in layer 6 of area 30, respectively. In a subsequent study, Miyashita and Rockland showed retrograde labeling of non-pyramidal neurons in CA1 after injection of CTB conjugated with Alexa 488 in area 29 (Miyashita & Rockland 2007). These neurons were particularly abundant in the border of the SR and *stratum lacunosum-moleculare* and stained positive for GAD67 and GABA, establishing their identity as hippocampal long-range projecting GABAergic neurons targeting area 29.

Concerning the MCC, Finch, Derian and Babb showed that injection of horseradish peroxidase conjugated to wheat germ agglutinin does not result in retrograde labeling of cells in the HIPP (Finch et al. 1984). Contrarily to the previous, Lee A Cenquizca and Swanson reported moderate number of labeled axons in the «…caudal portion of cingulate cortex…», specifically in layers 1 to 4, upon injection of PHA-L in the dorsal third of CA1 (Lee A Cenquizca & Swanson 2007). More recently, Fillinger and colleagues found in the mouse that retrograde labeling of hippocampal cells was produced when the injection of CTB was restricted to subarea 24a', but not when the injection was in subarea 24b' (Fillinger et al. 2017).

2. SECTION 2 - THE HIPP-MMC INTERACTION AT THE MICROCIRCUIT LEVEL

While the work reviewed in this section suggests that the HIPP-MMC projection forms functional synapses onto the MMC, these studies displayed two major caveats. First, these studies used electrical stimulation of the HIPP or hippocampal projections to evoke activity in the MMC. This stimulation protocol leads to stimulation of many pathways beyond the hippocampal projections targeting the MMC, which consists in an anatomical confound, and stimulation of inhibitory and excitatory neurons alike, which constitutes a serious functional confound. Second, the extracellular recordings in the MMC were carried out one position at a time. This procedure does not provide access to the spatiotemporal dynamic of the evoked responses at the microcircuit level, which requires simultaneous recordings at different positions in the MMC.

An ideal experimental system to probe whether the HIPP-MMC projection forms functional synapses onto the MMC would allow (1) *in vitro* experimentation, which could be achieved by using acute cortical slices containing the MMC; (2) specific, fast and reversible stimulation of the hippocampal projections targeting the MMC, which could be achieved by optogenetic stimulation of such projections; (3) simultaneous extracellular recordings at different positions, which implies the use of a multi-electrode array (MEA); (4) matching the extracellular recordings with the anatomy of the acute slice; and (5) specific stimulation of inhibitory and excitatory neurons. To build such a system, in the present work we developed a protocol for *in vitro* high-throughput extracellular recordings in acute MMC slices based on the MEA2100-System®, coupled with optogenetic stimulation of the hippocampal axon terminals preserved in the acute slices using ChR2, and sequential pharmacological manipulation.

2.1. THE HIPP-RSC INTERACTION AT THE MICROCIRCUIT LEVEL

Figure 7 depicts the standard microcircuit of subarea 29c and the known laminar distribution of the hippocampal axons. Our current understanding of the HIPP-RSC interaction at the microcircuit level derives from *in vitro* studies in rat acute cortical slices

(Hedberg et al. 1993) and *in vivo* studies in the anesthetized rat (Hedberg & Stanton 1995).

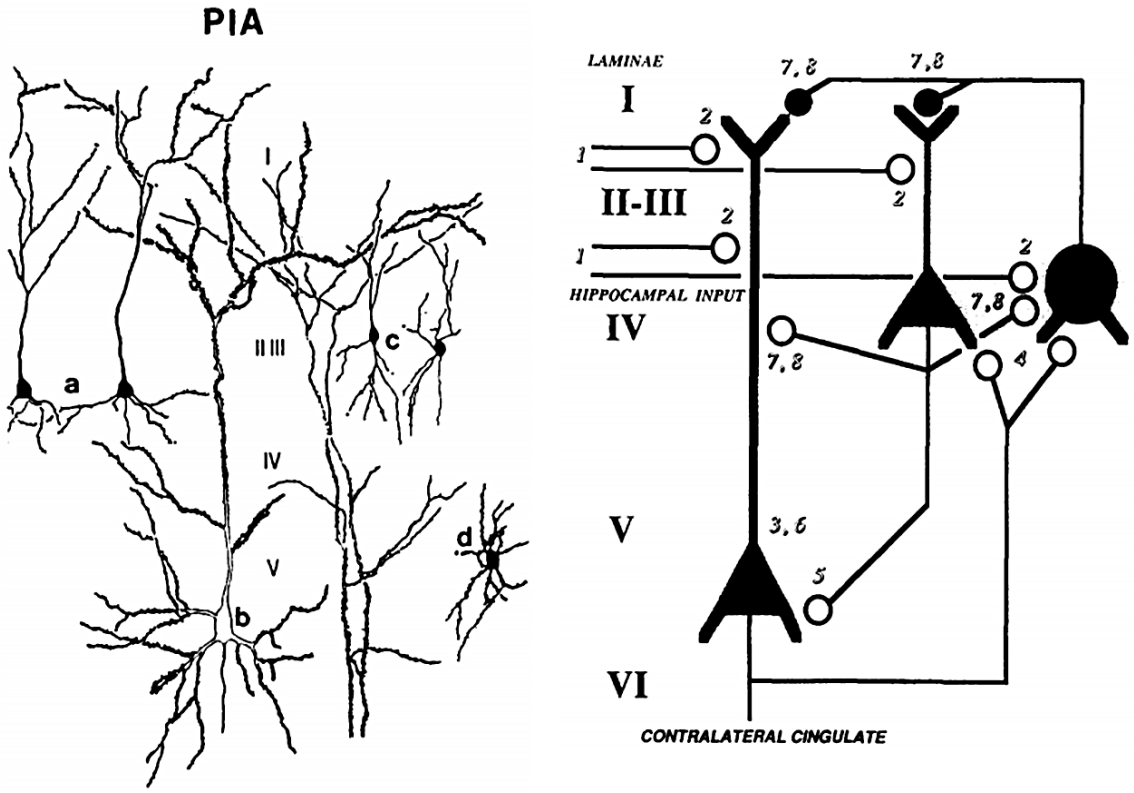

Figure 7 – Standard microcircuit of subarea 29c. Left, Neurons shown include (a) a small pyramid; (b) a large pyramid; (c) a fusiform cell. Adapted from (Vogt & Peters 1981). Right, Description of the extracellular activity in subarea 29c upon electrical stimulation of the SCT, as hypothesized in (Hedberg et al. 1993). 1, fiber volley; 2, monosynaptic EPSP; 3, depolarization of deep lamina pyramids; 4, putative disynaptic pathways; 5 to 8, di- and polysynaptically evoked depolarizations. Roman numerals indicate cortical layers. The triangle in layer V represents medium and large pyramids, whereas the triangle in layer III and IV represents small pyramids and fusiform cells. The solid circle represents polimorphic, local inhibitory interneurons. Small open circles are hypothesized excitatory synapses and small filled circles are hypothesized inhibitory synapses. Adapted from (Hedberg et al. 1993).

Hedberg, Simpson and Stanton developed a protocol to produce rat acute cortical slices containing subarea 29c (RSC), the subiculum, and a functional fraction of the subiculo-cingulate tract (SCT) (Hedberg et al. 1993). Using this preparation, they showed that electrical stimulation of the SCT elicited a sink in layer 1 (latency: 1.5 ms), followed by a sink in layer 2/3 (latency: > 2.0 ms), and succeeded by a sink in layers 4 and 5 (latency: < 4.0 ms) (Hedberg et al. 1993). After these early sinks, three latter sinks appeared in the superficial layers, the first in layer 1 (latency: 4.0 ms), the second in layers 2/3 and 4 (latency between 4.0 and 8.0 ms), and the third in layer 1 (latency: 8.0 ms). From Figure 6

and knowing that the SCT terminates in layer 2/3, with sparse innervation of layer 1 and 4, (Hedberg et al. 1993) hypothesized a model for the population events recorded in subarea 29c. In their model, the first sink (latency: 1.5 ms) corresponded to the depolarization of the SCT, whereas the second sink (latency: > 2.0 ms) corresponded to the excitatory post-synaptic potentials (EPSP) on the apical dendrites of pyramidal neurons from layer 5. The depolarization of the apical dendrites would evoke action potentials in the pyramidal neurons from layer 5, explaining the sink observed in layers 4 and 5 (latency: < 4.0 ms). Together, these events suggested that stimulation of the SCT recruited pyramidal neurons from layer 5 monosynaptically at their apical dendrites. The discharge of pyramidal neurons in layer 5 would result in polysynaptic activation of pyramidal cells and interneurons located in layers 2/3 and 4, via the ascending axon collaterals of the pyramidal cells from layer 5. This would explain the late, superficial sinks described (latencies ranging from 4.0 to 8.0 ms). This model was further supported by additional intracellular and extracellular multiple-unit data, and it remains the only model available in literature to explain the activity of the MMC at the microcircuit level, upon hippocampal stimulation in the rat. Hedberg and Stanton further probed the synaptic plasticity of the HIPP-RSC projection (subarea 29c) (Hedberg & Stanton 1995). High-frequency stimulation of the SCT produced long-term potentiation, whereas 1-5 Hz stimulation of the SCT induced long-term depression, both restricted to deep layers of subarea 29c. In contrast, superficial layers showed paired-pulse facilitation, particularly at a 190 ms inter-stimulus interval (ISI), and short-term post-tetanic potentiation.

To test their model using an *in vivo* system, Hedberg and Stanton recapitulated the *in vitro* work in the anesthetized rat (Hedberg & Stanton 1995). In the anesthetized rat, Hedberg and Stanton evoked a trimodal response in the local field potential (LFP) in the deep layers of subarea 29c (RSC), upon electrical stimulation of the subiculum with single pulses (Hedberg & Stanton 1995). These evoked responses *in vivo* matched the evoked potentials produced by the stimulation of the SCT in the *in vitro* preparations, and consisted of two negativities (N1 @ 3-4 ms, N2 @ 5-6 ms) and one positivity (P1 @ 8-10 ms). Regarding plasticity changes and in agreement with their *in vitro* work, the authors showed paired-pulse facilitation upon stimulation of the SCT with an ISI falling between 120 and 300 ms (3-8 Hz, theta frequency band). Besides tuning sensitivity, the responses

in deep layers of subarea 29c showed evidence of long-term potentiation when high-frequency stimulation (60 Hz/ 3-5 s/ 2x) was delivered to the SCT.

2.2. THE HIPP-ACC INTERACTION AT THE MICROCIRCUIT LEVEL

A detailed description of the neuronal populations in area 24 is not available in literature and the distribution of the hippocampal axons is debatable. Our current understanding of the HIPP-ACC interaction at the microcircuit level derives from *in vivo* studies in the anesthetized rat (Gigg et al. 1994; Ishikawa & Nakamura 2003; Nakamura et al. 2010; Brockmann et al. 2011).

Gigg, Tan and Finch established the neurotransmitters used in the HIPP-mPFC projection (including subarea 24b of ACC) using multi-barrel iontophoresis (Gigg et al. 1994). Electrical stimulation of the HIPP (DG, CA1, and subiculum) produced excitation followed by prolonged inhibition in 6% of the prefrontal cells, prolonged inhibition alone in 26% of the prefrontal cells, and no clear response in 68% of the prefrontal cells. While these numbers derive from recordings in the whole mPFC, the qualitative aspects of the responses were conserved across subareas. The recordings in subarea 24b were carried out in layer 2 and in layer 5. The excitatory responses were inhibited by CNQX iontophoresis, with and without a concomitant decrease in spontaneous firing, and consisted of one spike with mean latency of 16 ms. No attenuation of the excitatory responses was reported upon D-CPP iontophoresis. These results suggest that the HIPP-ACC projection is, at least in part, glutamatergic, and provides excitatory, monosynaptic drive to cells in subarea 24b. Regarding the inhibitory responses, they were composed of a CGP-35348-sensitive, long-latency component (>100 ms), and of a bicuculline methiodide-sensitive, short latency component. The long-latency component explains the prolonged inhibition observed (alone or following excitatory responses). The short-latency component explains the observation of excitatory responses upon bicuculline methiodide iontophoresis in cells with no pre-drug excitation to hippocampal stimulation. These results suggest that the HIPP-ACC projection also drives local GABAergic neurons in subarea 24b. Complementing the previous study, Ishikawa and Nakamura recorded 22 single units in subarea 24b (ACC) in the anesthetized rat (Ishikawa & Nakamura 2003).

Electrical stimulation of ventral CA1/subiculum with single pulses induced excitation in 3 (latency: 48.0 ± 4.9 ms) and inhibition in 7 (latency: 45.0 ± 8.9 ms) of the 22 neurons recorded. The excitatory and inhibitory latencies suggested a polysynaptic effect onto the 10 neurons modulated by the hippocampal stimulation. More recently, Brockmann and colleagues reported evoked responses in subarea 24b (ACC) starting at 12.2 ± 0.6 ms and lasting for 22.34 ± 1.71 ms, after single pulse electrical stimulation of intermediate CA1, in anesthetized neonatal rats (Brockmann et al. 2011).

Nakamura, Katayama and Kawakami further explored the synaptic plasticity of the HIPP-ACC projection (subarea 24b) in the anesthetized rat, by evaluating nociceptive responses after high-frequency stimulation in dorsal CA1/subiculum (Nakamura et al. 2010). High-frequency stimulation in dorsal CA1/subiculum led to long-term enhancement of nociceptive responses in layer 2/3 neurons of subarea 24b (with no effect on c-fos expression levels).

2.3. SUMMARY OF THE CLASSICAL LITERATURE

A systematic overview of the studies characterizing the rat HIPP-MMC projection at the microcircuit level is provided in Table 1. The studies were classified according to the system used (*in vitro* vs. *in vivo*), the electrophysiology technique applied (intracellular recordings, extracellular recordings, or both), and whether synaptic plasticity was evaluated or not. Crucially, most of the studies were carried out in subareas 32 and 25, commonly referred as the rat prelimbic and infralimbic cortex, respectively. While these subareas are part of ACC according to Vogt's nomenclature, the present dissertation focuses specifically on subareas 24, 24', 29 and 30. Only the studies targeting such subareas were reviewed in detail in the previous sections.

Table 1 – Systematic overview of the studies characterizing the rat HIPP-MMC projection at the microcircuit level. For each study, the table indicates whether intracellular (I) or extracellular (E) recordings were performed, whether short-term (S) and long-term (L) plasticity protocols were used, and which MMC areas were studied.

	System	Ephys (I/E)	Plasticity (S/L)	MMC Area
(Hedberg et al. 1993)	*In vitro*	I + E	-	29c
(Laroche et al. 1990)	*In vivo*	E	S + L	32
(Gigg et al. 1994)	*In vivo*	E	-	24b, 32, 25
(Hedberg & Stanton 1995)	*In vivo*	I + E	S + L	29c
(Jay et al. 1995)	*In vivo*	E	L	32
(Jay et al. 1996)	*In vivo*	E	L	32
(Takita et al. 1999)	*In vivo*	E	L	32
(Dégenètais et al. 2003)	*In vivo*	I	L	32
(Izaki et al. 2003)	*In vivo*	E	S + L	32
(Ishikawa & Nakamura 2003)	*In vivo*	E	-	24b, 32, 25
(Tierney et al. 2004)	*In vivo*	E	-	32
(Nakamura et al. 2010)	*In vivo*	E	L	24b, 32
(Brockmann et al. 2011)	*In vivo*	E	-	24b, 32

3. SECTION 3 - THE HIPP-MMC INTERACTION IN MEMORY, SPATIAL NAVIGATION AND GOAL-DIRECTED BEHAVIOR

Previous studies reviewed in this section addressed independently the role of HIPP and the divisions of the MMC in memory, spatial navigation and goal-directed behavior. While SWM is a fundamental component of memory and spatial navigation, the HIPP-MMC interaction in SWM was only studied in a spatial sequence task, and the work was restricted to the patterns of HIPP-CG coactivity. As a follow up of that work, the present dissertation aims at 1) describing the patterns of HIPP-MMC coactivity in the encoding, maintenance, and retrieval phases of SWM; 2) comparing the patterns of HIPP-ACC, HIPP-MCC, and HIPP-RSC coactivity in the encoding, maintenance, and retrieval phases of SWM; 3) probing and comparing the necessity of the HIPP-ACC, HIPP-MCC, and HIPP-RSC

interactions in SWM by specifically inhibiting these interactions in the encoding, maintenance, and retrieval phases of SWM.

3.1. GOAL-DIRECTED BEHAVIOR

The ability to make choices based on previous experiences allows animals to survive in dynamic environments. During natural behaviors, animals can shift between decision-making strategies, performing habitual choices and goal-directed choices. Habitual choices are a consequence of retrospective and slow accumulation of rewards via iterative updating of expectations, whereas goal-directed choices prospectively consider future outcomes of an action (Friedel et al. 2014; Lee et al. 2014; Voon et al. 2017). Goal-directed choices are, therefore, sensitive to devaluation, leading to quick behavioral adaptation, while habitual choices require new reward experience to change the behavior (Friedel et al. 2014; Lee et al. 2014; Voon et al. 2017). Rather than mutually exclusive, these choice strategies are interleaved in natural behaviors (Lee et al. 2014) and, depending on the animal's degree of performance in a specific task, habits can replace goal-directed choices (reviewed in (Redish 2016)). Crucially, the two strategies engage different sets of brain regions (reviewed in (Dolan & Dayan 2013)). The strongest evidence that goal-directed and habitual choices are supported by different neural substrates, and that increased performance shifts decision-making strategies from goal-directed to habitual comes from (Horga et al. 2015), who have shown a shift in control from the limbic system to the corticostriatal system in learners compared to non-learners, while performing a reinforcement learning task.

As the present dissertation focus on goal-directed choice in animals, it is important to define it algorithmically. While performing a behavioral task, animals express three decision-making stages, depending on their performance. The first stage is characterized by deliberation, defined as the process by which an agent searches through possibilities based on hypothesized models of the environment and evaluates hypothesized outcomes as a means of making decisions (Redish 2013; Redish 2016). In this stage, animals know the structure of the environment (or not), and need to vicariously try different alternatives to determine what they want to do (Redish 2013; Redish 2016). In the second

stage, characterized by action planning, animals know the structure of the environment and what they want to do, narrowing the deliberative process to just one option (Redish 2013; Redish 2016). As the performance increases, animals eventually enter a third stage, characterized by behavioral automation and the execution of action chains (Redish 2013; Redish 2016). Experimental data support this three-stage model of decision-making, and each stage has specific behavioral and electrophysiological signatures (reviewed in (Redish 2016)). For instance, deliberation shows high VTE levels and hippocampal replay of multiple alternative trajectories, whereas planning shows decreased VTE levels and hippocampal replay of trajectories mainly leading to the goal (Tolman 1939; Tolman 1948; Muenzinger & Gentry 1931; Johnson & Redish 2007). Upon automation, VTE and hippocampal replay become uncommon (Tolman 1939; Muenzinger & Gentry 1931; Johnson & Redish 2007; Tolman 1948). Goal-directed choice is, therefore, recognized when deliberation and action planning occur, which have specific behavioral and neural signatures, and is sensitive to devaluation.

Conceptually, goal-directed choice requires 1) the formation and storage of an internal representation of the environment (known as cognitive map (Tolman 1948)), as a product of previous experiences; 2) the retrieval of the mnemonic information acquired to provide options for deliberation and planning; 3) the comparison and evaluation of the options available; and 4) the selection of a final action (Yu & Frank 2014; Redish 2016). All these processes engage a plethora of brain regions, particularly the HIPP (Ruediger et al. 2012; Horga et al. 2015) and the MMC (reviewed in (Devinsky et al. 1995)).

3.2. SPATIAL NAVIGATION AS A MODEL OF GOAL-DIRECTED CHOICE

Spatial navigation in the brown rat, *Rattus norvegicus*, has been used as a model of goal-directed choice. In these paradigms, rats are supposed to find a goal location, which can be accomplished using three major strategies (Chersi & Burgess 2015). The rat might follow a sensory cue that directly indicates the goal location (“piloting”). Alternatively, the rat might perform a well-learned sequence of actions, each based on the previous action or sensory cue (egocentric strategy), or it might use an internal representation of the environment (allocentric strategy). Operationally, egocentric navigation is sensitive to

changes in the starting point, as reaching the goal depends on a sequence of actions, while allocentric navigation is sensitive to changes in distal cues, as it implies the formation of cognitive map of the environment. Egocentric and allocentric strategies engage different brain systems. While cortico-basal ganglia circuits support stimulus-response associations and learning sequences of actions in egocentric navigation, the HIPP supports the formation of a cognitive map of the environment required for allocentric navigation. These navigational principles and their neuronal substrates are conserved in humans (Burgess et al. 2002; Doeller et al. 2008; Iaria et al. 2003).

The present dissertation uses spatial navigation based on allocentric strategies to model goal-directed choice. During allocentric navigation, rats 1) store a cognitive map of the environment, using the distal cues and previous foraging experiences; 2) retrieve potential trajectories; 3) compare and evaluate the potential trajectories available; and 4) perform a final navigational choice to achieve a desired goal. These processes are usually expressed as VTE, a specific behavior established as a correlate of deliberation and action planning. During VTE, rats pause in the decision points and turn their head back and forth, scanning the potential routes available. This behavior is more frequent in the learning phase of the tasks, but can persist depending on the difficulty of the task.

3.3. SPATIAL NAVIGATION AND MEMORY

Spatial navigation is intimately tied to memory, as it requires the encoding and storage of information from previous foraging experiences and the recall of such information. There are different types of memory, supported by different brain systems (for review, see (Squire 2004)). Memories can be short-lived (sensory memory, short-term memory, and working memory) or long-lived (long-term memory), in respect to duration, and long-term memories can be implicit (non-declarative) or explicit (declarative), in respect to the information content. Different navigation strategies rely in different types of memory and neural substrates. Procedural memory dominates in periods of egocentric navigation, whereas episodic memory and working memory dominate in periods of allocentric navigation. Crucially, procedural memories are supported by the cortico-basal ganglia circuits, whereas episodic memories are supported by the HIPP.

While the navigation strategies are conserved between humans and rodents, a direct translation of the memory types from human literature to rodents is debatable. As the present dissertation focus on allocentric, hippocampal-dependent navigation, rats are expected to rely on (spatial) working memory and episodic-like memory. Operationally, (spatial) working memory is defined as a short term memory for a stimulus (location) that is used within a testing session, but not typically between sessions (Dudchenko 2004). It consists, therefore, in a delay-dependent representation of a given stimulus, which persists after the cessation of the stimulus, and is used to guide behavior within a testing session (Dudchenko 2004). In spatial working memory tasks, working memory contrasts with reference memory, referred as the memory of task components that remain constant over time (e.g. task rules) (Dudchenko 2004). It is debatable whether rats possess long-term episodic and semantic memories (declarative), as defined for humans (Morellini 2013). Operationally, rodent episodic-like memory is defined as the ability to produce behavioral responses based on "what" occurred, "where", and "when" during a past experience.

3.4. THE FUNCTION OF THE HIPP

Two major lines of research established our functional understanding of the HIPP. One literature, mainly based in human studies, started with the observation that human patients with bilateral lesion in the HIPP, with and without involvement of additional regions of the medial temporal lobe, suffer from anterograde amnesia, being unable to transfer new episodic information from working memory into long-term memory (Scoville & Milner 1957; Penfield & Milner 1958; Squire 2009). The HIPP is, therefore, necessary for declarative memory. The other literature, mainly based in rodent studies, emphasizes the role of the HIPP in spatial navigation. While rodents navigate in the environment, hippocampal pyramidal neurons display increased firing rate when the animal is at a specific location. These cells were named "place cells", and their preferred location in the environment was named "place field" (O'Keefe & Dostrovsky 1971; O'Keefe 1976; O'Keefe 1979; O'Keefe & Conway 1978). By firing at particular places, place cells presumably contribute to an internal representation of the environment, a cognitive

(spatial) map (O'Keefe 1991; Tolman 1948; O'Keefe & Dostrovsky 1971). When the rat is moved to a new environment, place cells' activity shifts, and another internal representation (cognitive map) arises, consistent with the second environment (Jezek et al. 2011). Accordingly, hippocampal inactivation impairs allocentric navigation in rodents (Morris et al. 1982), and these findings were also reproduced in humans (Ekstrom et al. 2003; Parslow et al. 2005). The HIPP is, therefore, necessary for allocentric navigation.

While both theories of hippocampal function have been fruitful, efforts have been made to reconcile the two perspectives (for review, see (Eichenbaum & Cohen 2014)), by expanding the spatial navigation theory. Compelling data suggest, indeed, that the HIPP is not solely devoted to spatial processing, and that the hippocampal cognitive maps are not composed as a Euclidian coordinate space dedicated to allocentric navigation. While there are many objections to a strict spatial navigation theory to explain hippocampal function (see (Eichenbaum & Cohen 2014)), an essential finding was the observation that hippocampal cells can be modulated by spatial and non-spatial variables. The first report supporting non-spatial modulation of hippocampal neurons came from John O'Keefe, who reported that less than a third neurons recorded in his study actually encoded place (O'Keefe & Dostrovsky 1971). Since then, the HIPP was found to encode objects (Manns & Eichenbaum 2009), time (reviewed in (Eichenbaum 2014)), social variables (Tavares et al. 2015), among other non-spatial variables defining the current experience (Tanaka et al. 2018).

A parsimonious and influential reconciliation of the two literatures was advanced by Howard Eichenbaum (Eichenbaum & Cohen 2014). In his words, the HIPP could act as a «*relational processing system, … encoding events as relational mapping of objects and actions within spatial contexts, representing routes as episodes defined by sequences of places traversed, and relating spatial episodes to existing semantic maps of space…*». The hippocampal function in allocentric spatial navigation would be, therefore, a particular case, useful to study hippocampal function in the lab using rodent models. How would the HIPP work as a relational system? A mechanistic answer was proposed by Timothy Teyler (Teyler & DiScenna 1986; Teyler & Rudy 2007), who advanced the Memory Indexing Theory (Figure 8). In his words, «*…the hippocampus stores a map of locations of other brain regions.*» In this sense, experience drives specific cortical ensembles, which activate sets of hippocampal cells, strengthening their synaptic connections. The

hippocampal ensemble persists beyond the experience, indexing the cortical ensembles previously active. Future reinstatement of that hippocampal ensemble would produce the reinstatement of the cortical ensembles and, thus, the reinstatement of the past experience.

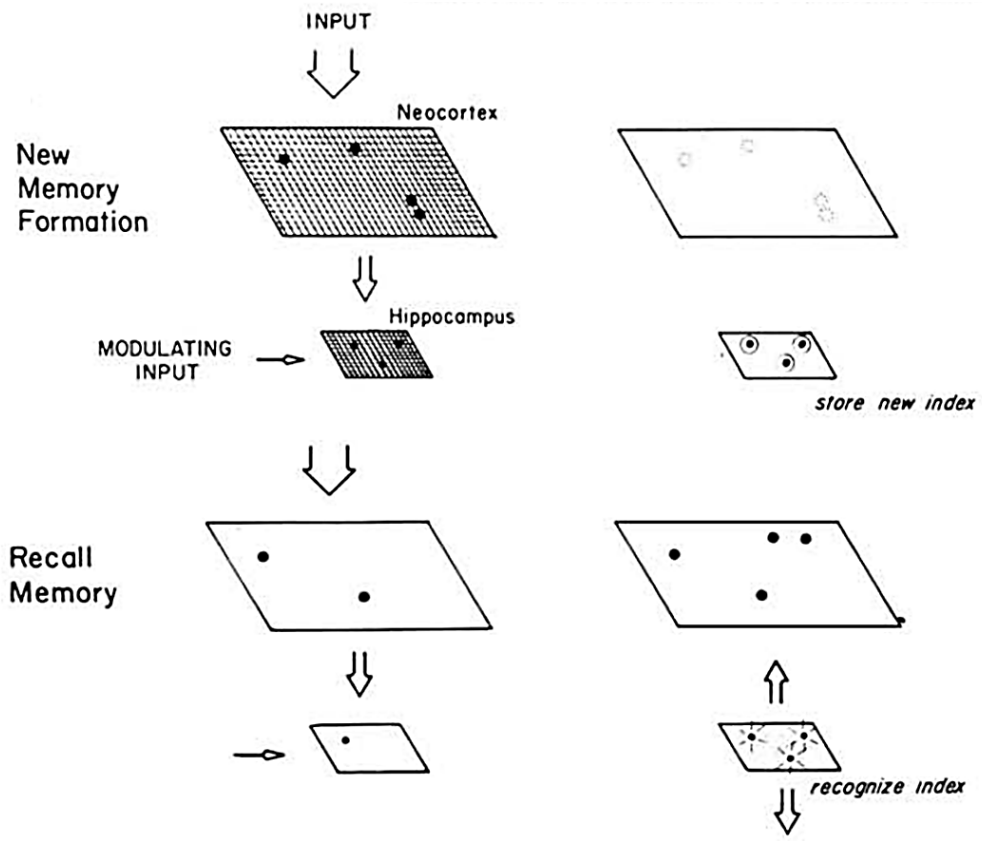

Figure 8 – Hippocampal memory indexing theory. Top, Mechanism of new memory formation. Experience activates multiple neocortical ensembles (black dots in neocortex), which activate specific hippocampal ensembles (black dots in HIPP). These hippocampal ensembles register (or index) the neocortical ensembles activated during the experience, and are stored tue to long-term plasticity mechanisms, persisting once the experience is finished. Bottom, Memory recall. Exposure to a subset of the information previously encoded activates only part of the established hippocampal index. Once a suprathreshold subset of the hippocampal index is activated, all the hippocampal index becomes active (back dots with sunbursts in HIPP), reinstating the full neocortical ensemble previously activate during the experience (black dots in neocortex). Adapted from (Teyler & DiScenna 1986).

3.5. HIPPOCAMPAL NETWORK ACTIVITY PATTERNS

Assuming that memories are supported by distributed ensembles of cortical and hippocampal neurons (Teyler & DiScenna 1986; Teyler & Rudy 2007) that are concurrently activated, synchronous neuronal activity is relevant for memory. Classically, brain rhythms are network activity patterns thought to provide synchronization, and thereby coordination, of the activity of distributed neurons during memory processes (for review, see (Buzsáki 2006)).

In vivo extracellular recordings in rats performing spatial navigation have shown different hippocampal network activity patterns, including theta oscillations, sharp-wave ripples (SWR), and gamma oscillations in the local field potential (LFP) (Figure 8) (for review, see (Colgin 2016)).

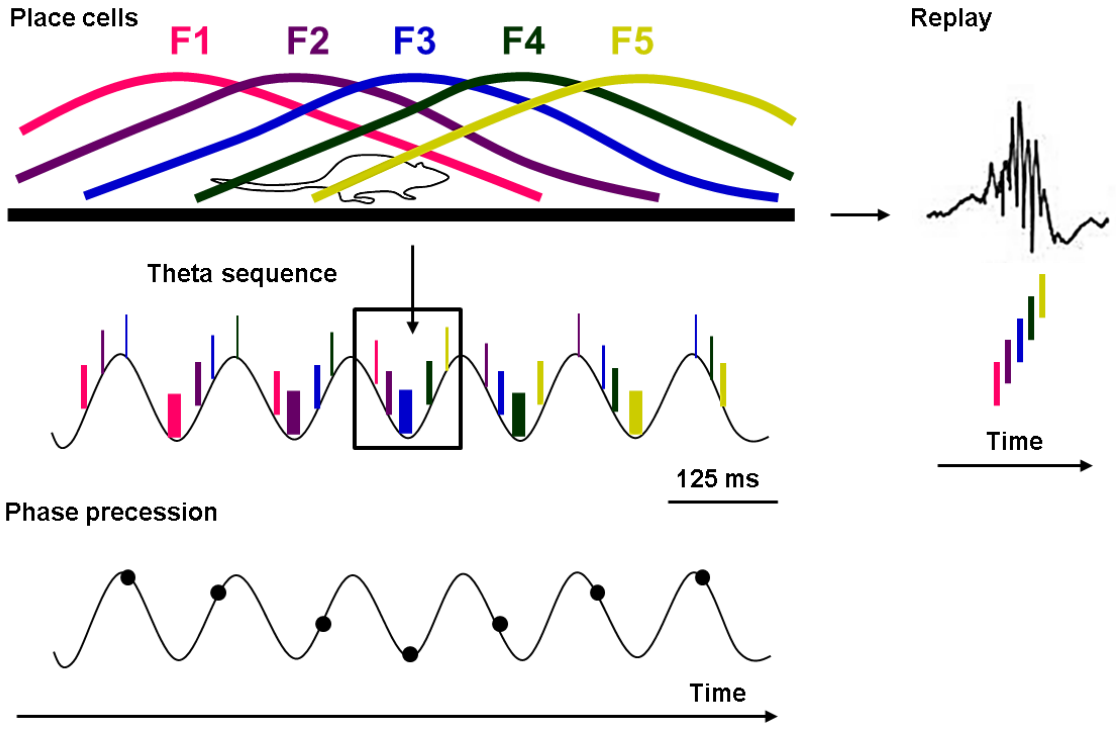

Figure 9 – Relation between place cells and hippocampal rhythms in freely behaving rats. While the rat is running in a linear track, hippocampal place cells display increased firing rate as the animal traverses each of their place fields. Five different place fields are depicted in the linear track (F1-F5). When the spikes of each place cell are aligned with the ongoing hippocampal theta oscillation (black waves on the left), for any given theta cycle (black rectangle), the spikes of place fields extending behind (pink) and ahead (light green) of the animal occur at different phases, producing a compressed representation of a spatial trajectory within each theta cycle (theta sequence) (Foster & Wilson 2007). More specifically, as the animal traverses each place field, the corresponding place cell will fire at earlier phases within each theta cycle (phase precession) (O'Keefe & Recce 1993; Skaggs et al. 1996). The sequences of place cells observed within each theta cycle during exploratory behavior can be reinstated during awake immobility, firing in compressed time scales but preserving the sequence detected during exploration (replay). Replay of spatial trajectories occurs during hippocampal SWR (Lee & Wilson 2002).

Theta oscillations are synchronous oscillations in the hippocampal LFP with frequency ranging from 4 to 12 Hz (for review, see (Buzsáki 2002; Colgin 2016)). This network pattern is particularly prominent during active exploration of the environment and during rapid eye movement (REM) sleep. Several studies have suggested a role for theta oscillations in learning and memory, based on their ability to coordinate groups of neurons, possibly linking different cells to produce the neuronal ensembles that represent each memory. This view is supported by the observation that ensembles of place cells spike in sequence within theta cycles, matching the succession of locations traversed by the animal during active exploration (Figure 9) (Dragoi & Buzsáki 2006; Foster & Wilson 2007; Skaggs et al. 1996). These sequences of place cells were termed theta sequences (Figure 9) (Foster & Wilson 2007). Crucially, the sequential firing of the place cells was disrupted upon theta oscillations blockade (Wang et al. 2015).

SWR are high frequency oscillations in the hippocampal LFP with frequency ranging from 150 to 250 Hz (for review, see (Buzsáki 2015; Colgin 2016)). This network pattern is particularly prominent at low movement speeds, during quiet wakefulness, during slow wave sleep, and during consummatory behaviors, originating from CA3 and propagating to CA1. During SWR, ensembles of hippocampal place cells are reinstated, firing in compressed time scales in relation to epochs of active exploration (Nádasdy et al. 1999; Lee & Wilson 2002). The sequence of firing of individual place cells in SWR matches their sequence of firing in the exploration epochs, providing a compressed, internal representation of the past trajectories actually traversed by the animals (Figure 9) (Kudrimoti et al. 1999; Karlsson & Frank 2009; Jadhav et al. 2012; Davidson et al. 2009; Nádasdy et al. 1999; Lee & Wilson 2002). This offline reinstatement observed during SWR has been proposed as a mechanism for memory consolidation, during slow wave sleep (Ego-Stengel & Wilson 2009; Ramadan et al. 2009), and for memory recall, during quiet wakefulness (Jadhav et al. 2012; Karlsson & Frank 2009) (for review on SWR in memory recall and consolidation, see (Joo & Frank 2018)). Disruption of SWR in rats performing a spatial memory task led to behavioral impairment, suggesting a role for SWR in awake animals during memory-guided trajectory planning (Jadhav et al. 2012).

Gamma oscillations are synchronous oscillations in the hippocampal LFP with frequency ranging from 25 to 55 Hz for slow gamma and 60 to 100 Hz for fast gamma (for review, see (Buzsáki & Wang 2012; Colgin 2016)). Fast gamma oscillations in CA1 are driven by

the medial EC, suggesting their relevance for the encoding of current sensory information in memory (Colgin et al. 2009; Belluscio et al. 2012; Kemere et al. 2013; Schomburg et al. 2014; Yamamoto et al. 2014; Cabral et al. 2014; Newman et al. 2013). Contrarily, slow gamma oscillations in CA1 are driven by CA3, and memory retrieval is thought to depend on CA3 (Schomburg et al. 2014; Kemere et al. 2013; Colgin et al. 2009; Belluscio et al. 2012).

Assuming that allocentric navigation requires encoding, retrieval, comparison, and choice, the HIPP would guarantee the encoding, storage, and recall of past trajectories, providing the alternatives for deliberation and behavior planning (Yu & Frank 2014; Foster & Knierim 2012).

3.6. THE FUNCTION OF THE MMC

The function of the MMC was first proposed by Vogt BA and colleagues (Vogt et al. 1992), who divided the MMC in anterior executive region and posterior evaluative region. The executive region (areas 24 and 25, ACC) was involved in controlling the output of visceromotor, endocrine, and skeletomotor systems, whereas the evaluative region (areas 29 and 30, RSC) played a role in monitoring the environment and in memory. This functional dichotomy was supported by further studies in humans, non-human primates, and rodents (Devinsky et al. 1995) (for review, see (Vogt & Gabriel 1993)).

It is generally accepted that ACC is necessary for motivated behavior or the willed control of action. Willed control of action implies overcoming inertia to initiate action and controlling competing neural processes, like habitual behaviors, innate tendencies, or salient distractors (Holroyd & Yeung 2012; Devinsky et al. 1995). It is, however, debatable whether ACC acts as a monitor, a controller, or an economic structure (for review, see (Heilbronner & Hayden 2016)). “Monitoring Theories” focus on ACC’s ability to track external and internal variables (Schall et al. 2002; Norman & Shallice 1986), whereas “Controlling Theories” postulate that ACC directly regulates actions, cognitive processes or other control processes (Morecraft & Van Hoesen 1998; Bush et al. 2000; Paus 2001; Rushworth et al. 2011; Holroyd & Yeung 2012; Heilbronner & Hayden 2016). Monitoring Theories” place the ACC outside of, or beside, the processes that transform inputs into

outputs or actions, whereas “Controlling Theories” place the ACC in the input-output transformation process.

Despite the conceptual disparities (reviewed in (Heilbronner & Hayden 2016)), the field is converging to the notion that ACC produces a cognitive map, but, more than purely spatial, this internal representation contains all the task-relevant variables, and has been known as *task set* (Reverberi et al. 2012) or *task space*. This notion is supported by the observation that ACC does encode a vast array of task-relevant variables, including variables related with task state (context) and variables that guide action (strategy) (Hayden & Platt 2010; Luk & Wallis 2013; Cowen et al. 2012; Remondes & Wilson 2013). Crucially, the variables encoded are inconsistent across studies, probably because their relevance changes across tasks, determining their encoding. The ACC acts, therefore, as a storage buffer, where the task set is encoded, linking contexts, strategies, and outcomes to guide actions (Heilbronner & Hayden 2016).

Studies in rodents have shown engagement of the MMC is spatial paradigms requiring (C. C. Lapish et al. 2008; Cowen et al. 2012; Remondes & Wilson 2013) and not requiring working memory, in acquisition of contextual fear conditioning (Corcoran et al. 2016), and in tasks requiring execution of spatial sequences (Remondes & Wilson 2015; Remondes & Wilson 2013). The engagement of the MMC in such a diversity of tasks suggests a central, rather than a specific role. While individual cingulate cells contained little spatial information, the activity of cingulate ensembles changed dramatically between environments (Hyman et al. 2012). Within each environment, this activity showed, however, little modulation by specific locations, unlike hippocampal place cells (Hyman et al. 2012). Dramatic changes in the activity of cingulate ensembles were also reported upon non-spatial changes, including changes in the task phase (Christopher C Lapish et al. 2008) or introduction of reward in the environment (Caracheo et al. 2013). The idea that ACC encodes a task space to guide action is a parsimonious explanation for those observations.

Regarding the RSC, it is generally accepted that RSC plays a role in spatial navigation and episodic memory (for review, see (Mitchell et al. 2018; Seralynne D Vann et al. 2009)), reinforcing Vogt’s conception of a posterior evaluative region. When trying to specify the exact function of RSC, studies used different behavioral tasks, leading to different conclusions. In summary, their proposals concerning RSC function fall into three major

categories, specifically (1) landmark processing; (2) mediation between spatial representations or reference frames; and (3) consolidation and retrieval of spatial maps.

The landmark processing hypothesis emerged from studies showing that RSC activity is modulated by manipulation of landmarks, defined as discrete objects or visual discontinuities in the environment. Some key findings included the observation that head-direction (HD) cells became less sensitive to landmarks upon RSC lesions (Clark et al. 2010), a subpopulation of HD cells in RSC responded to landmarks in preference to the main HD network activity (Jacob et al. 2017), and both human subjects (Iaria et al. 2007) and rodents (Vann & Aggleton 2005) showed decreased performance in allocentric navigation upon RSC lesions. This hypothesis is further reinforced by the strong connectivity between RSC, the visual cortices, and the HIPP (van Groen & Wyss 1990; van Groen & Wyss 1992; van Groen & Wyss 2003), placing the RSC in a strategic position to process perceived landmarks and use them to update hippocampal spatial maps. The latest update in the landmark processing hypothesis came from Auger and Maguire, who found a correlation between RSC activation and landmark stability/permanence (Auger et al. 2017). While this hypothesis has been influential, it implies that landmarks are a special category of object, with enhanced modulatory effect on RSC, something that is not clearly supported by experimental data as RSC is modulated by many other spatial variables. Since no studies clearly dissociated the influence of landmarks vs. global environment and other spatial variables in RSC activity, RSC might be modulated by spatial variables and their stability beyond just landmarks.

The mediation hypothesis (reviewed in (Seralynne D. Vann et al. 2009)) emerged from studies in which behavioral tasks required switching between different representations of the same spatial information or between reference frames (egocentric vs. allocentric; proximal vs. distal cues; local vs. global environment). In such tasks, RSC was found to produce a conjunctive map of both egocentric and allocentric variables (Alexander & Nitz 2015). The core idea here is that spatial learning might occur in the absence of RSC, but RSC is needed when the subject moves between representational modes.

The consolidation and retrieval hypothesis came from studies addressing spatial learning over extended temporal windows, and suggests that RSC is required when animals need to use and update previously learned spatial maps. This influential hypothesis is supported by many studies showing that RSC engaging is frequently time-limited (Maviel

et al. 2004; Nonaka et al. 2017). More specifically, there seems to be a 24h time window after training, above which RSC shows increased activity (Buckley & Mitchell 2016).

While the hypotheses referred show numerous disparities, they all share a common aspect, specifically the relevance of RSC in tasks requiring switching, merging and comparison of representations, for instance, egocentric vs. allocentric and recent vs. remote. The RSC could act, therefore, as a short-term buffer for the representations as they are compared and merged (Seralynne D. Vann et al. 2009). Interestingly, this integrated notion of RSC function and its ability to build an internal representation has many parallels with the concept of task space advanced in ACC literature.

3.7. HIPP-MMC INTERACTION IN SPATIAL WORKING MEMORY

Spatial working memory (SWM) consists in the online processing (update, maintenance, and retrieval) of trial-specific spatial information in the service of goal-directed spatial navigation. While previous studies have shown that SWM requires the HIPP-mPFC interaction in the rat (for review, see (Wirt & Hyman 2017)), the HIPP-MMC interaction in SWM has received less attention.

Remondes and Wilson found that cingulate neurons phase-lock to and are modulated by several hippocampal network patterns, including theta oscillations, gamma oscillations, and SWR, while rats perform a SWM task involving spatial sequences. During quiet wakefulness, cingulate and hippocampal neural activity showed a SWR-triggered increase in slow gamma phase coherence, and cingulate neurons responded to hippocampal SWR (Remondes & Wilson 2015). During locomotion, the HIPP-ACC theta phase coherence was strongest at the choice points of the wagon wheel maze (Remondes & Wilson 2013). Further studies addressing HIPP-RSC interaction in SWM are lacking. While these reports suggest a role for the HIPP-MMC interaction in SWM, this interaction was also observed in other behaviors and tasks devoid of SWM, including grooming, rearing, locomotion, and immobility (Young et al. 2009) and during exploration (Corcoran et al. 2016). The HIPP-MMC interaction might, therefore, play a role in SWM, but a general, rather than specific, role in processing the necessary spatial information.

Studies involving manipulations in ACC, RSC, or HIPP provided conflicting evidence to the hypothesis that HIPP-MMC interaction plays a role in SWM. Inactivation of the RSC (Keene & Bucci 2009; Pothuizen et al. 2010), and HIPP (Hallock et al. 2013) impaired animals' performance in paradigms requiring SWM. Other studies, however, did not support the formers (Neave et al. 1994; Mao & Robinson 1998), and inactivation of the ACC did not impaired animals' performance in paradigms requiring SWM (Ragozzino et al. 1998; Neave et al. 1994). Crucially, the absence of effect could be attributed to other factors, including incomplete lesion of the target regions (see Figure 4 in (Ragozzino et al. 1998)), and low spatial component in the behavioral task (Neave et al. 1994; Mao & Robinson 1998).

II

Techniques

II. TECHNIQUES

1. ANTEROGRADE NEURONAL TRACING

Method used to trace axons from their source (soma) to their termination point. This technique relies on the injection of chemical tracers with a detectable tag or viral vectors encoding fluorescent tags, which are locally incorporated in the soma, filling the neurons and allowing the visualization of their axonal projections (Figure 10). Monosynaptic tracers are not transported across synapses, signaling the neurons that send direct output from the injection site. All anterograde tracers reported in the dissertation are monosynaptic.

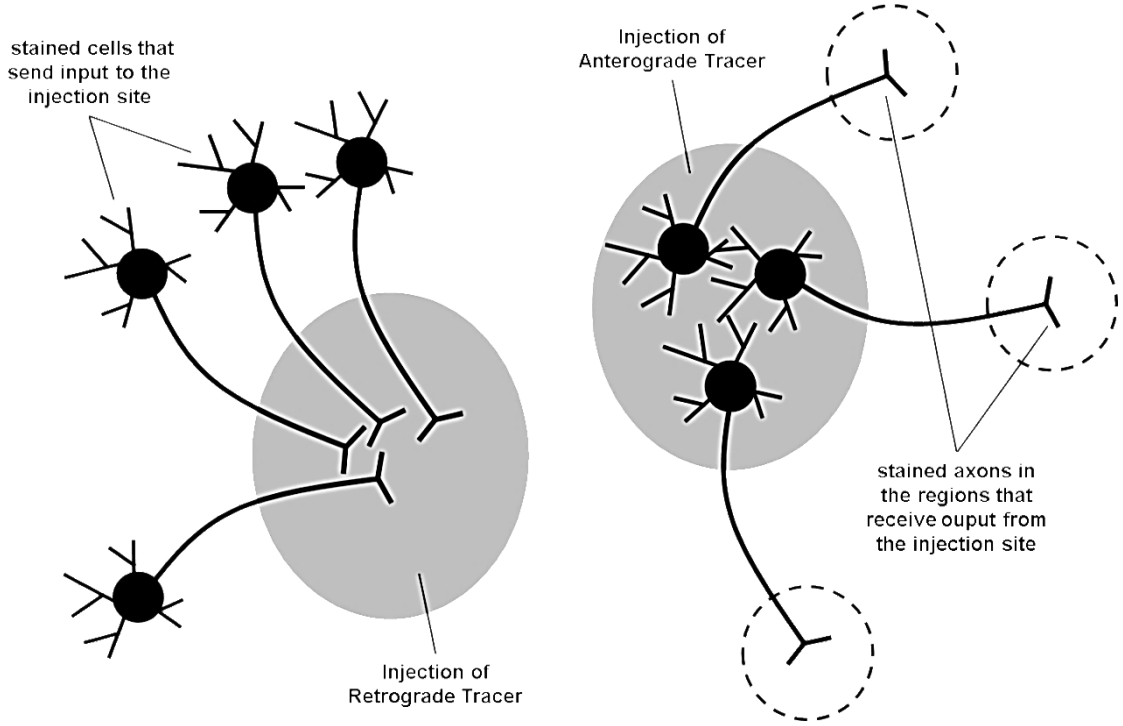

Figure 10 – Mechanism of action of neuronal tracers. Left, Monosynaptic retrograde tracers are incorporated by the axon terminals and travel towards the soma, producing detectable inclusions in the neurons sending input to the injection site. Right, Monosynaptic anterograde tracers are incorporated by the cell bodies and fill the neurons. Filled axons can be traced, allowing the identification of the regions receiving output from the injection site.

2. RETROGRADE NEURONAL TRACING

Method used to trace axons from their termination point to their source. This technique relies on the injection of chemical tracers with a detectable tag or viral vectors encoding fluorescent tags, which are locally incorporated in the axon terminals and travel towards the soma, producing detectable inclusions (Figure 10). Monosynaptic tracers are not transported across neurons, signaling the neurons that send direct input to the injection site. All retrograde tracers reported in the dissertation are monosynaptic.

3. ELECTROPHYSIOLOGY - INTRACELLULAR RECORDINGS

Method used to measure ionic currents or voltage changes across the cell membrane of individual neurons (for review, see (Johnston & Wu 1995)). It requires the insertion of a microelectrode in the intracellular space of a neuron. The standard microelectrodes are glass pipettes, filled with a solution chemically similar to the intracellular fluid of the neuron and containing a chloride silver wire. The voltages measured by the recording electrode are compared with the voltage of a reference electrode, which consists in a silver chloride-coated silver wire placed in the extracellular medium.

Intracellular recordings can be performed in voltage clamp mode, in which case the voltage across the cell membrane is clamped and the resulting currents are recorded, or in current clamp mode, in which case the membrane potential is not clamped and voltage changes resulting from current injections are recorded. Currently, the patch clamp technique is the standard technique used for intracellular recordings, and there are many variations of the technique depending on the purpose (for review, see (Johnston & Wu 1995)). The whole cell patch clamp technique is the most common in literature, and is used to measure ionic currents through multiple channels simultaneously, over the membrane of the whole neuron. In whole cell configurations, the pipette containing the electrode is attached (sealed) to the cell membrane and the membrane is ruptured through application of negative pressure or a current pulse. By rupturing the cell membrane, the pipette gains access to the intracellular space. This allows the recording

of the ionic currents in the whole cell and guarantees better electrical access (lower resistance) to the intracellular space.

4. ELECTROPHYSIOLOGY - EXTRACELLULAR RECORDINGS

Method used to measure the voltage changes associated to the current sinks and sources distributed along a local population of neurons (for review, see (Buzsáki et al. 2012; Buzsáki 2006; Johnston & Wu 1995)). This procedure is applied to *in vitro* preparations (e.g. acute brain slices), and *in vivo* preparations (e.g. anesthetized and freely behaving rodents).

At small scale, which implies the use of microelectrodes (tip diameter 1 to 25 µm) and proximity between the microelectrodes and the soma of the neurons (50 to 140 µm), extracellular recordings capture actions potentials (spikes) from single neurons. The distance is crucial to capture spikes because the extracellular medium has low resistance and ionic currents are relatively slow, attenuating fast-rising events. At higher scale, which implies increasing electrodes' diameter or increasing the distance between the microelectrodes and the soma of the neurons, extracellular recordings capture local field potentials (LFP). The LFP reflects the linear summation of overlapping fields produced by current sinks and sources distributed along a local population of neurons. The post-synaptic events are the major contributors to the LFP because they have higher duration and happen in more cells than the spikes, thus having higher chance to happen simultaneously, leading to summation and less attenuation.

5. NON-IMPLANTABLE MULTI-ELECTRODE ARRAY (MEA)

Device containing multiple plates (or contacts) through which neural signals are recorded or delivered, acting as an interface between neural tissue and electronic microcircuitry. This system is used for high-throughput *in vitro* extracellular recordings. The first non-

implantable MEA was developed by (Thomas et al. 1972) to record from cultured cells, but commercial options are now available. We used the MEA2100-System® platform, whose architecture and components are depicted in Figure 11. Regarding the MEA to serve as the interface between the neural tissue and the platform, we used the 60MEA200/30iR-Ti configuration. These MEAs are made of 60 titanium nitride (TiN) electrodes, in a 8x8 grid, with electrode spacing of 200 µm and electrode diameter of 30 µm.

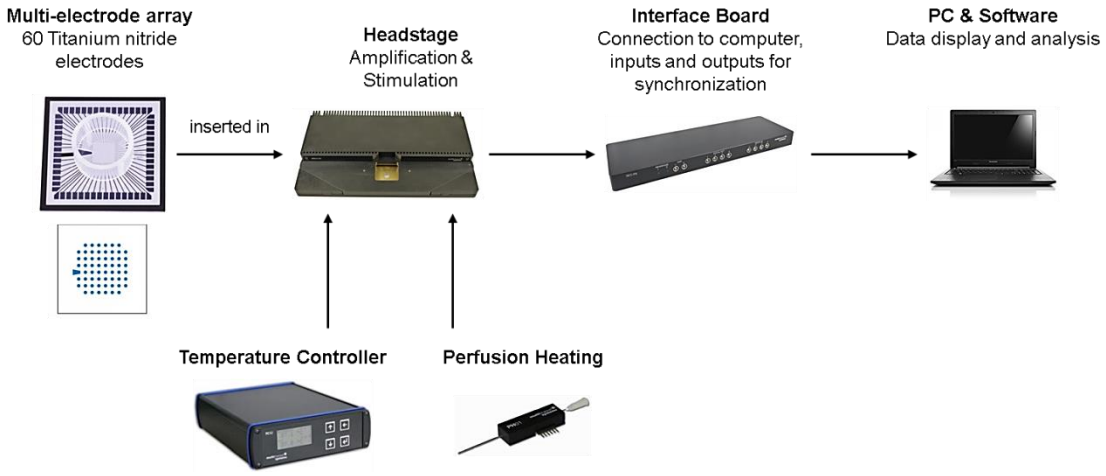

Figure 11 – MEA2100-System® platform. The MEA2100S platform consists of two main devices: the headstage and the interface board. The headstage is equipped with amplifiers, an analog-to-digital converter ADC, and a stimulus generator, whereas the interface board contains an integrated signal processor, assures the connection to the computer, and performs synchronization of inputs and outputs. A temperature controller and a perfusion heating device control the temperature throughout the experiments.

6. CHRONIC IMPLANTABLE HYPERDRIVE WITH MOVABLE TETRODES

Device containing multiple movable microelectrodes through which neural signals are recorded, acting as an interface between the brain tissue and electronic microcircuitry (Figure 12). This system is used for chronic *in vivo* extracellular recordings in freely behaving rodents (for review, see (Kloosterman et al. 2009; Nguyen et al. 2009)). The microelectrodes used are tetrodes, which consist in four gold-plated wires (12 to 15 µm in diameter each) twisted together. Tetrodes (Gray et al. 1995) enhance the discrimination

of single cells as they allow the triangulation of the neurons (for review, see (Buzsáki 2006)).

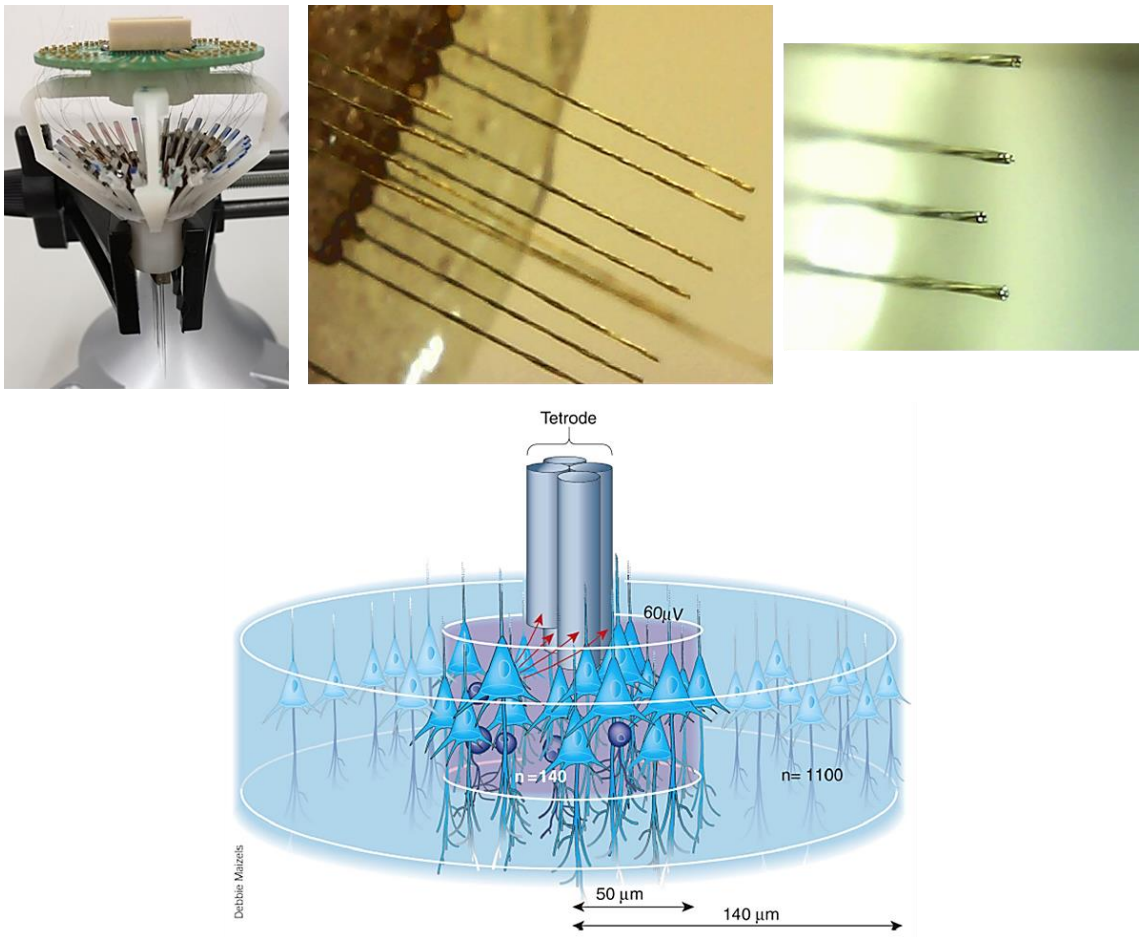

Figure 12 – Chronic implantable hyperdrive with movable tetrodes. *In vivo* electrophysiological recordings in freely-behaving animals require chronic implantable drives through which microelectrodes, most commonly tetrodes, can be inserted into the nervous system to record neural signals. While drives can have several designs, the SLIQ drive (Liang et al. 2017) (top left panel) became popular as a light and flexible drive, capable of accommodating up to 32 independently movable tetrodes for chronic *in vivo* recordings. Tetrodes, four gold-plated wires twisted together (top right panel), are arranged in bundles, whose dimensions are ajusted according to the coordinates of the target brain regions. Once neurons are recorded, spikes are assigned to each individual neuron. Spike assignment is ambiguous if single electrodes are used as neurons that are located at the same distance from the tip in a sphere provide similar amplitude spikes. By using microelectrodes containing two closely spaced electrodes, ambiguity can decrease to neurons in a plane, with three electrodes ambiguity decrase to neurons in a line, and with four electrodes the spatial position of each neuron in the line can be triangulated. This explains why tetrodes became popular as they allow triangulation of the three dimensional position of neurons due to voltage differences between the four wires when spikes from individual neurons are detected and recorded (bottom panel). Bottom planel adapted from (Buzsáki 2004).

7. OPTOGENETICS

Technique in which light is used to manipulate living cells (e.g. neurons) that were genetically modified to express light-sensitive ion channels (for review, see (Fenno et al. 2011)). In the present work, we used ChR2 (for review, see (Deisseroth & Hegemann 2017; Lin 2011; Nagel et al. 2003)). ChR2 is a rhodopsin that acts as a light-switched, cation-selective ion channel. This channel opens rapidly after absorption of a photon (typically with wavelengths corresponding to blue light), generating influx of monovalent and divalent cations, leading to optical excitation of neurons. First isolated from *Chlamydomonas reinhardtii*, ChR2 has been genetically engineered to be expressed in specific types of mammalian neurons.

In this work, we used the constructs AAV_9.CaMKIIa.hChR2(H134R)-mCherry.WPRE.hG and AAV_9.CAG.hChR2-mCherry . In this case, ChR2 is delivered to the neurons via an adeno-associated virus (AAV), and its expression is constrained to the target cells through the selection of a specific promoter (e.g. CamKIIa, promoter for excitatory neurons; CAG, pan-neuronal promoter). In-frame fusion with fluorescent tags (e.g. mCherry) optimizes the visualization of ChR2-expressing cells, while ChR2 itself has modified codons to optimize its expression in mammalian cells (hChR2). Using such constructs, ChR2 has been widely used in *in vitro* and *in vivo* systems for fast, reversible, and cell-specific excitation of neurons.

8. DESIGN RECEPTORS EXCLUSIVELY ACTIVATED BY DESIGNER DRUGS (DREADD)

Technique in which synthetic small molecule chemical actuators are used to manipulate living cells (e.g. neurons) that were genetically modified to express chemogenetically engineered proteins capable to interact with such actuators (for review, see (Roth 2016)). In the present work, we used $hM4D_i$ (for review, see (Zhu & Roth 2014)). hM4Di is a modified human M4 muscarinic receptor. This modified receptor has low affinity for endogenous ligands, has little constitutive activity, and can be activated upon interaction

with clozapine N-oxide (CNO), triggering a G_i cascade and silencing neuronal activity. CNO, the synthetic small molecule chemical actuator, is a clozapine metabolite, which is *considered* biologically inert in rodents and with low affinity for endogenous receptors. Whether CNO is completely inert is, however, debatable (MacLaren et al. 2016; Manvich et al. 2018).

In this work, we used the construct AAV_8.CaMKIIa.hM4D(G_i)-mCherry. As for ChR2, the DREADD is delivered to the neurons via an adeno-associated virus (AAV), and its expression is constrained to the target cells through the selection of a specific promoter (e.g. CamKIIa, promoter for excitatory neurons). In-frame fusion with fluorescent tags (e.g. mCherry) optimizes the visualization of DREADD-expressing cells. Using such constructs, DREADDs have been widely used in *in vitro* and *in vivo* systems for sustained (60-90 min), reversible, and cell-specific inhibition of neurons.

9. DNMTP TASK

The DNMTP task is widely used to evaluate SWM in animals (Dudchenko 2004). The task consists in 3 phases, namely the Sample Run, the Delay Period, and the Test Run, and is typically performed in a T maze (Figure 13). In the Sample Run, the animal is forced to turn left or right, and receives a reward at the end of the arm. A delayed is imposed between the Sample Run and the Test Run (typically 15 s). In the Test Run, the animal has a free choice, but only the arm not visited in the Sample Run has a reward at the end.

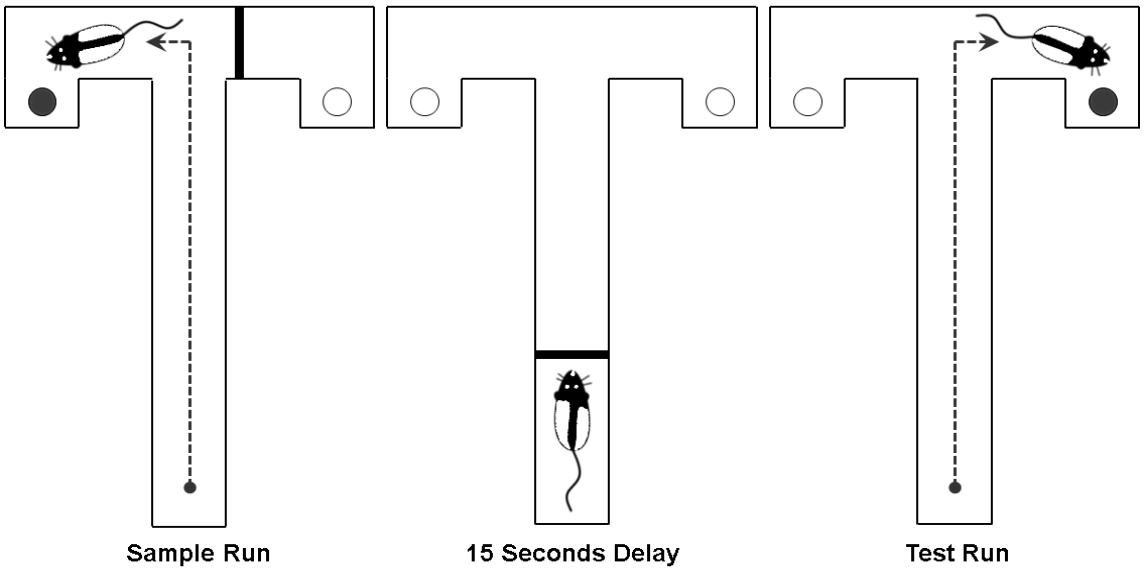

Figure 13 – DNMTP task.

III

Aims

III. AIMS

The present dissertation aims at:

1) Quantifying the hippocampal populations projecting to the divisions of the MMC, using a retrograde neuronal tracer;
2) Quantifying the hippocampal axons in the divisions of the MMC, using an anterograde neuronal tracer;
3) Assessing whether the hippocampal axons form functional synapses onto the MMC, using the MEA2100-System® coupled with optogenetic stimulation of the hippocampal terminals in acute cortical slices of the MMC;
4) Characterizing the spatiotemporal dynamics of the hippocampal-evoked responses in the divisions of the MMC, at the microcircuit level, using the MEA2100-System® coupled with optogenetic stimulation of the hippocampal terminals in acute cortical slices of the MMC;
5) Correlating the activity of the HIPP with the activity of the MMC in the encoding, maintenance, and retrieval phases of a DNMTP task, using coherence analysis applied to the LFP and multi-unit activity (MUA);
6) Characterizing the changes in population activity in the HIPP and in the MMC in the encoding, maintenance, and retrieval phases of a DNMTP task, using power spectral analysis applied to LFP and MUA;
7) Testing the necessity of the HIPP-MMC interaction in the DNMTP task, using DREADDs to inhibit the HIPP.

IV

Materials and Methods

IV. MATERIALS AND METHODS

Table 2 – Stereotaxic injections.

Experiment	Coordinates (A/P*, M/L*, D/V**)
Retrograde Tracing (CTB Alexa Fluor 647)	Single, Unilateral Injection ACC (+2.0, +0.5, -2.3); 0.5 µL (n = 1, A) ACC (+1.0, +0.5, -2.0); 0.5 µL (n = 3, B) MCC (-1.0, +0.5, -1.5); 0.5 µL (n = 3, C) RSC (-4.0, +0.5, -1.5); 0.5 µL (n = 1, D) RSC (-5.0, +0.5, -1.5); 0.5 µL (n = 1, E) RSC (-7.0, +1,0, -1.5); 0.5 µL (n = 1, F)
Anterograde Tracing (AAV_9.CaMKIIa.hChR2(H134R)-mCherry.WPRE.hG)	Single, Unilateral Injection (-5.0, +4.0, -2.4); 0.5 µL (n = 3)
Anterograde Tracing AAV_9.CAG.hChR2-mCherry	Single, Unilateral Injection (-5.0, +4.0, -2.4); 0.5 µL (n = 3)
MEA AAV_9.CaMKIIa.hChR2(H134R)-mCherry.WPRE.hG	Double, Unilateral Injection (-5.0, +4.0, -2.4); 0.5 µL; (-5.0, +5.5, -4.4); 1 µL (n = 3)
MEA AAV_9.CAG.hChR2-mCherry	Double, Unilateral Injection (-5.0, +4.0, -2.4); 0.5 µL; (-5.0, +5.5, -4.4); 1 µL (n = 3)
Implant Surgeries AAV_8.CaMKIIa.hM4D(G_i)-mCherry	Single, Bilateral Injection (-5.0, +4.0, -2.4); 0.5 µL

* from bregma. ** from the surface of the brain.

1. ANIMALS

All rats were obtained from Charles River. For the anatomical experiments and neuronal tracing, we used 16 male Wistar rats (300-400 g). For the *in vitro* extracellular recordings coupled with optogenetic stimulation of the hippocampal axons, we used 11 male Sprague-Dawley rats (300-400 g). For the *in vivo* extracellular recordings and behavioral experiments, we used 2 male Long-Evans rats (3-6 months old or 400-600 g at implantation). Rats were housed in groups of two or three, provided with *ad libitum* food and water, and monitored in a room with controlled temperature and a 12 hour

light/dark cycle. For *in vivo* recordings and behavioral experiments, rats were singly housed and food deprived to 85% of their *ad libitum* weight following the implant surgery. All experiments and procedures were approved by the Portuguese National Authority for Animal Health, Direcção-Geral de Alimentação e Veterinária (DGAV).

2. VIRAL CONSTRUCTS

The AAV_9.CaMKIIa.hChR2(H134R)-mCherry.WPRE.hG was acquired from the University of Pennsylvania Vector Core. The AAV_9.CAG.hChR2-mCherry was gently provided by Marta Moita at the Champalimaud Centre for the Unknown. The AAV_8.CaMKIIa.hM4D(G_i)-mCherry was acquired from the University of North Carolina (UNC) at Chapel Hill Vector Core. Viral titers were 4.77 x 10^{13} GC mL^{-1} for AAV_9.CaMKIIa.hChR2(H134R)-mCherry.WPRE.hG, and ranged from 1 x 10^{12} to 8 x 10^{12} CG mL^{-1} for AAV_9.CAG.hChR2-mCherry and for AAV_8.CaMKIIa.hM4D(G_i)-mCherry.

3. ANATOMY

3.1. RETROGRADE NEURONAL TRACING

For retrograde neuronal tracing, we used cholera toxin subunit B (CTB) conjugated to Alexa Fluor 647 diluted in phosphate buffered saline (PBS) solution to achieve a final concentration of 0.5% WT vol^{-1}. Diluted CTB was aliquoted and stored at -20°C. Ten Wistar male rats received a 500 nL injection of diluted CTB in the MMC, and were used to quantify the hippocampal cells projecting to the MMC. Seven to 11 days after injection, rats were perfused for histological analysis and imaging. The coordinates used in the injections are depicted in Table 2. This protocol was based on (Varela et al. 2014; Conte et al. 2009), with modifications.

3.2. ANTEROGRADE NEURONAL TRACING

For anterograde neuronal tracing, 3 male Wistar rats received a 500 nL injection of AAV_9.CaMKIIa.hChR2(H134R)-mCherry.WPRE.hG in diHIPP to study the laminar distribution of the hippocampal excitatory axons across the MMC. Three additional male Wistar rats received a 500 nL injection of AAV_9.CAG.hChR2-mCherry in diHIPP to study the laminar distribution of the hippocampal excitatory and inhibitory axons in the MMC, as the HIPP-MMC projection included long-range GABAergic neurons. Thirty days after injection, rats were perfused for histological analysis and imaging. The coordinates used in the injections are depicted in Table 2. This protocol was based on (Morgenstern et al. 2016), with modifications.

3.3. STEREOTAXIC SURGERY

Rats were induced in an induction chamber with 5% isoflurane. Once the animals lost the righting reflex, they were weighted and received an intraperitoneal injection of a cocktail containing ketamine (25 mg/kg) and xylazine (3 mg/kg), followed by subcutaneous injection of Carprofen. During the entire surgery, anesthesia was maintained with 1-2% isoflurane, animals were placed onto a heating pad, and eye ointment was regularly applied. Rats were shaved, and had Lidocaine applied to the ears and to the surgical site. Once the animals lost the paw withdrawal reflex, they were placed in the stereotaxic apparatus, and the surgical site was scrubbed 3 times with 10% povidone iodine followed by 70% ethanol. A sagittal incision was made along the sagittal suture, the skin was retracted, and the muscle and *periosteum* were scrapped away from the skull. The injection sites were marked using a needle placed into the mount of the stereotaxic device. The craniotomies were performed with a Dremel drill, and the *dura mater* was excised with a curved needle to expose the brain surface. The anatomical tracers or viral constructs were pressure injected using a stereotaxic injector assembled in-house and glass micropipettes (average internal tip diameter ranging from 20 to 50 µm). Micropipettes were filled with mineral oil, and silicon grease was applied in the interface between the micropipette and the plunger. All micropipettes containing bubbles were

discarded. Micropipettes were placed in the stereotaxic injector, and they were filled with the target volume of tracer and washed with saline solution. Micropipettes were lowered at the center of the craniotomies until they reach the target depth. Injections were performed at a rate of 50 µL/ min. To minimize the injection track, micropipettes were left in place for 15 minutes after injection, and were removed at a rate of 0.5 mm/min. Once the micropipettes were removed, the surface of the brain was rinsed with saline solution, and the surgical wound was sutured. Rats received 5 mL of Ringer's lactate solution subcutaneously, and were placed in a warm recovery area. All injection sites were verified histologically. This protocol was based on (Conte et al. 2009), with modifications.

3.4. IMMUNOHISTOCHEMISTRY

Rats were sacrificed through isoflurane overdose and transcardially perfused with 200 mL of PBS, followed by 500 mL of 4% paraformaldehyde (PFA). Brains were removed and placed in a postfix solution of 4% PFA for 24 hours, at 4°C. Fixed brains were equilibrated in a solution of 30% sucrose in 4% PFA, embedded in gelatin, and frozen. Coronal brain sections (100 µm) were prepared using a cryostat (Leica, CM3050 S). For retrograde and anterograde neuronal tracing, free-floating sections were incubated in 1µg/ mL of DAPI (Sigma) for 20 min and mounted in Mowiol (Sigma). For neurochemical characterization, free-floating sections were incubated in 0.1 M PBS containing 0.5 % Triton X-100 for 15 min at room temperature (RT), followed by an incubation in 0.1 M PBS containing 10% rabbit serum (RS) and 1% bovine serum albumin (BSA) for 1h at RT. Sections were then incubated in blocking solution containing primary antibody (dilution 1:500) for 48 h, at 4°C, in a humidity controlled chamber. The primary antibody was a polyclonal anti-GAD65/67 antibody raised in rabbit (Sigma-Aldrich, G5163). Stained sections were washed 3 times (15 min each) in PBS and were placed in blocking solution containing secondary antibody (dilution 1:200) overnight at 4°C. The secondary antibody was goat anti-rabbit IgG conjugated with Alexa Fluor 488 (ThermoFisher, A-11008). Stained sections were washed 3 times (15 min each) in PBS, were incubated in 1µg/ mL of DAPI

for 20 min and mounted in Mowiol. This protocol was based on (Miyashita & Rockland 2007), with modifications.

3.5. MICROSCOPY AND IMAGE ANALYSIS

For retrograde neuronal tracing, coronal slices were imaged in an Axio Observer widefield fluorescence microscope (Zeiss) equipped with an Axiocam 506 mono CCD (Zeiss). Zeiss filter sets number 49 (DAPI) and 50 (Cy5) were used to observe DAPI and CTB-Alexa Fluor 647, respectively.

For neuronal tracing and neurochemical characterization, confocal images were obtained with a LSM 880 point-scanning microscope with Airyscan (Zeiss) using a 20x plan-apochromat objective (0.80 numerical aperture) or a 40x plan-apochromat objective (0.95 numerical aperture). Fluorophores were excited using a 405 nm diode, a 488 nm argon, a 561 nm diode-pumped solid-state (DPSS), and a 633 nm helium-neon lasers. The detection intervals were set at 420-480 nm for DAPI, 500-550 nm for Alexa Fluor 488, 571-620 for mCherry, and 643-700 nm for Alexa Fluor 647.

For retrograde neuronal tracing, CTB-positive cells were manually counted in 15 slices *per* animal. The slices selected spanned the entire anterior-posterior axis of the HIPP and were 100 µm apart. To study the distribution of the cells across the anterior-posterior axis of the HIPP, the HIPP was divided in dHIPP (from -3.0 mm AP to -4.0 mm AP), diHIPP (from -4.0 mm AP to -6.0 mm AP, above the rhinal fissure), and vHIPP (from -4.0 mm AP to -6.0 mm AP, below the rhinal fissure). The DAPI staining was used to identify the position of the cells across the hippocampal *strata*. The numbers of CTB positive cells were grouped in ACC, MCC, and RSC ('region'), and, within each group, were grouped according to the anterior-posterior axis of the HIPP (dHIPP, diHIPP, and vHIPP, 'hippAP') or according to the hippocampal *strata* (SO, SP, SR, SR-SLM, 'strata'). Differences in the numbers of CTB positive cells were tested using N-Way ANOVA {'region', 'hippAP'} and N-Way ANOVA {'region', 'strata'}. Bonferroni's correction was applied to the multiple comparisons.

For anterograde neuronal tracing, mCherry positive axons were manually counted using Fiji software. Eleven slices *per* animal were quantified, for both constructs

(CaMKIIa.hChR2 and CAG.hChR2). Three slices (200 µm apart) contained the ACC (subarea 24a), 4 (200 µm apart) contained the MCC (subarea 24a'), and 4 (500 µm apart) contained the RSC (subarea 29c). The quantification was performed in a ROI of 255 µm x 1169 µm. For manual quantification, 8 lines (orthogonal to L1 and 25 µm apart) were drawn across the ROI and the intersecting axons were counted. For each individual slice, axon density in each layer (L1 to L6) was computed by dividing the total number of axons counted in each layer by the thickness of that layer (subareas 24a and 24a': L1, 210 µm; L2, 65 µm; L3, 177 µm; L5, 210 µm; L6, 370 µm; subarea 29c: L1, 160 µm; L2, 45 µm; L3, 68 µm; L4, 68 µm; L5, 365 µm; L6, 273 µm). Axon densities were grouped in ACC, MCC, and RSC ('region'), and, within each group, were grouped in superficial (L1-L4) and deep (L5-L6) ('layer'). Differences in axon density were tested using N-Way ANOVA {'region', 'layer'}. Bonferroni's correction was applied to the multiple comparisons. The DAPI staining and the reference values indicated above for the thickness of the layers ((Paxinos & Watson 2006)) were used to identify the position of the axons across the cortical layers. mCherry fluorescence was also measured along the cortical axis (as in (Morgenstern et al. 2016)). Fluorescence values were background corrected (subtraction of the mode), normalized, and the corresponding regions were averaged across rats. Colocalization analysis was performed using the Colocalization Threshold plugin (Fiji) as in (Temido-Ferreira et al. 2018).

4. IN VITRO ELECTROPHYSIOLOGY

4.1. OPTOGENETICS AND ACUTE CORTICAL SLICE ELECTROPHYSIOLOGY

Eight male Sprague-Dawley rats received two unilateral injections of AAV_9.CaMKIIa.hChR2(H134R)-mCherry.WPRE.hG, and 3 male Sprague-Dawley rats received two unilateral injections of AAV_9.CAG.hChR2-mCherry in diHIPP. The coordinates used in the injections are depicted in Table 2. Four to 6 weeks post-injection (CaMKIIa.hChR2) and 4 weeks post-injection (CAG.hChR2), rats were decapitated under deep isoflurane anesthesia and the brain was removed. After decapitation, the whole

brain was removed and submerged in ice-cold oxygenated (95% O_2, 5% CO_2) dissection solution [in mmol/L: sucrose 110, KCl 2.5, $CaCl_2$ 0.5, $MgCl_2$ 7, $NaHCO_3$ 25, NaH_2PO_4 1.25, glucose 7 (pH 7.4)]. After cooling for 3 minutes, the anterior and posterior portions were trimmed to produce a 7 mm block, and the block was glued to the stage of a vibratome (Leica VT1200S) with cyanoacrylate. Coronal slices at an angle of 10° to the vertical line were cut at 400 µm in ice-cold, oxygenated dissection solution, and gently transferred to a chamber containing oxygenated (95% O_2, 5% CO_2) artificial cerebrospinal fluid (aCSF) [in mmol/L: NaCl 124, KCl 3, NaH_2PO_4 1.25, $NaHCO_3$ 26, $MgSO_4$ 1, $CaCl_2$ 2, glucose 10 (pH 7.4)] at 35°C for 20-25 min. The aCSF Slices were transferred to a final storage chamber containing oxygenated aCSF at RT (20-25°C). This protocol was based on (Rombo et al. 2014; Rombo et al. 2016; Lu et al. 2014), with modifications.

4.2. ELECTROPHYSIOLOGICAL RECORDINGS

Evoked responses were recorded using the MEA2100-System® with a 60-channel multi-electrode insert (60MEA200/30iR-Ti). The diameter of each electrode was 30 µm, and the 60 electrodes were arranged in an 8 x 8 square with an inter-electrode distance of 200 µm. After 45 to 60 min in aCSF at RT, a slice was placed on the 8 x 8 array and immobilized with a nylon-mesh anchor. The slice was perfused with oxygenated aCSF at 2 mL/ min and at 30°C. To determine the optimal stimulation site, blue light from an LED was focused in different regions of the slice until evoking maximal network responses, at an intensity corresponding to 30mW total LED power, with pulse duration of 100 ms, and with interpulse interval of 10s. The response was allowed to stabilize for 10 min and the experimental protocol was started. For rats injected with CaMKIIa virus, each slice was sequentially recorded in control aCSF (20 min; condition CT_{CAM}), in aCSF with PTX (PTX, 50 µM; 20 min; condition $T1_{CAM}$), in aCSF with PTX and CNQX (CNQX, 20 µM; 20 min; condition $T2_{CAM}$), and in aCSF with PTX, CNQX, and APV (APV, 50 µM; 20 min; condition $T3_{CAM}$). For rats injected with CAG virus, each slice was sequentially recorded in control aCSF (condition CT_{CAG}), in aCSF with CNQX (condition $T1_{CAG}$), in aCSF with CNQX and APV (condition $T2_{CAG}$), and in aCSF with CNQX, APV, and PTX (condition $T3_{CAG}$). Drug concentrations and incubation times were the same as for rats injected with CaMKIIa

virus. Responses were amplified and digitized at 50 kHz. Slice position in the MEA was captured using a monochromatic camera (Celestron), and the expression of the optogenetic tool was verified histologically for each slice. This protocol was based on (Hass & Glickfeld 2016; Lu et al. 2014), with modifications.

4.3. DATA ANALYSIS AND STATISTICS

Responses were downsampled to 2 kHz in MC_Rack. Baseline correction and further analyses were carried out in MATLAB. For each slice from rats injected with CaMKIIa virus, we compared the average slope of the responses in the last 2 min of CT_{CAM} *versus* the last 2 min of $T3_{CAM}$. This comparison was performed within channels. To compute the slope, t0 was align to the light stimulus and t1 was defined 60 ms after stimulus. Wilcoxon rank sum test was used to determine statistical significance. Only channels with average slope in CT_{CAM} significantly different from the average slope in $T3_{CAM}$ were included in further analyses. For these channels, we computed the synaptic response by subtracting the average response in the last 2 min of $T3_{CAM}$ to the average response in the last 2 min of CT_{CAM}, and collected the slope and amplitude of the synaptic response. The slope was defined as above and the amplitude was defined as the maximum or minimum (depending on the orientation of the response) between the light stimulus and 160 ms after stimulus. The whole synaptic responses were grouped in CG and RSC ('region'), according to the region where they were recorded. Within each group, the responses were grouped in superficial and deep responses ('layer'), according to the layer where they were recorded. Differences in the amplitude/absolute amplitude and slope/absolute slope of the synaptic responses were tested using N-Way ANOVA {'region', 'layer'}. Bonferroni's correction was applied to the multiple comparisons. Responses from rats injected with CAG virus were analyzed as described above, with modifications. To select channels with significant responses, we compared the average slope of the responses in the last 2 min of CT_{CAG} *versus* the last 2 min of $T2_{CAG}$. For these channels, we computed the excitatory response by subtracting the average response in the last 2 min of $T2_{CAG}$ to the average response in the last 2 min of CT_{CAG}, and we computed the inhibitory response by subtracting the average response in the last 2 min of $T3_{CAG}$ to the average response in

the last 2 min of $T2_{CAG}$. The whole synaptic responses from RSC were grouped in excitatory and inhibitory. Differences in the amplitude/absolute amplitude and slope/absolute slope of the synaptic responses were tested using Wilcoxon signed rank test.

5. *IN VIVO* ELECTROPHYSIOLOGY

5.1. IMPLANT SURGERY

For tetrode recording from the MMC and CA1, animals were implanted with a hyperdrive with 32 independently movable tetrodes constructed from (Liang et al. 2017; Kloosterman et al. 2009; Nguyen et al. 2009). The bundle to target the MMC (19 tetrodes) was linear, and it was implanted at +2.0 mm A/P and at +0.5 mm M/L (coordinates of the first tetrode of the linear bundle). The bundle to target CA1 (7-11 tetrodes) was rectangular, and it was implanted at -3.0 mm A/P and at +2.0 mm M/L (coordinates of the top-left tetrode). For pharmacogenetic experiments, rats were bilaterally injected with AAV_8.CaMKIIa.hM4D(G_i)-mCherry (500 nL per injection) in the diHIPP (coordinates depicted in Table 2).

The implant surgery was performed as described for the injection of anatomical tracers and viral constructs, with some modifications. The hyperdrive was secured to the skull with 7 jeweler's screws in the temporal crest. An additional screw behind the lambda (above the cerebellum) served as ground. The screws and the viral injections were done before the craniotomy. Once finished the craniotomy and durotomy, mineral oil was applied to the surface of the brain, and the hyperdrive was lowered with the tetrodes sticking out (1.5 mm for MMC and 2.0 mm for CA1). The hyperdrive was secured to the screws and bone with dental cement and the surgical wound was closed. During recovery, animals received subcutaneous injections of Carprofen to prevent pain and inflammation, and had *ad libitum* access to nutritional gel and solid food. Rats were allowed to recover during one week post-surgery. This protocol was based on (Remondes & Wilson 2013; Remondes & Wilson 2015).

5.2. DNMP TASK

Rats were handled 1 week before the implant surgery and were fed with dry-food soaked in milk chocolate for habituation. One week post-surgery, rats were habituated to the maze in one session of 30 min. Milk chocolate drops were placed in the reward ports and across the maze. Once experiments began, rats were given 2 sessions per day. Each session consisted of 20 trials, and each trial consisted of two runs, the Sample Run and the Test Run. All trials started in the sleep box. In the Sample Run, rats were placed in the central arm and forced to choose one of the arms (left or right) by closing the other with a block. Rats were rewarded in each Sample Run. When the rats consumed the reward, it was gently picked up and trapped in the start zone for 15 s. During the delay, the arms and the stem were wiped with 70% EtOH. In the Test Run, the block trapping the rats in the start zone was removed and animals were allowed to choose freely which arm to visit (left or right). Rats were rewarded for visiting the arm blocked in the Sample Run and were not rewarded for choosing the previously visited. After the Test Run, rats were placed back to the sleep box for 30 s and a new trial started. The forced choices in the Sample Run were balanced (50% left and 50% right) and pseudo-randomized. Rats were scored based on the number of correct/ incorrect choices in the Test Run, and based on the time they needed to choose. The position of the experimenter in the room was constant across experiments. Reward was administered through a long tube connected to a peristaltic pump installed in the room next to the behavioral room. This protocol was based on (Yamamoto & Tonegawa 2017),with modifications.

5.3. ELECTROPHYSIOLOGICAL RECORDINGS AND PHARMACOGENETICS

Tetrodes were daily adjusted in the first week post-surgery to prevent stucking and to reach the target brain regions. Data included in this work were acquired from awake rats in various behavioral states, namely running the DNMT task (Yamamoto & Tonegawa 2017) and open field exploration sessions with and without reward. Recordings in the

DNMT task were carried out during habituation, learning, in *plateau* performance, and for pharmacogenetic experiments. Tetrodes were daily adjusted after behavioral testing at a maximal rate of 25-50 µm/ day and guaranteeing at least 12 hours between adjustment and recording to ensure single units' stability. During pharmacogenetic experiments, the adjustment routine changed to guarantee that the same single units were tested under CNO (1 mg/kg, intraperitoneal) and vehicle. Single units' action potentials and LFP were recorded using the Intan's RHD2000 System in the Open Ephys configuration (Lopes et al. 2015; Siegle et al. 2017). Extracellular action potentials and continuous LFP were acquired at 30 kHz per channel, digitized and amplified using RHD2164 amplifier boards, and transmitted to the acquisition computer. Xyt position was acquired at 30 fps using a Flea 3 Point Grey camera tracking an LED placed on the hyperdrive. Bonsai Software run in the acquisition computer and was used to manage the acquisition processes and write the electrophysiological and position data files.

5.4. DATA ANALYSIS AND STATISTICS

Raw data were band-pass filtered between 700 Hz and 8 kHz for waveform extraction, and between 0.1 and 8 kHz for LFP analysis. Action potentials were assigned to individual cells by offline clustering based on spike amplitudes, using UltraMegaSort 2000 (Hill et al. 2011). Subsequent analyses employed functions from the Chronux toolbox and code written by M. Remondes in Matlab (Mathworks, Natick, MA), ultimately adapted by E. Ferreira-Fernandes.

Extracted spikes from either clustered single units, or unclustered, were converted into a single file of timestamps and binned at 10 ms to create a MUA spikecounts vector per region and per dataset. LFP was filtered to remove movement artifacts. All data was then analyzed at epochs corresponding to +/- 1 s of enhanced HIPP neural spiking activity, defined as 10 ms bins with over 4 MUA spikes, on each dataset. Binned MUA response, trigger-point response, spectra and coherence with HIPP binned MUA were computed, the latter two for each frequency until a maximum of 50 Hz (given MUA bin size of 10 ms), in 50 ms-stepping windows of 500 ms duration. Such spectrograms and coherograms were normalized by a pre-trigger baseline of 0.5 s and pre vs post HIPP-trigger

magnitudes were compared across relevant frequencies and MMC regions using n-way ANOVA with the appropriate factors. Post-hoc comparisons were made using Bonferroni corrections.

5.5. HISTOLOGY AND MICROSCOPY

The position of the tetrodes along the traces was defined based on post-mortem histological verification after electrolytic lesion, the records of daily adjustments, and direct visual control of the tetrode entry sites during surgery. For the electrolytic lesions, animals were euthanized and 10 μA of cathode current was injected during 10 s per channel. Brains were fixed and processed as previously described for retrograde and anterograde neuronal tracing (see Anatomy, Immunohistochemistry). Tetrode tracks and electrolytic lesions were brightfield imaged in an Axio Observer widefield fluorescence microscope (Zeiss) equipped with an Axiocam 506 mono CCD (Zeiss). AAV_8.CaMKIIa.hM4D(G_i)-mCherry injection and expression were evaluated using a Zeiss AxioZoom V16 fluorescence stereo microscope (Zeiss) equipped with a monochromatic AxioCam MRm camera (Zeiss) and a PlanNeoFluar Z objective (Zeiss). Zeiss filter set RFP (FS63HE) was used to observe mCherry.

V

Results

V. RESULTS

1. CG receives input from SP, whereas RSC receives input from pyramidal and non-pyramidal *strata*

To quantify the hippocampal populations projecting to the MMC, we counted the hippocampal neurons labeled by CTB-Alexa 647, following injection at individual rostro-caudal MMC coordinates (Figure 14 and Table 2). All injections were on target, and no effort was made to target specific subdivisions of the ACC, MCC, or RSC.

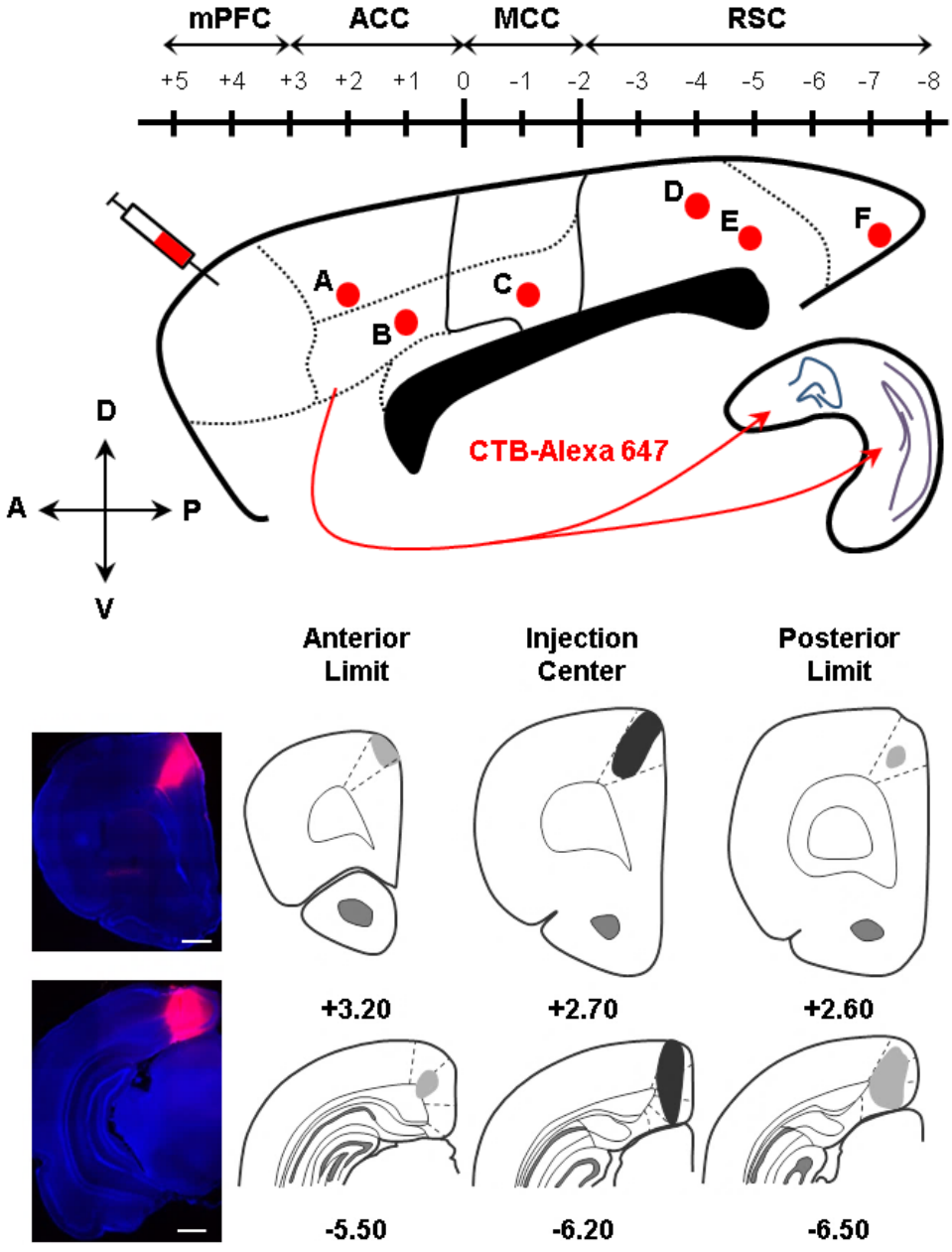

Figure 14 – Retrograde tracer injections. Top, Coordinates. Bottom, Injection sites in 2 example rats (Injections A and E). Values are A/P coordinates in mm from bregma. Magnification: 10x. Scale bar: 1 mm.

Our results show that the full extent of MMC was directly targeted by hippocampal CA1 axons, contrary to earlier reports (Figure 15) (Lee A. Cenquizca & Swanson 2007; Jay & Witter 1991). To test for differences in the distribution of labeled neurons across the HIPP, we counted and compared the numbers of CTB positive neurons in each hippocampal level (dHIPP, diHIPP, and vHIPP, Table 3) and in each hippocampal *strata* (SO, SP, SR, and SR/SLM, Table 4), as a function of each MMC injection level (ACC, MCC, and RSC). We found a significant difference in the hippocampal levels providing input to the different levels of the MMC, and the major hippocampal populations targeting MMC were located in diHIPP (N-way ANOVA, $F_{(2,21)}$=14.87, p=0.0001, followed by Bonferroni-corrected *post hoc* multiple comparisons) (Table 3 and Figure 16, top). Regarding the distribution of CTB positive neurons across the hippocampal *strata*, we found a significant difference in the hippocampal *strata* providing input to the different levels of the MMC (N-way ANOVA, $F_{(3,28)}$=11.94, p=0.000) (Table 4 and Figure 16, bottom). In addition, there was a significant interaction between the MMC injection level and the numbers of neurons counted on each *stratum*, suggesting that the distribution of the hippocampal populations across the hippocampal *strata* depends on the MMC level where the injection was performed (N-way ANOVA, $F_{(6,28)}$=3.62, p=0.0087; significant interaction between 'injection level' and 'hippocampal *strata*'). Specifically, the hippocampal populations targeting the ACC were located almost exclusively in SP (N-way ANOVA, p<0.05 in pairwise comparisons with Bonferroni's correction) (Figure 16, bottom). This result was confirmed by the injection of a non-selective retrograde virus rAAV2-retro-tdTomato (Tervo et al. 2016) in CG, which labeled a dense population of exclusively pyramidal neurons in all medial-lateral divisions of diHIPP (data not shown). No such difference was found after RSC injections, which labeled populations of neurons in pyramidal and non-pyramidal *strata* (N-way ANOVA, all p≈1 in pairwise comparisons with Bonferroni's correction) (Figure 16, bottom). The distribution of labeled neurons in the MCC resembled the distribution seen for RSC injections, with no significant differences in the neuron numbers across *strata* (N-way ANOVA, all p≈1 in pairwise comparisons with Bonferroni's correction). This suggests that, contrary to what is suggested by cytoarchitectonic and immunohistochemistry results (Vogt, 2016), MCC and RSC are indistinct in terms of HIPP connectivity (Figure 16, bottom). The numbers of neurons labeled in SP was, however, not different from the one obtained upon ACC injection

(p=0.12), suggesting that MCC and more anterior MMC levels receive input from comparable numbers of pyramidal neurons.

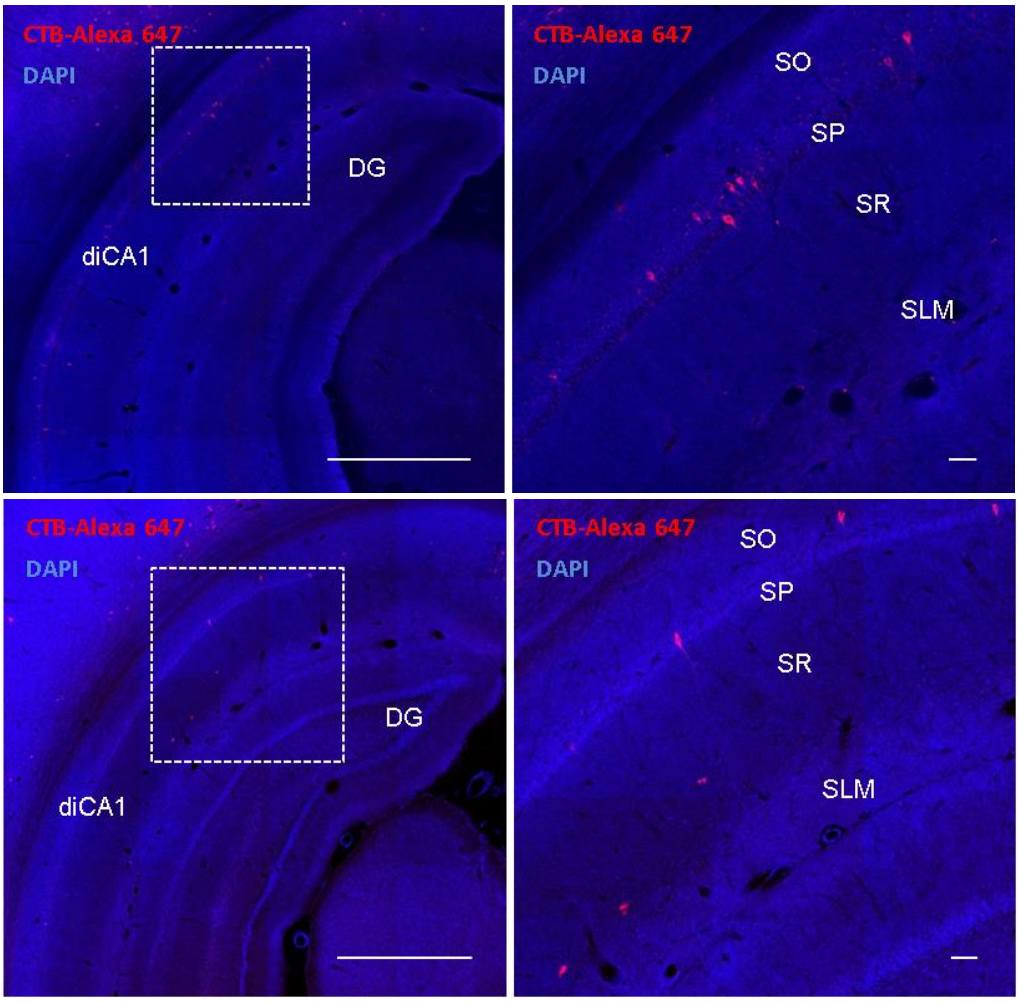

Figure 15 – MMC is directly targeted by hippocampal populations. Top, Fluorescence pictures from Injection A in ACC showing CTB positive hippocampal neurons located in diHIPP (left), with a distribution almost restricted to SP (right). Bottom, Fluorescence pictures from Injection E in RSC showing CTB positive hippocampal neurons located in diHIPP (left), with a distribution spanning the pyramidal and non-pyramidal *strata* (right). Magnification: 10x (left) and 20x (right). Scale bars: 1mm (left) and 50 µm (right).

Together, the data support the existence of hippocampal monosynaptic projections targeting the divisions of the MMC. Crucially, these projections display an anterior-posterior gradient. The ACC is mainly targeted by diHIPP, and such input is provided almost exclusively by cells located in SP. Conversely, the MCC and RSC are mainly targeted by diHIPP, but they balanced input from hippocampal cells located in pyramidal and non-pyramidal *strata*.

Table 3 – Absolute number of CTB positive neurons grouped by 'injection site' and 'hippocampal level' for N-way ANOVA.

	(CTB POSITIVE NEURONS) AVERAGE ± STANDARD DEVIATION		
Injection Sites	dHIPP	diHIPP	vHIPP
ACC	(2, 8, 3, 0)	(155, 63, 175, 288)	(76, 21, 79, 65)
(A, B1, B2, B3; n = 4)	3.25 ± 3.40	170.25 ± 92.42	60.25 ± 26.85
MCC	(47, 1, 3)	(154, 49, 49)	(33, 14, 8)
(C1, C2, C3; n = 3)	17 ± 26	84 ± 60.62	18.33 ± 13.05
RSC	(32, 46, 41)	(139, 227, 59)	(48, 0, 0)
(D, E, F; n = 3)	39.67 ± 7.09	141.67 ± 84.03	16 ± 27.71

Table 4 – Absolute number of CTB positive neurons grouped by 'injection site' and 'hippocampal *strata*' for N-way ANOVA.

	(CTB POSITIVE NEURONS) AVERAGE ± STANDARD DEVIATION			
Injection Sites	SO	SP	SR	SR/SLM
ACC (A, B1, B2, B3; n = 4)	(2, 2, 1, 6)	(227, 65, 252, 317)	(4, 6, 4, 27)	(0, 19, 0, 3)
	2.75 ± 2.22	215.25 ± 107.11	10.25 ± 11.21	5.5 ± 9.11
MCC (C1, C2, C3; n = 3)	(3, 0, 1)	(137, 63, 58)	(25, 1, 1)	(69, 0, 0)
	1.33 ± 1.53	86 ± 44.24	9 ± 13.86	23 ± 39.84
RSC (D, E, F; n = 3)	(5, 21, 1)	(108, 11, 95)	(36, 53, 2)	(70, 188, 2)
	9 ± 10.58	71.33 ± 52.65	30.33 ± 25.97	86.67 ± 94.11

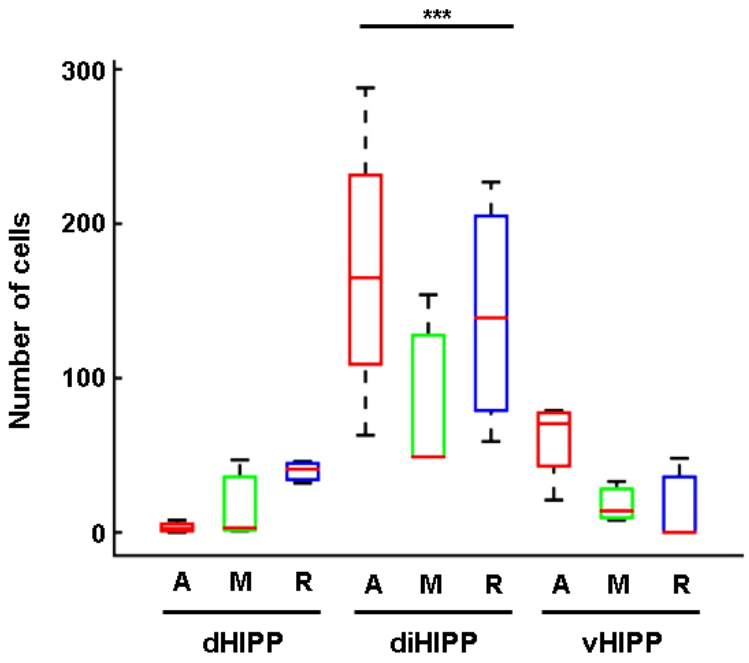

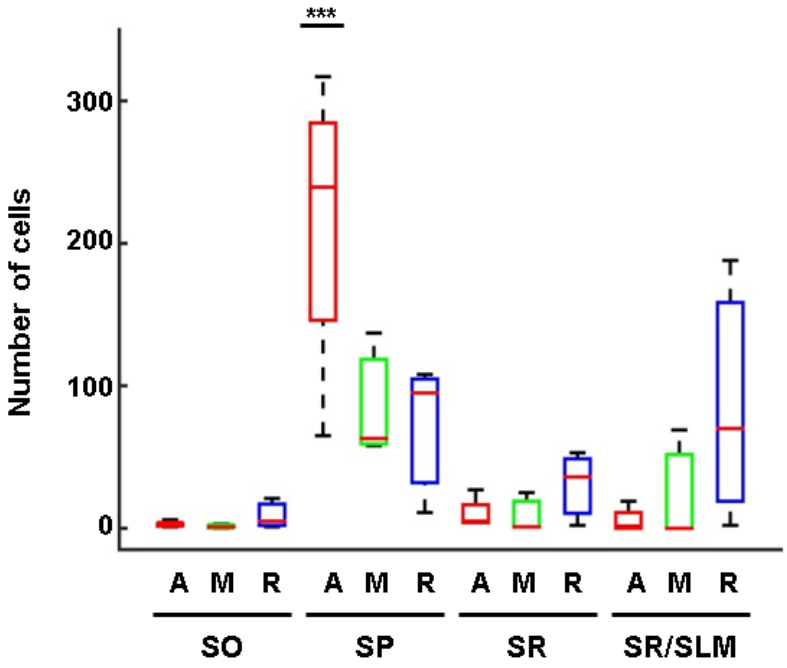

Figure 16 – The hippocampal monosynaptic projections targeting the divisions of the MMC follow an anterior-posterior gradient. Top, Absolute number of CTB positive neurons across the HIPP anterior-posterior level. diHIPP is the major source of input to the MMC (***p<0.01, pairwise comparisons were performed with just one factor, 'hippocampal level', with Bonferroni's correction). Bottom, Absolute number of CTB positive neurons across hippocampal *strata*. (***p<0.01, pairwise comparisons were performed with two factors, 'injection level' and 'hippocampal *strata*', with Bonferroni's correction). SP is the major source of input to ACC and MCC and RSC receive similar input from all hippocampal strata (pairwise comparisons within brain regions). Note that the number of cells in A-SP is not significantly different from M-SP or R-SR/SLM when the pairwise comparisons were performed between regions (not illustrated). A, ACC; M, MCC; R, RSC.

2. The monosynaptic hippocampal input to RSC includes long-range inhibitory projecting interneurons located in the border between SR and SLM

We have shown that RSC is targeted by hippocampal neurons located in pyramidal and non-pyramidal *strata*. Specifically, the non-pyramidal neurons were interneuron-shaped neurons located at the border between SR and SLM (Figure 15), known to harbor relevant populations of interneurons (Jinno et al. 2007; Jinno 2009; Lovett-Barron & Losonczy 2014). To ascertain whether these were indeed GABAergic neurons, we performed GAD staining on the brain slices resulting from ACC, MCC, and RSC retrograde injections (see previous section). GAD positive neurons were found in all hippocampal *strata*,

independently of the MMC level injected with retrograde tracer, confirming the success of the immunohistochemistry protocol applied. Crucially, only samples injected with CTB-Alexa 647 in RSC harbored neurons labeled with both CTB-Alexa 647 and GAD (Figure 17), and exclusively at the border between SR and SLM. This population of long-range inhibitory projecting (LRIP) interneurons was quantified in two slices from each of 3 animals injected in RSC. We identified 50 double-labeled neurons out of 90 retrogradely labeled with CTB-Alexa 647, suggesting that ~50% of all hippocampal neurons projecting to the RSC are LRIP interneurons located at the border between SR and SLM (Miyashita & Rockland 2007). No such population of LRIP interneurons (double-labeled neurons) was identified in brain slices resulting from ACC or MCC retrograde injections.

Extending these observations, CTB positive neurons located in SP were CaMKIIa positive (Supplementary Material, Figure 31), and the population of LRIP interneurons included both Reelin positive (13.8%) and M2 positive (80.5%) neurons (Supplementary Material, Figure 32).

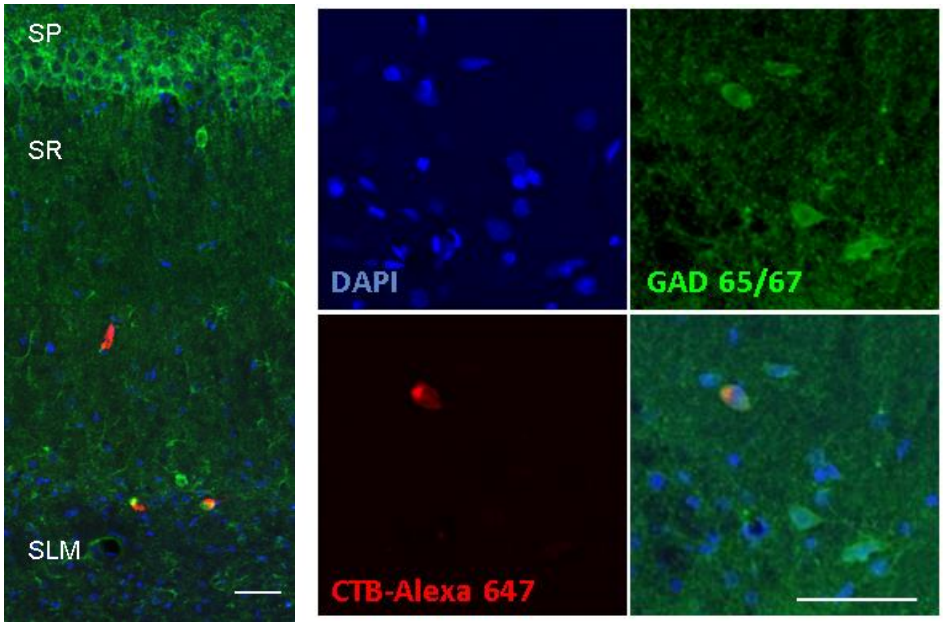

Figure 17 – RSC receives input from LRIP interneurons located at the border between SR and SLM. Left, Confocal picture from Injection E in RSC showing examples of CTB positive, GAD negative neurons in SR and CTB positive, GAD positive neurons at the border between SR and SLM. Magnification: 20x. Scale bar: 50 µm. Right, High magnification confocal picture from Injection E in RSC showing a representative CTB positive, GAD positive LRIP interneuron. Magnification: 63x. Scale bar: 50 µm.

Together, the data suggest that the hippocampal populations targeting the ACC and MCC are exclusively excitatory, whereas the hippocampal projection to the RSC is conveyed by excitatory and inhibitory populations.

3. The hippocampal axons exhibit significant differences in their laminar distribution at distinct MMC levels

Our retrograde labeling studies demonstrated the existence of long-range excitatory hippocampal neurons differentially targeting distinct levels of the MMC. These data are, however, uninformative regarding the distribution of such projections at the destination, which is crucial to understand the effect of such inputs on the neural activity in the MMC. To study the laminar distribution of the hippocampal axons in the MMC, we injected the construct AAV9.CaMKIIa.hChR2.mCherry.WPRE.hGH in diHIPP, leading to expression of mCherry in hippocampal excitatory neurons. The injections were placed in field CA1, with significant viral diffusion to the dorsal subiculum and to the DG.

Following anterograde transport of the fluorescent reporter, we quantified the normalized fluorescence derived from hippocampal axons within a standard ROI at the divisions of the MMC. While we found noticeable fluorescence among layer 1 and layers 2 to 4, a fluorescence peak centered in layer 3 was identified in RSC, and absent in ACC and MCC (Figure 18). At higher magnification, we found that this fluorescence was due to the presence of labeled axons with terminal boutons (LATB), resembling “beads-on-a-string” structures (Lee A. Cenquizca & Swanson 2007). LATB were identified in superficial layers (1 to 4) of RSC (Figure 18). Comparing to RSC, LATB were significantly less abundant on MCC and sparsely present on ACC (Figure 18). In order to quantify this observation, we manually counted the LATB on each layer of each MMC division and compared such number, normalized by layer thickness. LATB counts for ACC, MCC, and RSC revealed a gradient of hippocampal connectivity, with a significant interaction between the MMC ‘region’ and ‘layer’ (N-way ANOVA, $F_{(2,1185)}$=107.58, p=0.0000; significant interaction between ‘region’ and ‘layer’). RSC was unique in the very dense hippocampal projection targeting its superficial layers compared to deep layers (p=0.0000) (Figure 19). Contrarily

to RSC, the density of hippocampal axons in superficial compared to deep layers was not significantly different in ACC or MCC, suggesting a sparse and diffuse projection, lacking layer-specificity. Furthermore, we found a progressive increase in the number of LATB along the anterior-posterior axis of the MMC (N-way ANOVA, $p<0.05$ in pairwise comparisons with Bonferroni's correction) with the exception of the number of LATB in the deep layers of MCC compared to the deep layers of RSC ($p=0.12$) (Figure 19).

These results suggest that, while there is an anterior-posterior gradient in the source of hippocampal input to the MMC, the laminar distribution of hippocampal excitatory axons in the MMC also follows an anterior-posterior gradient, in which a dense, layer-specific projection in RSC is progressively converted in a sparse and diffuse projection in ACC and MCC. The gradient is reinforced by the observation that hippocampal axons in MCC showed a lamination pattern closer to ACC, MCC harbored somewhat higher number of LATB than ACC, and the number of LATB in MCC were intermediate between the ones in ACC and the ones in RSC.

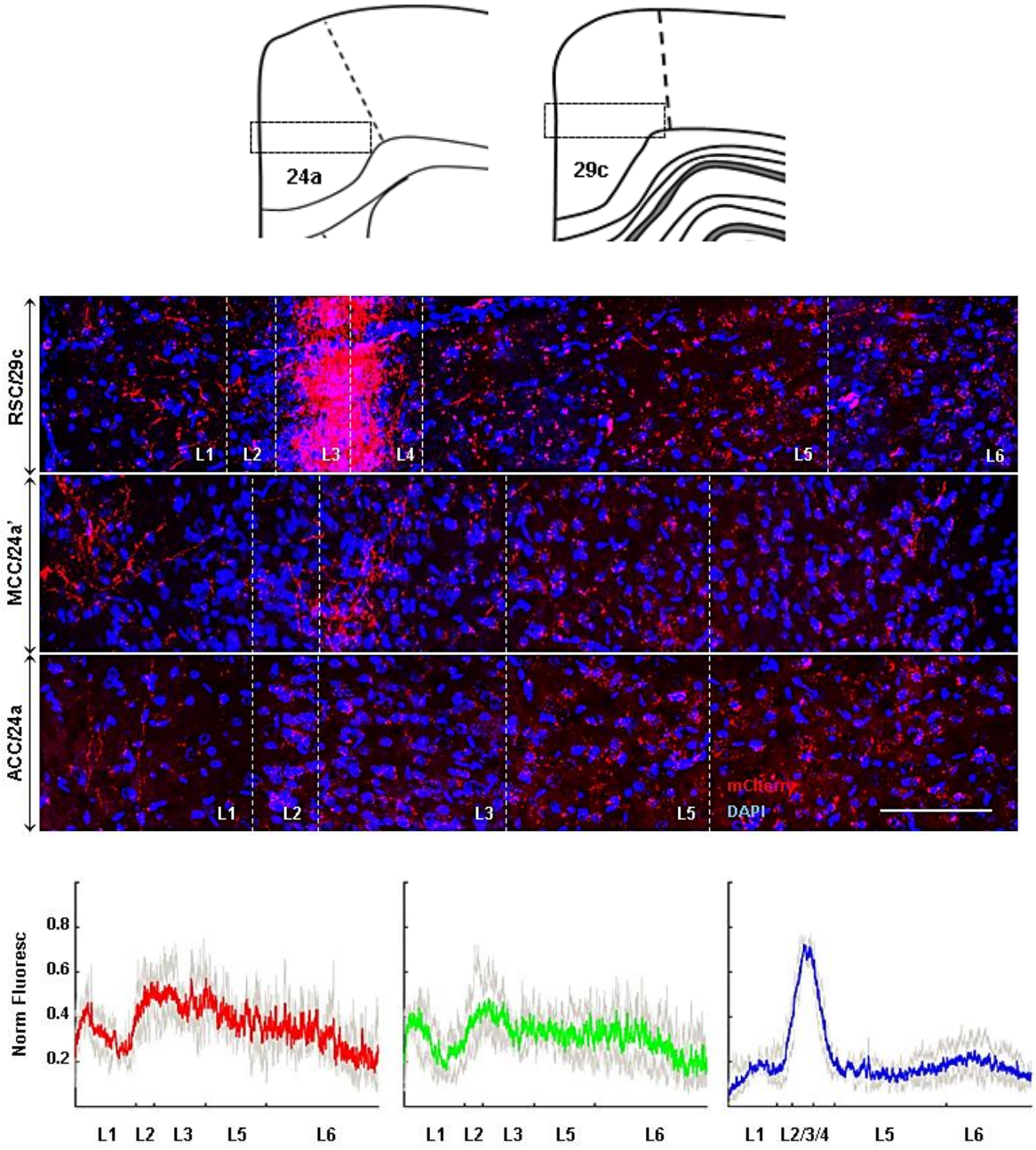

Figure 18 – Laminar distribution of hippocampal excitatory axons in the divisions of the MMC. Top, Standard ROI used to measure the normalized fluorescence at the divisions of the MMC. Middle, Confocal pictures from one example rat expressing mCherry in excitatory neurons of diHIPP. Magnification: 40x. Scale bar: 100 µm. Bottom, Horizontal profile of the normalized mCherry fluorescence in ACC (red), MCC (green), and RSC (blue) (n = 3 rats; red, green, blue, means; light gray, replicas).

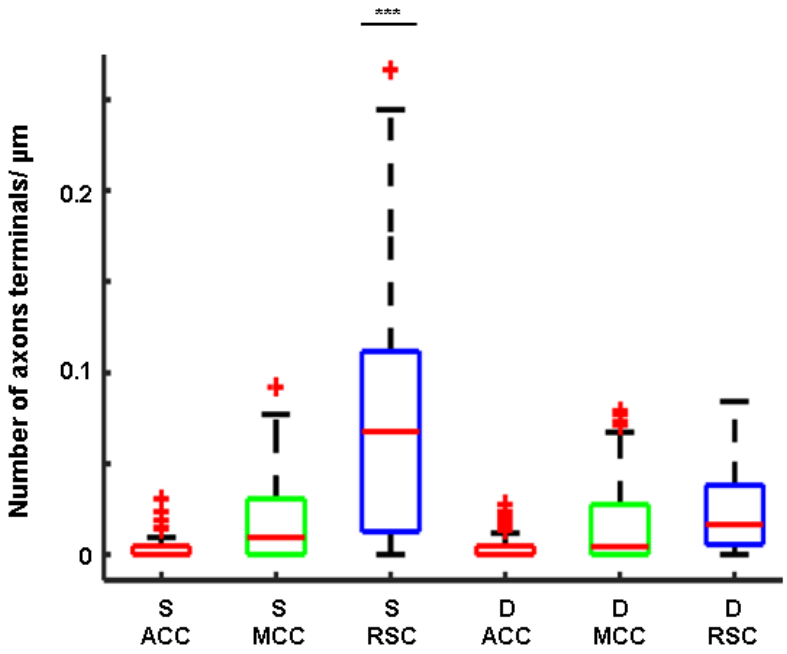

Figure 19 - The laminar distribution of hippocampal excitatory axons follows an anterior-posterior gradient in the MMC. Normalized number of mCherry positive neurons in superficial (S) and deep (D) layers of ACC, MCC, and RSC. (***p<0.01, pairwise comparisons were performed with two factors, 'region' and 'layer', with Bonferroni's correction). Hippocampal axons were denser in the superficial layers of RSC compared to the deep layers. No such difference between superficial and deep layers was observed for ACC or MCC. Note that the density of axons also increases from ACC to RSC when the pairwise comparisons were performed between regions (not illustrated), except in the transition from the deep layers of MCC to the deep layers of RSC.

4. Hippocampal LRIP interneurons at the border between SR and SLM send monosynaptic inhibitory input to superficial layers of RSC

Our previous anterograde study did not target inhibitory populations in HIPP. Since we found hippocampal LRIP targeting RSC, we sought to study the laminar distribution of their axons in RSC as we did for the excitatory populations. Commercial viral constructs with interneuron-specific promoters are, however, not available, and transgenic rats expressing Cre recombinase under the control of interneuron-specific genes were not developed. Assuming that all non-pyramidal neurons establishing long-range connections with RSC were LRIP, we injected a non-selective neurotropic construct, AAV9.CAG. hChR2(H134R).mCherry.WPRE.hGH, in diHIPP, leading to the expression of mCherry in all neural populations. Following anterograde transport of the fluorescent reporter, we studied the laminar distribution of the mCherry-labeled hippocampal axons at the level of

RSC, and compared the result with the one found following CaMKIIa-promoted mCherry expression, to infer the laminar distribution of LATB corresponding to inhibitory terminals.

Expression of a non-selective virus in diHIPP resulted in dense labeling of RSC at the border between layer 3 and layer 4, such as the one obtained upon CaMKIIa-promoted mCherry expression, but also in a distinct, dense labeling on layer 1, creating a second peak not seen when excitatory projections were targeted (Figure 20). To test whether the distinct labeling produced by the non-selective construct had an inhibitory phenotype, thus corresponding to axons of hippocampal LRIP interneurons targeting RSC, we performed GAD staining on the brain slices resulting from RSC anterograde injections with the non-selective construct. GAD positive *puncta* were found to colocalize with mCherry labeled axons among the dense labeling on layer 1 (Figure 21 and Supplementary Material, Figure 33), with an average tM GAD coefficient close to 0.5, suggesting high proportion of co-occurrence between mCherry and GAD signals (Table 5). In agreement with the previous, Costes' threshold was in the [0, 255] range and the correlation below Costes' threshold was around zero (Table 5). This observation confirmed that hippocampal LRIP interneurons project to layer 1 of RSC. When the same analysis was performed in layers 3/4 and 5, the tM GAD coefficient was around 0.1 for layers 3/4 (Table 5) and the Costes' threshold assumed negative values for layer 5, suggesting poor or absent colocalization in this layer and supporting the notion that the additional fluorescence peak we see in Figure 20 can indeed correspond to GABAergic terminals; these are also present in layers 3/4. No significant colocalization was found when the same analyses were performed on brain slices resulting from RSC anterograde injections with the CaMKIIa selective construct (Supplementary Material, Figure 33). An explanation of the metrics used in the colocalization analysis is available in Supplementary Material, Table 6.

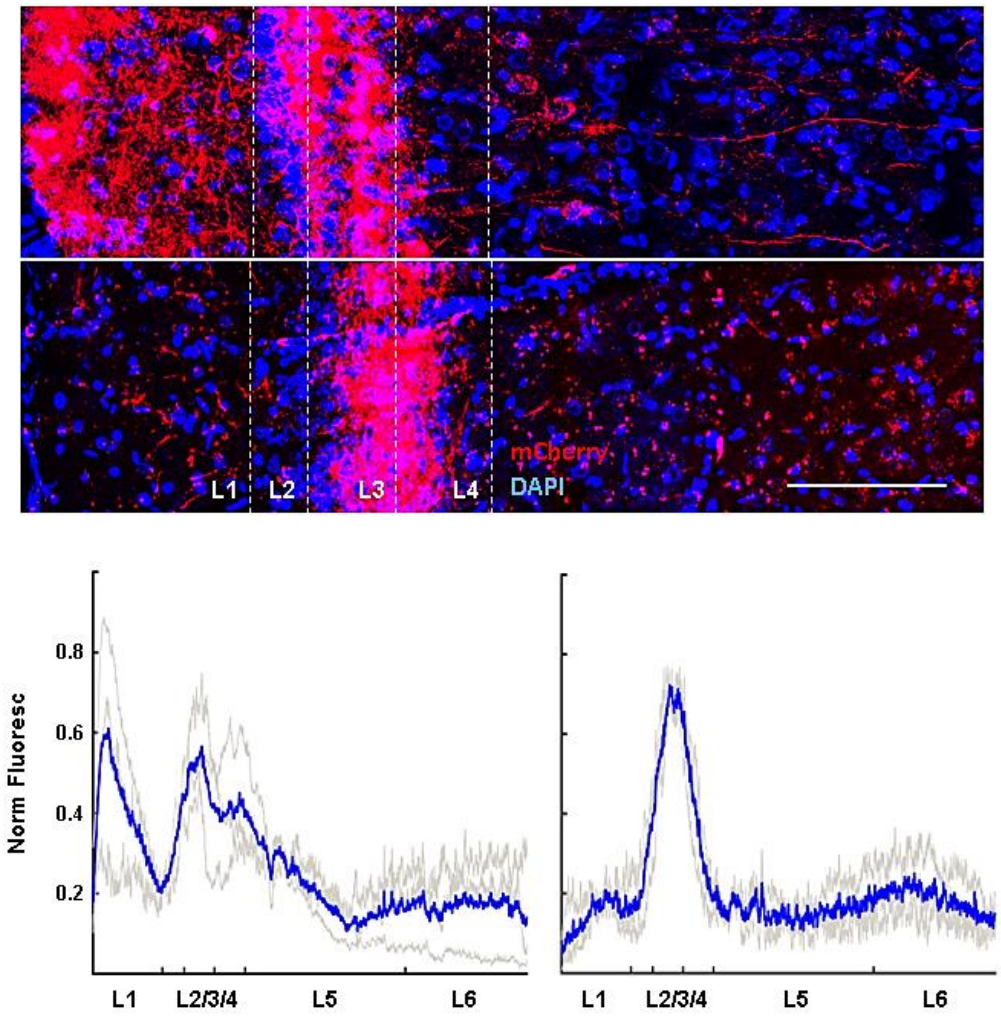

Figure 20 - Laminar distribution of hippocampal axons in RSC. Top, Confocal pictures from one example rat expressing mCherry in diHIPP under a pan-neuronal promoter (top) and under the CaMKIIa promoter (bottom). Magnification: 40x. Scale bar: 100 µm. Bottom, Horizontal profile of the normalized mCherry fluorescence in RSC generated by the CAG construct (left) and the CaMKIIa construct (right) (n = 3 rats; blue, means; light gray, replicas).

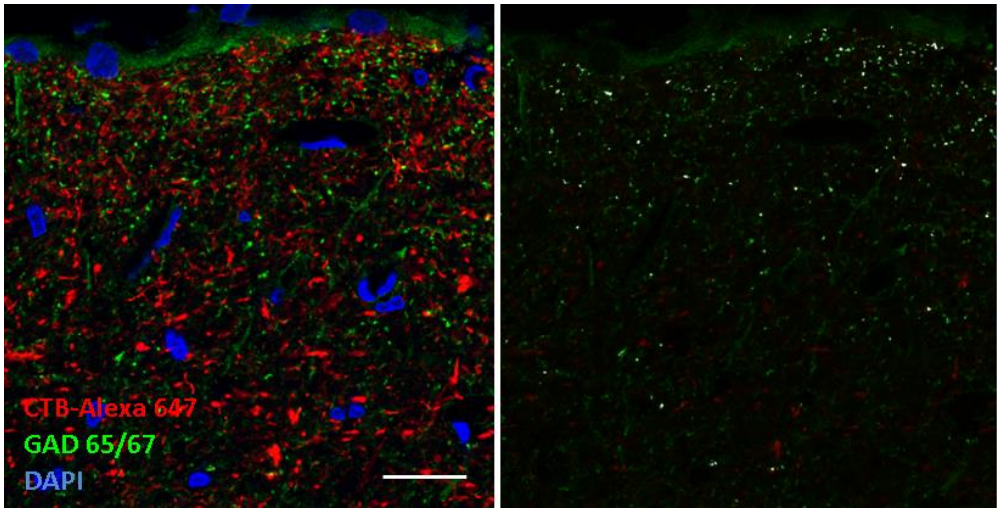

Figure 21 – Hippocampal LRIP interneurons project to layer 1 of RSC. Single plane confocal picture from one example rat showing mCherry positive hippocampal axons and GAD65/67 positive *puncta* in layer 1 of RSC (left). Co-occurring objects are identified as gray dots (right). Scale bar: 20 µm.

Table 5 – Colocalization analysis. tM, thresholded Mander's split colocalization coefficient; th, Costes' threshold; r<th, correlation below the Costes' threshold. All values are average ± standard deviation.

Layers	tM GAD	Th mCherry	th GAD	r<th
1 (n = 3)	0.47 ± 0.17	6.44 ± 2.51	41.11 ± 40.16	0.005 ± 0.016
3/4 (n = 3)	0.10 ± 0.08	92.44 ± 121.93	8.44 ± 2.83	0.001 ± 0.006
5 (n = 3)	≈0	<0	<0	-

5. Monosynaptic hippocampal inputs to the MMC constitute *bona fide* functional synaptic inputs

The presence of LATB originated in the HIPP and targeting the divisions of the MMC suggests, but does not demonstrate, the existence of functional hippocampal synapses onto the neural populations of the MMC, neither does it show how such distinct distribution of hippocampal synaptic inputs contribute to the known differences in neural coding properties between ACC and RSC (Alexander & Nitz 2015; Remondes & Wilson 2013). Local projections to mPFC, ACC and RSC have been studied *in vitro*, in slice electrophysiology experiments using electrical stimulation. These experiments do not guarantee, however, specific stimulation of the hippocampal projections targeting the MMC, and do not provide access to the spatiotemporal dynamics of the evoked responses at the microcircuit level, which requires simultaneous recordings at different positions. In order to specifically study the hippocampal inputs to the different levels of the MMC and ascertain whether they indeed establish functional synapses originating in HIPP, we injected the viral construct AAV9.CaMKIIa.hChR2.mCherry.WPRE.hGH in diHIPP, which drives the expression of hChR2 in excitatory populations. This approach allows specific stimulation of hippocampal excitatory axons in MMC *in vitro* in acute slices using blue light driven by a fiber optic coupled to a recording setup. Using acute cortical slices containing the full extent of MMC placed onto a 64-electrode grid (MEA, Multi Channel Systems), coupled with a blue-LED light delivery system (PlexBright Module, Plexon), we recorded evoked extracellular potentials from the divisions of the MMC, in response to

light stimulation of hChR2-expressing hippocampal excitatory axons (see Supplementary Material, Figure 34 for *in vitro* electrophysiology control experiments and I/O analysis).

We found that stimulation of hippocampal axons using 100 ms pulses of a blue LED (at 30mW total LED power) evoked significant responses on slices originating from all the divisions of the MMC (Figure 21), both in superficial and deep layers. Such responses comprised distinct components, namely the potential resulting from direct activation of hChR2 channels while the LED is on, which could be isolated from the genuine synaptic responses using sequential pharmacological incubations (Figure 21, CT, Control; T_1-T_3, sequential treatments). By sequential application of Picrotoxin, CNQX, and APV, we managed to isolate the "hChR2-only" response (Figure 21, blue trace), which we could subtract from the previous control trace to obtain the synaptic response (Figure 21) and study its properties (slope and amplitude), across the layers of distinct MMC levels. We found no significant differences in the slope and amplitude of the synaptic responses recorded in ACC vs. RSC, nor in synaptic responses recorded in superficial vs. deep layers. We found, however, a significant interaction between 'region' and 'layer' (N-way ANOVA, $F_{(1,38)}$=10.31, p=0.0027 and $F_{(1,38)}$=11.55, p=0.0016; significant interaction between 'region' and 'layer' for slope and amplitude, respectively), suggesting that slope and amplitude of the evoked responses depends on whether the response was recorded at superficial or deep layers, and this dependence significantly changes with the MMC division considered. Specifically, responses evoked in RSC exhibited significantly higher slope and amplitude at superficial layers, whereas evoked responses in ACC exhibited maximal deflections in the deep layers (Figure 22). As expected, these responses would revert later (Figure 21, 200 ms after triggering the LED). When the analysis was restricted to the absolute values for slope and amplitude, the differences previously observed were largely abolished (Figure 22), suggesting that the polarity of the evoked responses is the result of differences in the pattern of activity between MMC levels, matching the differences observed in our anterograde studies. In fact, the patterns of evoked responses matched the laminar distribution of LATB seen in Figures 18 and 19. RSC showed stronger responses in superficial layers, which were densely targeted by hippocampal LATB, whereas rostral levels of MMC, where layer-specificity was absent, showed stronger responses in deeper layers, which contain more sparsely targeted dendrites (Figure 22).

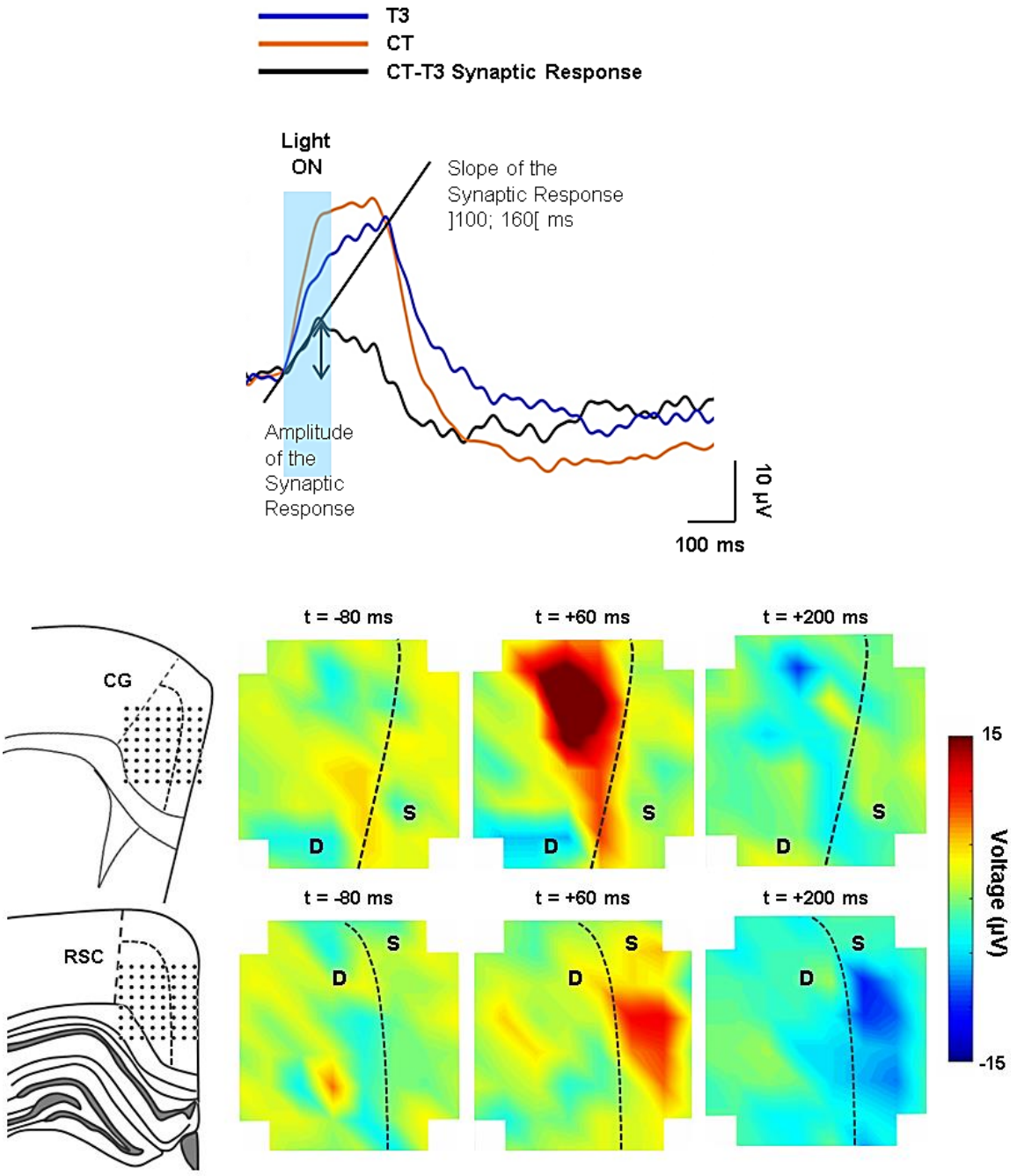

Figure 22 – Monosynaptic hippocampal inputs to the MMC constitute functional synapses. Top, Calculation of the synaptic response by linear subtraction (CT – T3). The trace corresponds to the activity averaged over 2 min in one contact of the MEA array during an experiment with an acute CG slice, under control conditions (CT) and under $T3_{CAM}$ treatment (T3). Computation of slope and amplitude are demonstrated. Bottom, Heatmaps of the excitatory synaptic response in deep (D) and superficial (S) layers of CG (top) and RSC (bottom) (LED triggered at t = 0 ms) Each heatmap illustrates one representative experiment. See Supplementary Material, Figure 35 for current source density analysis.

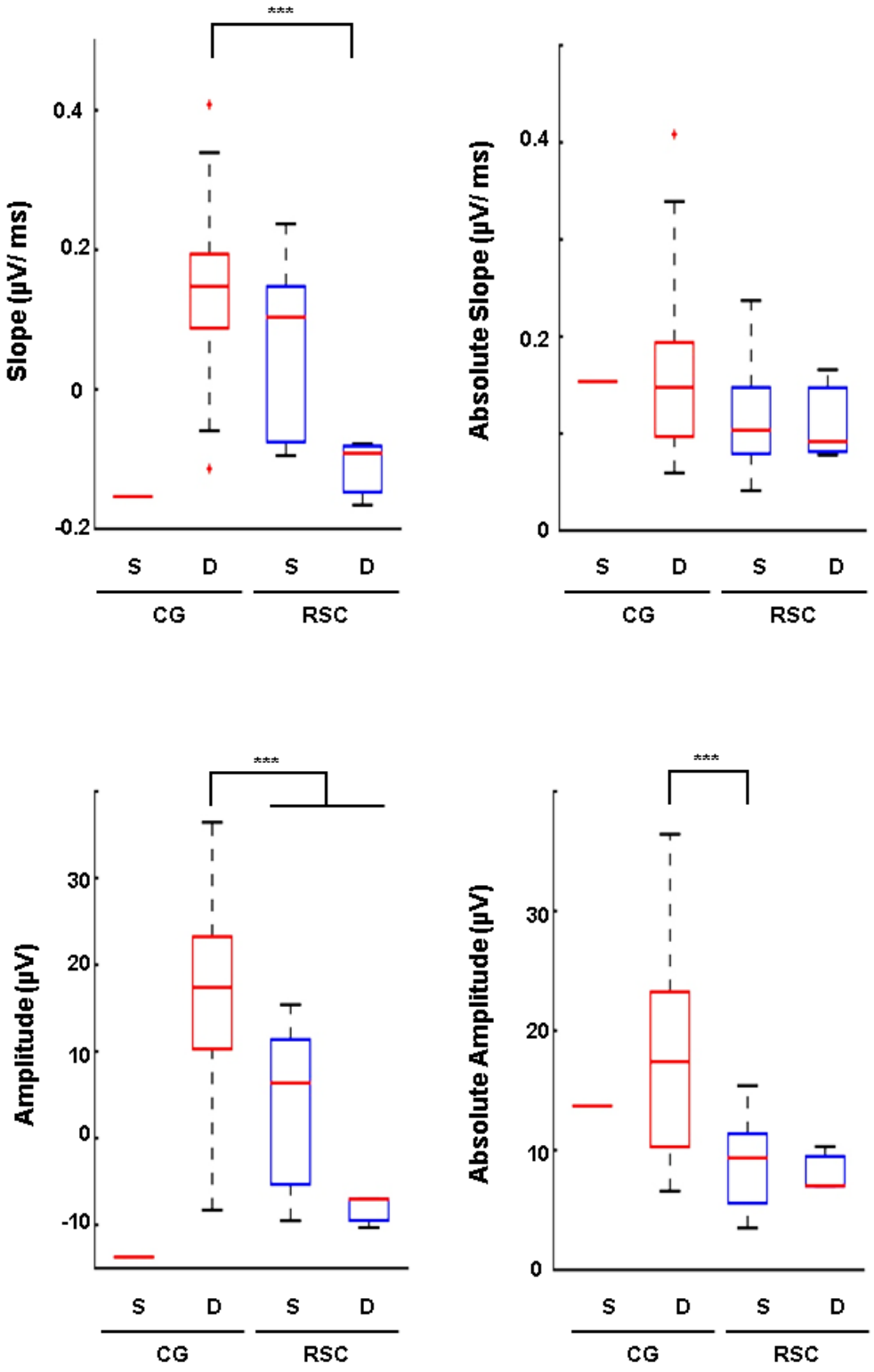

Figure 23 – The patterns of evoked activity match the differences in the laminar distribution of hippocampal LATB in the MMC. Slope and absolute slope (top), amplitude and absolute amplitude (bottom) of the synaptic responses evoked in superficial (S) and deep (D) layers of CG and RSC (***p<0.01 in pairwise comparisons with Bonferroni's correction).

6. Hippocampal LRIP interneurons provide a functional GABAergic input to RSC

Having identified hippocampal LRIP interneurons targeting the RSC, we sought to ascertain whether this neural population would form functional synapses onto RSC. Crucially, we sought to study the effect of the LRIP interneurons in the local circuitry in a manner that was dissociated from the local inhibition provided by local inhibitory interneurons in RSC. To manipulate such inhibitory hippocampal input, we injected a non-selective neurotropic construct, AAV9.CAG.hChR2(H134R).mCherry.WPRE.hGH, in diHIPP, leading to the expression of hChR2 in all neural populations. hChR2-containing hippocampal axons were then stimulated in vitro using a blue LED, and evoked activity was recorded through the MEA System. To isolate the inhibitory component of the hippocampal projection, we inverted the sequence of pharmacological agents used in the previous section. In this rationale, we would initially stimulate the hippocampal LATB targeting RSC with blue light, apply CNQX and APV to block all long and short-range excitatory inputs, thus blocking local interneurons targeted by the hChR2-containing hippocampal excitatory projections, leaving only the long ranging inhibitory terminals whose synapses onto local neurons we would then monitor. Since this approach blocks excitation and then inhibition, we could record excitation and inhibition separately and use such data to essentially confirm the previous results obtained with the CaMKIIa-driven hChR2, besides studying the long-range inhibition in isolation.

The spatial distribution of the light-evoked, excitatory responses in RSC is depicted in the top panel of Figure 23. Subtraction of the hChR2 and inhibitory components from the control trace (see Materials and Methods) showed light-evoked, excitatory responses essentially concentrated in the superficial layers, in agreement with our previous result. The light-evoked, long-range inhibitory responses were further isolated pharmacologically and mathematically (see Materials and Methods), producing the results depicted in the lower panel of Figure 23. In summary, we found that the responses triggered by the hippocampal LRIP interneurons could indeed be isolated and studied; its slope and amplitude are both significantly lower than those corresponding to excitatory responses (Wilcoxon signed rank test, all comparisons, $p=0.0000$), as widely reported, and they tend to target superficial layers of the RSC (Figure 24).

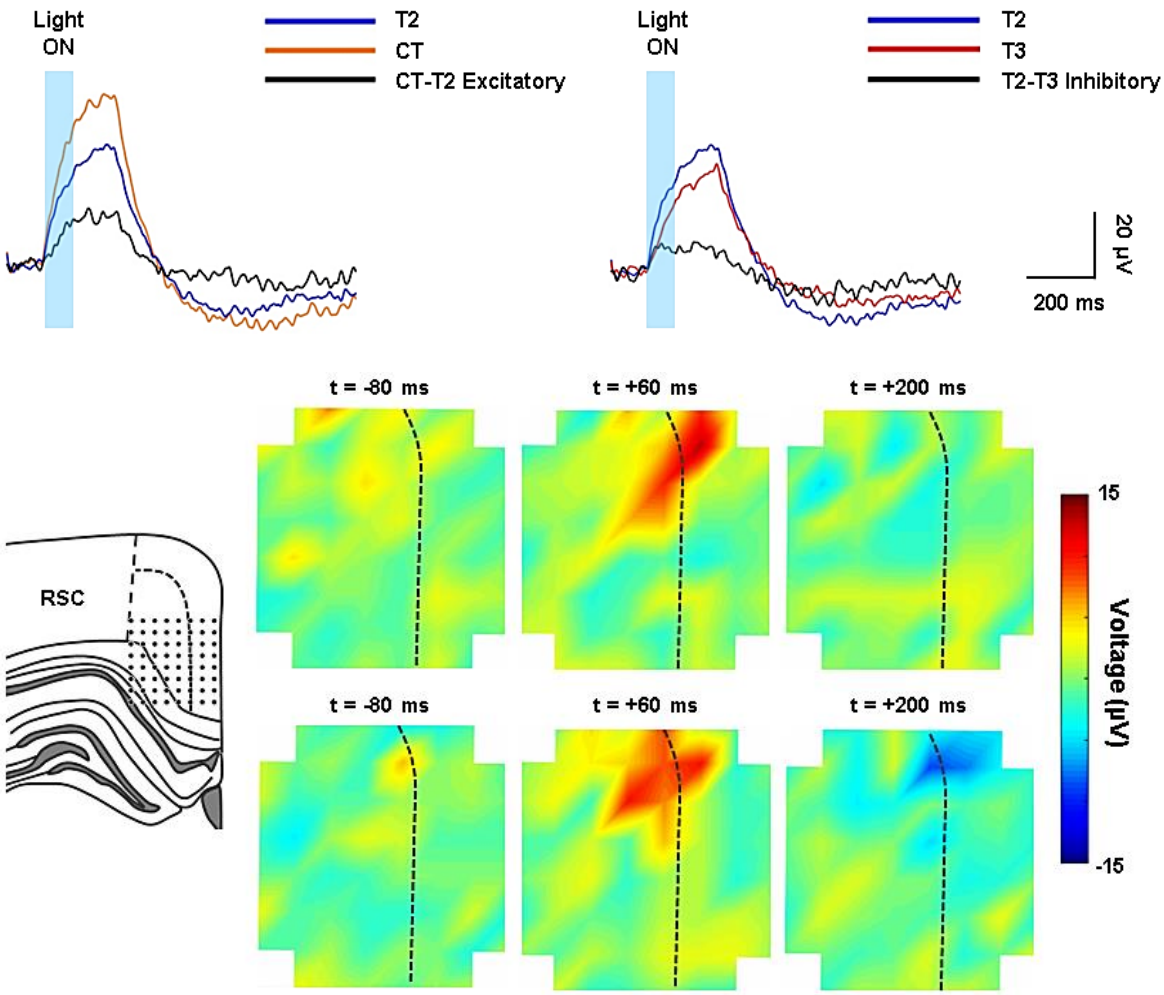

Figure 24 – Hippocampal LRIP interneurons convey a functional GABAergic input to RSC. Top, Calculation of the excitatory and inhibitory responses by linear subtraction (CT – T2 and T2 – T3). The traces correspond to the activity averaged over 2 min in one contact of the MEA array during an experiment with an acute RSC slice, under control conditions (CT), $T2_{CAG}$ (T2), and $T3_{CAG}$ treatment (T3). Bottom, Heatmap of the excitatory (top) and inhibitory (bottom) synaptic response in deep (D) and superficial (S) layers of RSC (LED triggered at t = 0 ms). The heatmaps illustrate one representative experiment. The inhibitory response was detected in the superficial layers and in the transition between superficial and deep layers (layer 4 and upper layer 5). See Supplementary Material, Figure 36 for current source density analysis.

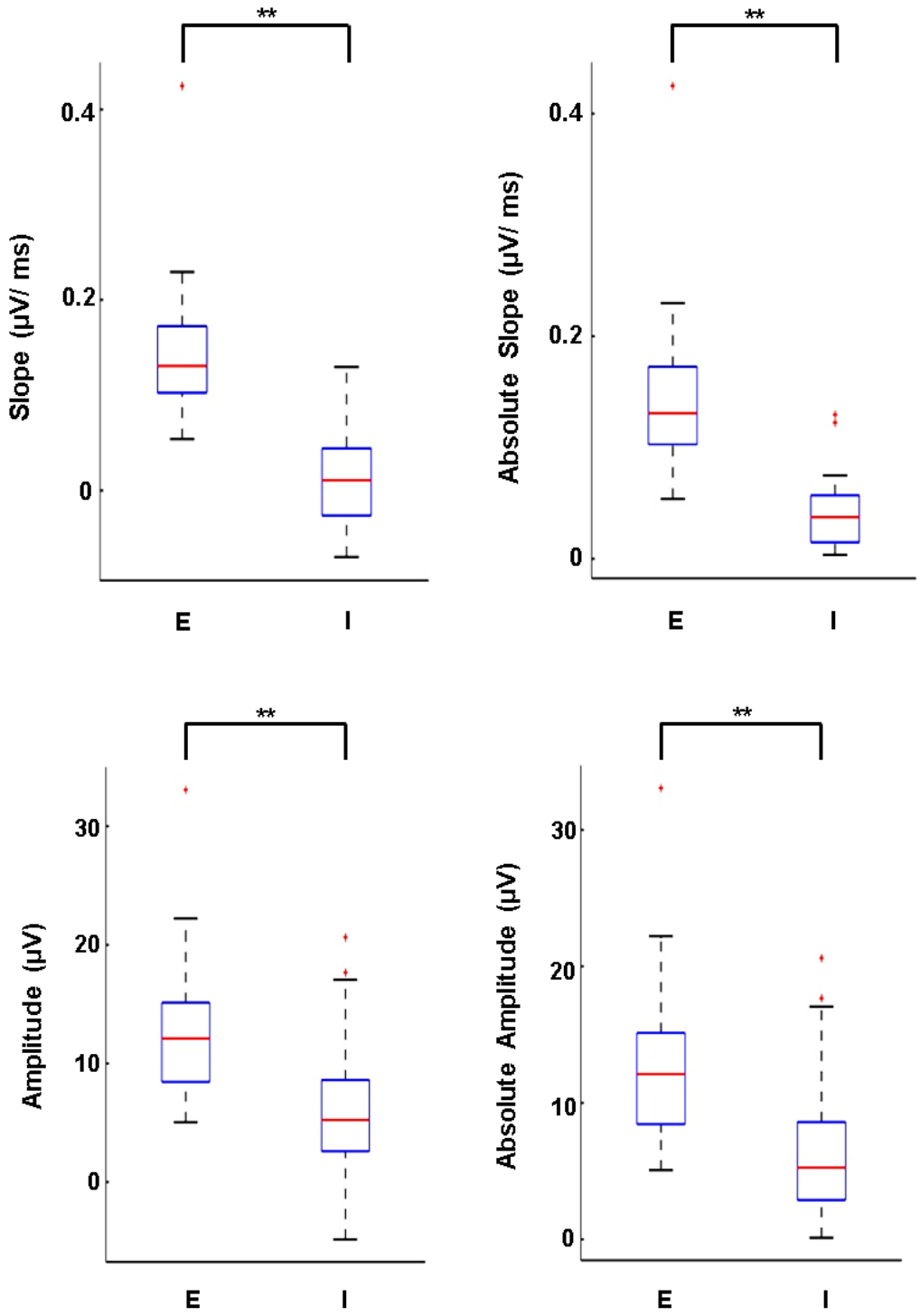

Figure 25 – The patterns of excitatory and inhibitory activity match the laminar distribution of hippocampal LRIP interneurons in the MMC. Slope and absolute slope (top), amplitude and absolute amplitude (bottom) of the excitatory (E) and inhibitory (I) responses evoked in RSC (**p<0.01 in Wilcoxon signed rank test).

7. *In vivo* hippocampal-triggered MMC neural activity is consistent with the presence of diverse monosynaptic connectivity between HIPP and distinct levels of MMC

Having found that the HIPP directly connects to the distinct levels of MMC, establishing *bona fide* synapses therein, and that these connections support diverse remote-to-local neural circuitry, we sought to study the pattern of HIPP-MMC spontaneous co-activity that might result from such diversity. We thus recorded MUA from the diHIPP, simultaneously with the full extent of MMC, encompassing CG, MCC, and RSC, on awake rats in various behavioral conditions, and compared cortical responses to hippocampal spikes. To compute such responses, we extracted 2 second epochs of z-scored cortical MUA triggered by 10 ms time bins containing at least 4 HIPP MUA spikes. As a control, we compared these epochs with equivalent ones triggered by randomly sampled time bins. We found that cortical responses to hippocampal spiking are significantly higher than randomly picked epochs, on all 3 MMC regions (Figure 26, from 12 datasets, $t_{(20,16,22)}$=3.04, 3.41, 2.77, p=0.006, 0.004, 0.01, for CG, MCC and RSC respectively), with no significant differences between distinct regions. A significant increase in cortical activity within 10 ms of hippocampal spiking is consistent with a long-range monosynaptic connection. We have also run these analyses on data from individual cortico-hippocampal tetrode pairs across sessions and confirmed the presence of diverse cortical response patterns to hippocampal spiking (Figure 27), both of cortical MUA and of LFP.

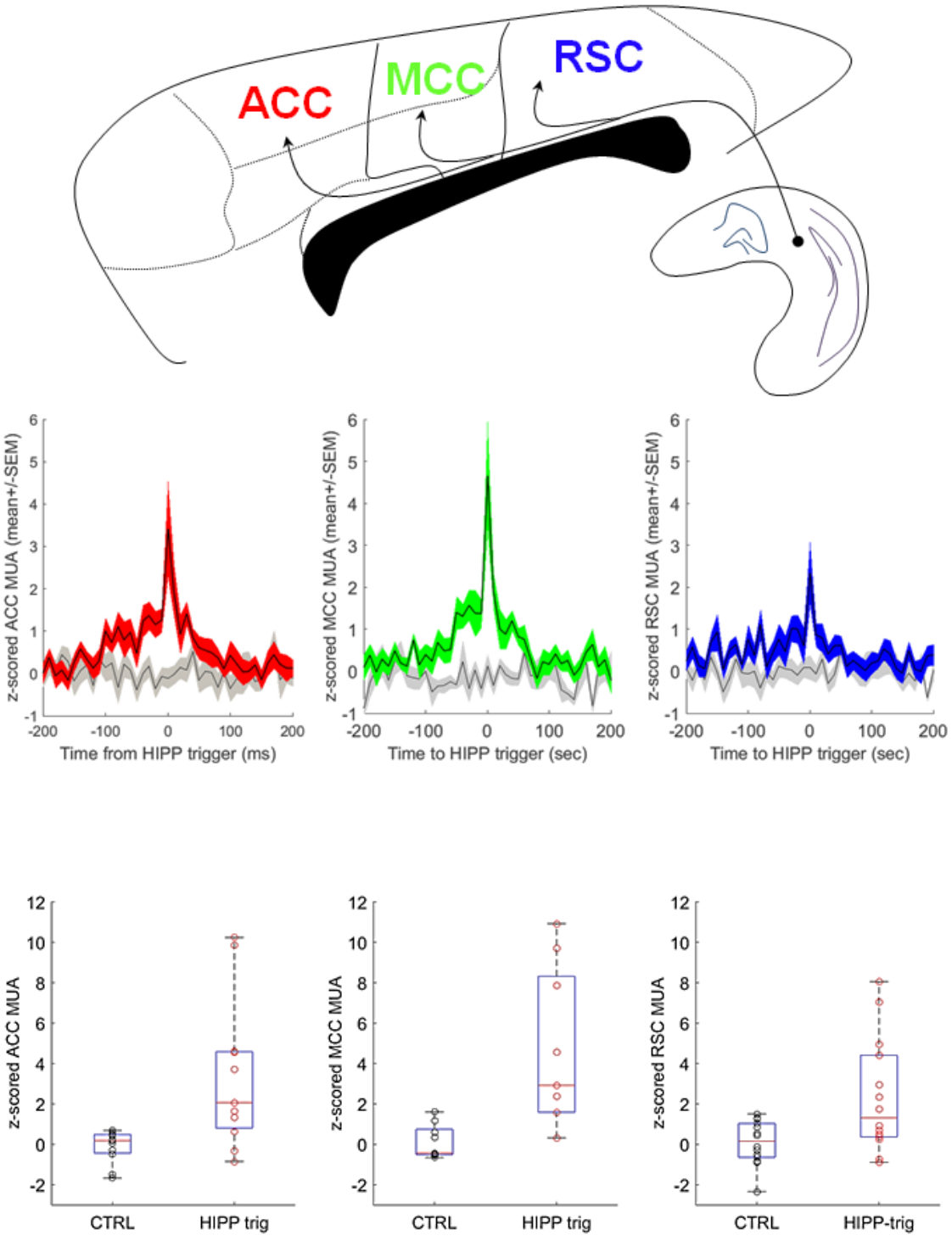

Figure 26 – Hippocampal-triggered cortical activity *in vivo* is consistent with the presence of monosynaptic connectivity between CA1 and MMC regions. Top, Color-coded plots depict CA1-triggered MMC MUA (average +/- SEM, overlaid onto grey-colored plots depicting cortical MUA triggered by randomly chosen time bins. Note the presence of increased activity on all MMC regions, within 20-30 ms of the trigger point, somewhat lower in RSC. Bottom, The row of boxplots depicts cortical MUA across datasets (median +/- IQR), and the randomly-triggered for comparison. All regions exhibited statistically significant MUA increases ($p \leq 0.01$).

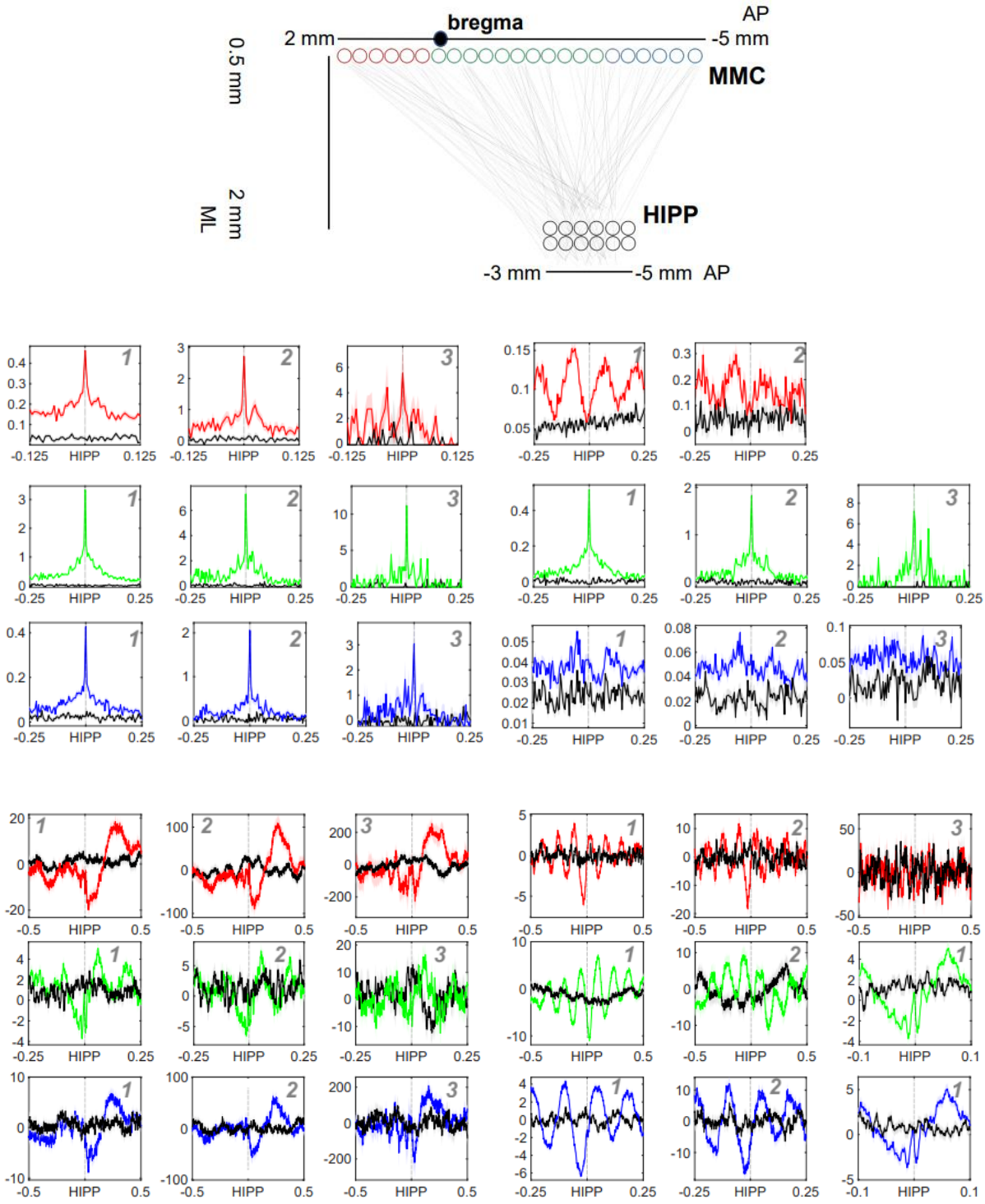

Figure 27 - Hippocampal-triggered changes in MMC MUA and LFP *in vivo*. Representative MUA and raw LFP taken from HIPP-MMC tetrode pairs corresponding to the diagram (top panel), from the three MMC regions at the same time epochs triggered by hippocampal spike events defined for Figure 26, color coded as before. Middle, Note the presence of robust HIPP-spike triggered MUA increases in tetrodes from all MMC regions, incremental with the number of hippocampal spikes considered as threshold. Bottom, Note the deflections of the MMC LFP, ranging from simple short-latency transients, to events with clear rhythmicity in the theta and co-existing gamma ranges. (yy scales: 5 ms binned z-scored MUA or LFP in mV; xx scales: seconds; "HIPP" is the trigger point; insets are the number of hippocampal spikes considered for threshold; in all panels the overlaid gray-colored plot corresponds to randomly triggered neural activity; line and shaded areas are mean ± standard error of the mean).

The diverse connectivity reported above, and the very conspicuous MMC responses to hippocampal spikes prompted us to ask whether such diversity could signify distinct patterns of transient and oscillatory activity and neural coordination. To answer this question, we performed a spectral analysis of the HIPP triggered MUA binned at 10 ms like before, on a 500 ms sliding window stepped every 50 ms. A qualitative assessment of the 3 regions' spectrograms, depicted in Figure 28, shows the presence of power increases on the main biologically-relevant frequencies reported in hippocampal-cortical ensembles, namely theta (5-8 Hz), beta (13-18 Hz), slow-gamma (23-31 Hz) and fast-gamma (40-50 Hz), something absent from the control data triggered randomly (Figure 28, bottom, only shown for hippocampal MUA). Furthermore, there is an apparent increase in relative power at higher frequencies as we move caudally in the cortex (Figure 28, top, note distinct color scales). This gradual increase is accompanied by distinct patterns of oscillatory synchrony, as measured by the spike-triggered HIPP-MMC coherence of the binned MUA (Figure 28, middle, note distinct color scales).

To quantify and test this hypothesis, we normalized power and coherence to a pre-trigger baseline of 0.5 s, took the mean at each of the above frequency bands on each dataset, (Figure 29 and 30), and compared their magnitude in the last data window before the trigger vs the first window completely after the trigger, on the three MMC regions considered, using N-way ANOVA (Figure 29). This analysis revealed a HIPP-triggered power increase in all regions of the MMC on all frequencies (Figure 30, $F_{(1,224)}$=78.06, p=0.0000, n=11 datasets, boxplots are presented for each condition for informative purposes). We then sought to investigate whether there were regional differences in the relative magnitude of coherence across the frequencies analyzed. For this, we used the same normalization procedure as above, and compared magnitudes at the same time points and frequencies as above (Figure 29). We found a main effect of the HIPP trigger (Figure 29, lower panel, $F_{(2,224)}$=26.37, p=0.0000, n=11 datasets, boxplots are presented for each condition for informative purposes) confirming the presence of a HIPP-triggered increase in HIPP-MMC synchrony. In addition, we found a significant trigger vs region interaction ($F_{(2,224)}$=3.92, p=0.021), indicating that such synchrony depends of the cortical region analyzed. Post-hoc comparisons revealed a rostro-caudal increase in the mean hippocampal-cortical coherence, culminating with a significant increase in coherence

between HIPP and RSC (p=0.0000, Bonferroni), itself significantly higher than the coherence between the HIPP and CG (p=0.02, Bonferroni).

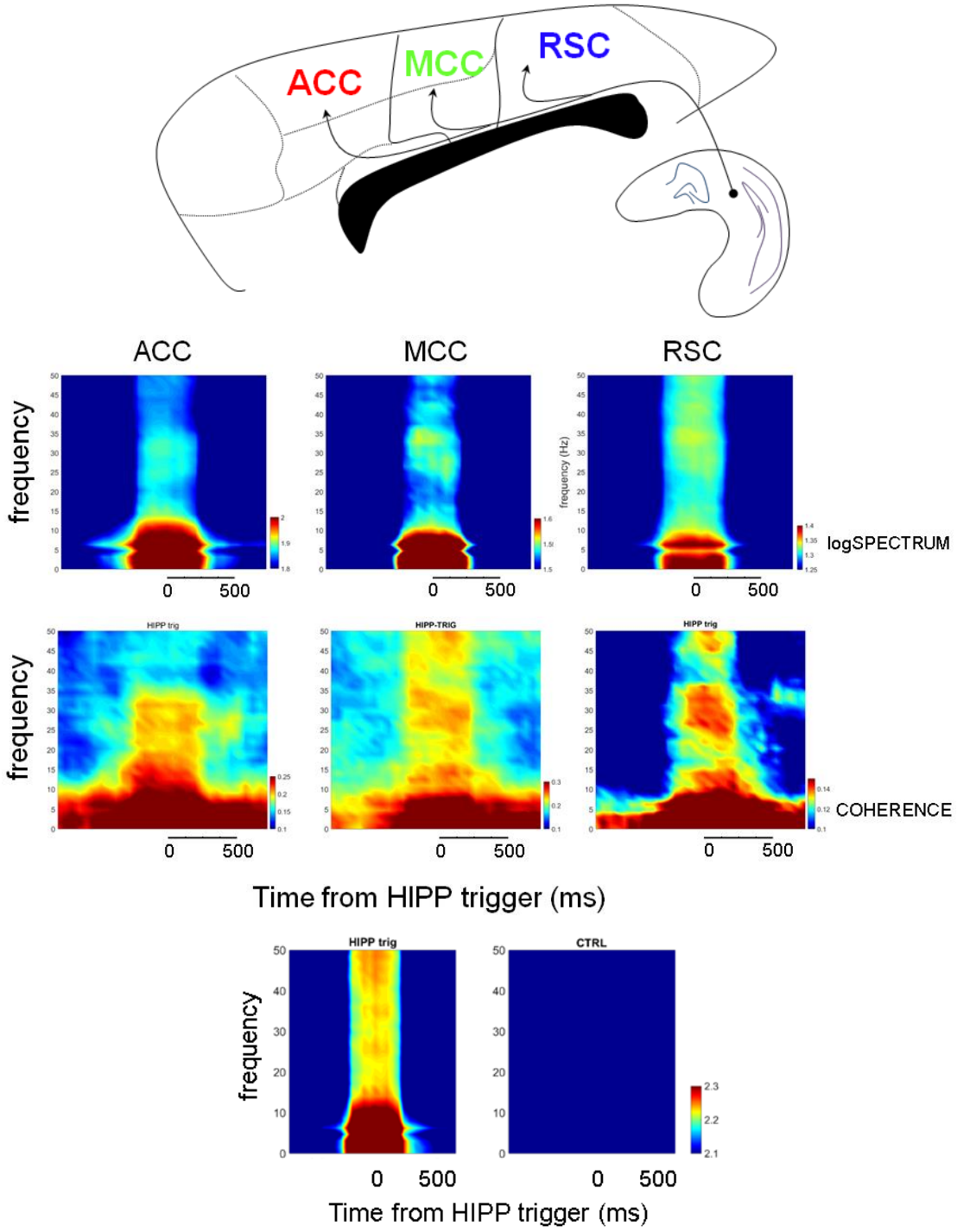

Figure 28 – Hippocampal-cortical spectrograms and coherograms support the presence of short-latency oscillatory synchrony. Top, HIPP-triggered MMC MUA spectrograms. Note the presence of increased power at behavior-relevant frequencies in all regions. Middle, HIPP-triggered MMC MUA coherograms illustrate the temporal alignment of CA1 and MMC MUA. Note the presence of coherence in all MMC regions. Bottom, Spectrogram of the HIPP-triggered MUA. Note the presence of increased power at all relevant frequencies, and the absence thereof in the control data.

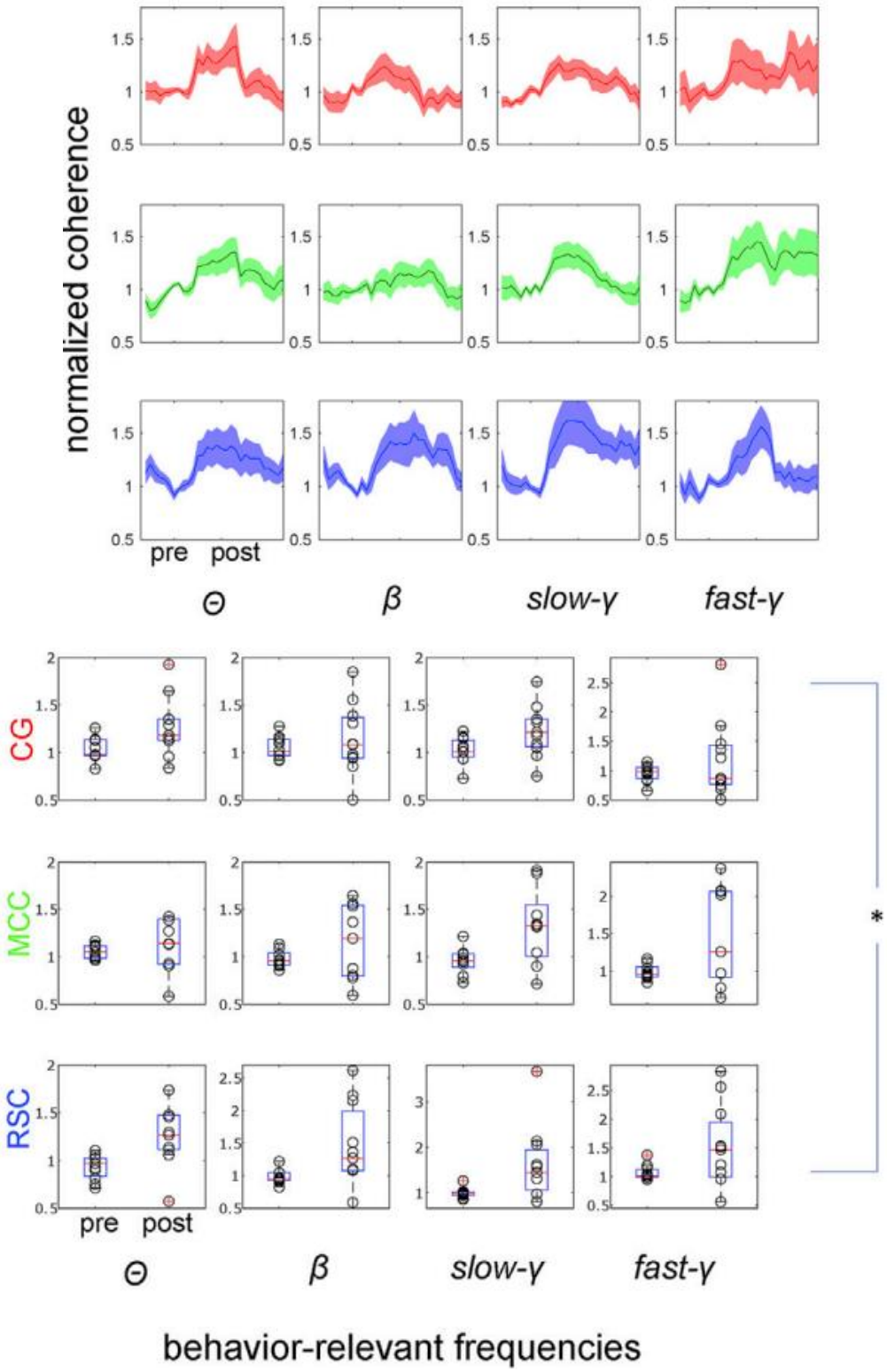

Figure 29 – HIPP-triggered HIPP-MMC coherence increases specifically in the RSC. Upper panel, Color coded plots depict the quantification of HIPP-triggered HIPP-MMC coherence at relevant frequency bands, normalized to a pre-trigger baseline of 0.5 seconds. Lower panel, HIPP-triggered HIPP-MMC coherence significantly increases across MMC (p=0.0000, n=11 datasets, boxplots for each condition are presented for informative purposes), with a significant trigger vs region interaction, and a region-related gradual increase in the mean coherence, culminating with a significant HIPP-triggered increase in coherence between HIPP and RSC (post-hoc comparisons, p=0.0000, Bonferroni), itself significantly different from the post-trigger coherence between HIPP and CG (p=0.02). This anatomically-distributed coherence pattern is suggestive of a rostro-caudal gradient underlying the communication between the HIPP and the distinct divisions of MMC.

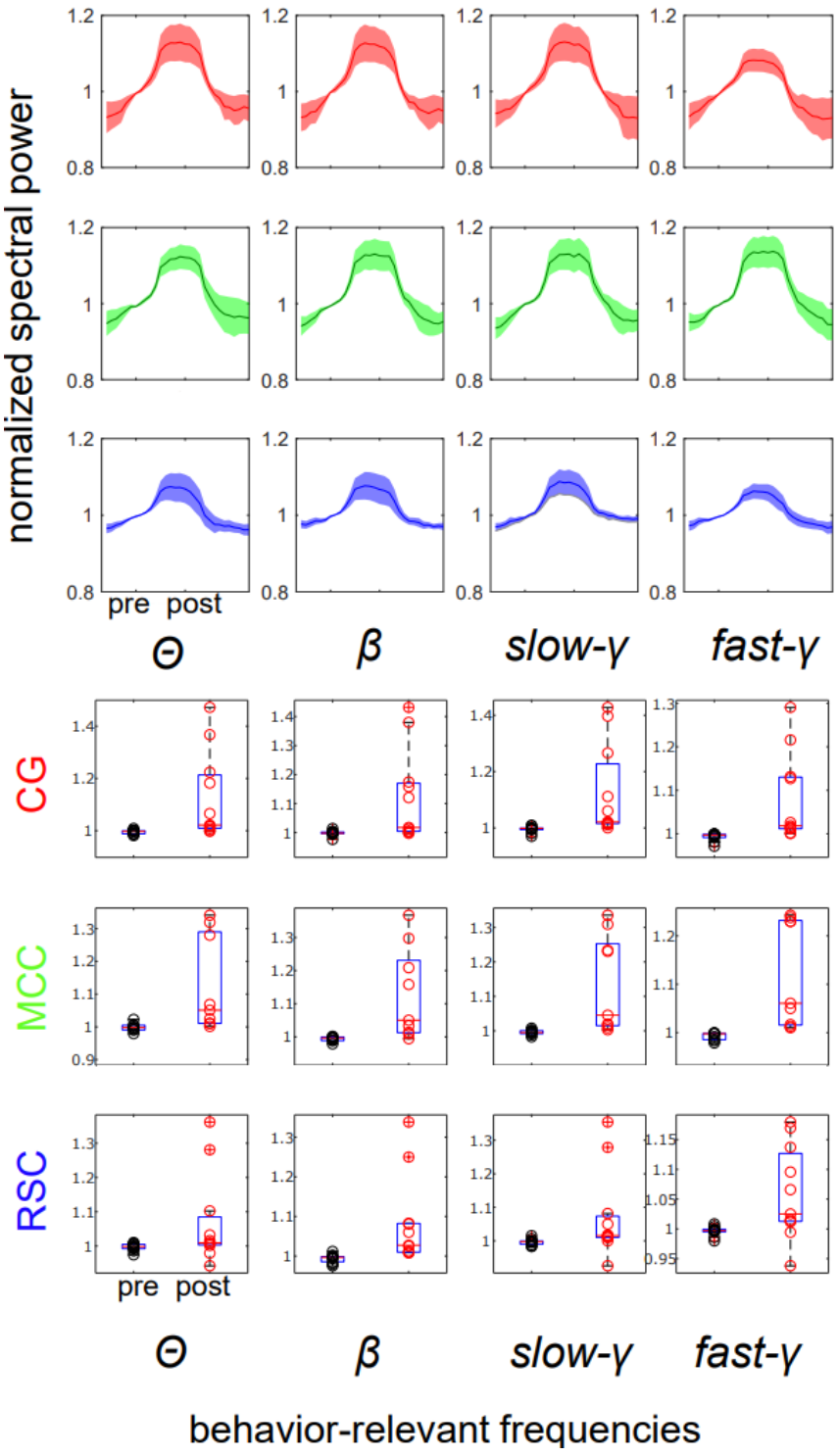

Figure 30 – Medial mesocortical responses to hippocampal spikes at behavior-relevant frequencies. Upper panel, color coded plots depict the quantification of HIPP-triggered MMC power at relevant frequency bands, normalized to a pre-trigger baseline of 0.5 seconds. Lower panel, There is a significant HIPP-triggered power increase at all frequencies regardless of cortical region analyzed (N-way ANOVA with factors pre- vs post-trigger, cortical region, and frequency, $F_{(1,224)}$=78.06, n=11 datasets, boxplots for each condition are presented for informative purposes).

VI

Discussion

VI. DISCUSSION

1. The HIPP-MMC monosynaptic projections follow a topographical gradient

Brent Vogt and colleagues were the first to hypothesize a functional dichotomy in the MMC, considering an anterior executive region and a posterior evaluative region. The executive region (areas 24 and 25, ACC) would control the output of visceromotor, endocrine, and skeletomotor systems, whereas the evaluative region (areas 29 and 30, RSC) would monitor the environment and play a role in memory (Vogt et al. 1992). This functional dichotomy was further supported by studies in humans, non-human primates, and rodents (Devinsky et al. 1995; Vogt et al. 1992). In attempting to explain this functional dichotomy, Brent Vogt and colleagues turned to the structural details of the MMC. Gene expression, cytoarchitecture (Vogt & Paxinos 2014), and connectivity studies suggested that the MMC is indeed composed of structurally different regions (ACC, MCC, and RSC), and these structural differences follow an anterior-posterior gradient compatible with the hypothesized anterior-posterior functional dichotomy. Connectivity studies never included, however, a systematic analysis of the HIPP-MMC connectivity. As HIPP plays a role in memory and spatial navigation, a difference in the HIPP-MMC connectivity could be a major cause for such functional dichotomy. Crucially, an executive region would need 'ready to use' contextual information, whereas an evaluative region, capable of monitor the environment and form memories, would need denser input of contextual information.

Our retrograde tracing studies showed that different levels of the MMC receive monosynaptic projections from different hippocampal compartments. Specifically, anterior levels of the MMC are mainly targeted by hippocampal populations located in diHIPP and vHIPP, whereas posterior levels of the MMC are mainly targeted by hippocampal populations from diHIPP and dHIPP. The hippocampal neurons projecting to the MMC follow, therefore, a dorso-ventral gradient, and their axons are distributed in the MMC in a posterior-anterior gradient. The gradient's complexity is further increased due to differences in the hippocampal populations targeting each MMC level. Crucially, anterior levels of the MMC are mainly targeted by hippocampal populations located in SP, presumably excitatory cells, whereas posterior levels of the MMC are targeted by both

pyramidal, presumably excitatory cells, and non-pyramidal cells, including LRIP interneurons from the border between SR and SLM.

The structural gradients described fully support Vogt's hypothesis, and provide a crucial structural explanation for the functional dichotomy observed in MMC. RSC receives inputs from all hippocampal *strata*, and possibly such input is closer to a copy of the information processed therein, something consistent with RSC neurons responding to visual-spatial variables necessary for contextual memory processing, and to such neurons exhibiting HIPP-like place selectivity. Conversely, ACC receives hippocampal input exclusively from pyramidal neurons, whose stronger behavioral correlate is the animal's position in space. This suggests that ACC privileges a 'ready to use' spatial map in the service of behavioral control, while the RSC accesses, and processes, a more complete version of the hippocampal activity. The observation that ACC, contrarily to RSC, receives significant input from vHIPP further strengths ACC's executive nature as vHIPP encodes non-spatial variables. Conversely, RSC receives significant input from dHIPP, where the encoding of spatial variables is more prominent.

While previous tracing studies in HIPP and parts of the MMC already suggested the existence of a dorso-ventral gradient in HIPP matching a posterior-anterior gradient in the MMC, the present study has many novel aspects. First, this study was the first to analyze HIPP-MMC connectivity systematically, thus including all the MMC levels. Second, this anatomical study was quantitative, rather than just qualitative, offering the first quantitative description of the gradients reported. Third, diHIPP was the major source of input to all MMC levels, contrarily to previous studies showing that ACC receives the densest input from vHIPP and RSC from dHIPP. Fourth, this study was the first to show differences in the laminar distribution and in the types of hippocampal neurons projecting to different MMC levels. The use of new fluorophores and more sensitive imaging systems combined with variability during the injections could explain differences in our results compared with previous works. This idea is strengthened by the observation that our data match the results from more recent anatomical studies in rodents. Since the hippocampal populations targeting the MMC seem to be sparse, the use of viral-based retrograde tracers is a valuable option. While viral-based retrograde tracers were not commercially available, we confirmed our results using a non-selective retrograde virus rAAV2-retro-tdTomato (Tervo et al. 2016) acquired through a recent collaboration.

2. RSC is targeted by LRIP interneurons located at the border between SR and SLM

While the structural gradient we report is enough to produce differences in the information reaching different MMC levels, our observations also suggest differences in the mechanism by which such information is transferred to and processed in anterior and posterior MMC divisions. Previous studies identified multiple classes of LRIP interneurons connecting the HIPP, SUB, medial septum, EC, and crucially, the RSC, with each population showing specific cell markers, specific laminar distribution within the HIPP, and specific correlations with the ongoing hippocampal oscillations. Optogenetic stimulation of LRIP interneurons in HIPP (and EC) increased sub- and supra-threshold θ-oscillations in post-synaptic neurons located in EC (and HIPP), suggesting that LRIP interneurons contribute to LFP coherence between brain regions, a standard biomarker of interregional communication and information transfer in the brain. By acting on coherence, LRIP interneurons could, theoretically, affect the efficacy of synaptic transmission, as high coherence epochs are associated with increased synaptic efficacy, whereas low coherence epochs are associated with less effective synaptic transmission, for instance, by increasing the likelihood of an action potential reaching a neuron during the refractory period.

Previous studies have shown that RSC has prominent θ-oscillations, and increased HIPP-RSC coherence in the θ-frequency was reported in behavioral tasks requiring contextual information, such as contextual fear conditioning, but the mechanism by which coherence is triggered remains elusive. While additional experiments would be required, our observation that RSC is targeted by LRIP interneurons located at the border between SR and SLM provides a candidate population, likely capable of triggering such coherence. Interestingly, hippocampal LRIP interneurons targeting RSC show θ modulation as their firing rate strongly increases during hippocampal θ-oscillations. Conversely, anterior MMC levels are not targeted by any hippocampal population of LRIP interneurons.

While previous studies have already shown the existence of this population of LRIP interneurons targeting RSC, our results show, for the first time, that such finding is not a ubiquitous feature among all hippocampal targets. To our knowledge, only major hippocampal partners, like SUB, medial septum, EC, RSC, but not ACC, receive long-range

excitatory and inhibitory inputs from HIPP. If LRIP interneurons facilitate coherence between HIPP and its target regions, an alternative mechanism should be responsible for the HIPP-ACC coherence also reported in behavioral tasks requiring contextual information, such as contextual fear conditioning and SWM tasks involving spatial sequences. As such LRIP interneurons seem restricted to the hippocampal formation and retro-hippocampal regions, regions known to play a role in contextual memory and spatial navigation, another hypothesis is that LRIP interneurons are involved in the mechanism(s) underlying spatial information processing in the hippocampal formation and retro-hippocampal regions, including the RSC.

3. The laminar distribution of hippocampal axons targeting MMC follows a topographical gradient

The hippocampal axons conveyed to different MMC levels arise from distinct hippocampal compartments and neural populations, but also reach different cortical layers, targeting distinct post-synaptic populations. Posterior MMC levels receive a denser and layer-specific excitatory input from HIPP directed to the superficial layers, most prominently to layer 3, thus reaching excitatory neurons, specifically fusiform pyramids, small and medium pyramids, and the apical tufts from pyramidal cells, and inhibitory local interneurons, specifically multipolar cells and bitufted cells. Paired with the excitatory input, axons from LRIP interneurons located at the border between SR and SLM also innervate superficial layers in RSC, most prominently layer 1 and layers 2-3, reaching excitatory and inhibitory post-synaptic targets presumably similar to the excitatory hippocampal axons. Whether the excitatory and inhibitory axons innervate similar neural populations and cell compartments, and whether these two projections interact requires further studies. Conversely, anterior MMC levels receive sparse, diffuse, and exclusively excitatory input from HIPP, targeting pyramids, parvalbumin-positive interneurons, and presumably other neural populations. The hippocampal axons targeting MMC follow, therefore, a posterior-anterior gradient, in which a dense, dual (excitatory/inhibitory) and

layer-specific projection is progressively converted in a sparse, excitatory, and diffuse projection. The progressive transition occurs around -1 mm from bregma in MCC. These observations suggest that hippocampal information integrates cingulate and retrosplenial computations at different levels. RSC receives hippocampal information mainly at superficial layers (layer 1 to 3), where most corticocortical afferents, efferents and computations occur, consistent with the notion of continuous feedback and functional proximity between RSC and HIPP, jointly processing and sharing contextual information in the service of contextual memory and spatial navigation. ACC, on the other hand, receives sparse and diffuse hippocampal input with stronger potentials evoked in layer 5, where large pyramids project descending axons to the striatum and other subcortical structures, consistent with an executive function and behavior control.

While previous tracing studies already suggested that hippocampal axons targeting the MMC follow an anterior-posterior gradient, the present study introduced novel aspects. First, this study was quantitative, rather than just qualitative, offering the first quantitative description of the gradient reported. Second, neuronal tracing was carried out using a virally-expressed anterograde tracer and more sensitive imaging systems, possibly explaining the increased numbers of LATB reported in this study, and the additional sparse labeling found in layers not referred by previous authors, particularly in ACC and MMC. Despite the novel aspects, our approach has limitations that should be considered. Commercial viral constructs with interneuron-specific promoters and transgenic rats expressing Cre recombinase under the control of interneuron-specific genes are not available, making the specific neuronal tracing of GABAergic projections to the RSC impossible to accomplish directly. An alternative strategy was necessary, specifically the expression of mCherry using a pan-neuronal promoter. The results were further compared with the labeling of hippocampal excitatory projections produced by mCherry under control of the CamKIIa promoter. Hippocampal axons labeled by the pan-neuronal construct and not replicated by the CamKIIa construct were considered putative GABAergic projections from LRIP interneurons, and were tested indirectly using anti-GAD antibodies. The absence of rats expressing Cre recombinase under control of specific hippocampal genes also hindered the possibility of restricting mCherry expression to specific hippocampal compartments, causing viral expression in diHIPP, dHIPP and dorsal SUB.

4. Hippocampal axons evoke extracellular potentials in MMC and their spatiotemporal dynamic follows a topographical gradient

Our findings show that distinct MMC levels receive axons from specific hippocampal compartments and the axons are organized in characteristic lamination patterns depending on the MMC level targeted. Specific stimulation of hippocampal axons evoked post-synaptic extracellular potentials in all MMC levels, both in superficial and deep layers, proving for the first time the existence of functional hippocampal synapses onto the neural populations of the MMC. Crucially, the patterns of evoked extracellular potentials matched the laminar distribution of LATB reported in the previous section, leading to differences in the spatiotemporal properties of the evoked extracellular potentials between anterior and posterior levels of the MMC. RSC showed evoked excitatory and inhibitory post-synaptic potentials with significantly higher slope and amplitude in superficial layers compared to deep layers, as predicted from our anterograde data showing denser targeting of superficial layers by hippocampal LATB conveyed by excitatory cells and LRIP interneurons. ACC, on the other hand, showed evoked EPSP with higher amplitude and slope in deep layers compared to superficial layers as deeper layers contain more sparsely targeted cells, despite the absence of layer-specificity in the HIPP-ACC projection. These differences are the first evidence that the topographical gradients found in this work translate into functional differences at the microcircuit level.

While previous *in vitro* studies performed recordings in divisions of the MMC, the present work introduced crucial aspects never attempted before. First, our work took advantage of optogenetic tools to ensure reversible and specific stimulation of the hippocampal projections targeting the MMC, a technical aspect never achieved by previous studies which used unspecific, electrical stimulation, hindering their ability to unequivocally prove the existence of functional synapses between HIPP and MMC. Second, our study took advantage of a system designed for high-throughput *in vitro* extracellular recordings in acute cortical slices to simultaneously record the evoked extracellular potentials at multiple sites per slice, providing the first characterization of the spatiotemporal dynamics of the responses evoked in MMC under hippocampal stimulation.

Despite these technical improvements, the approach used in the present study as limitations and assumptions that require attention. Sequential pharmacological incubations and linear subtraction of traces are standard strategies used to isolate specific components of extracellular responses (Hass CA, 2016), but this technique disregards non-linear effects. Even though linearity was an assumption when we computed the synaptic responses, excitatory responses, and inhibitory responses, we do not predict any negative impact in our results since we never attempted to isolate the response generated by a specific conductance. A second crucial assumption in our work was that $GABA_A$, kainate, AMPA, and NMDA receptors are the major non-artificial receptors generating the conductances responsible for the extracellular potentials recorded in MMC, as suggested by previous electrophysiological recordings from our lab (unpublished data), in which electrically-evoked extracellular potentials in MMC were completely inhibited under PTX, CNQX, and APV. Under these assumptions, pharmacological incubations and subtractions were used to evaluate whether the responses recorded were biological rather than artifacts, to isolate the contribution of ChR2 in each trace, and to isolate the excitatory and inhibitory components in the experiments using the CAG virus. Despite these manipulations, the evoked extracellular potentials were hard to interpret at the microcircuit level, a common limitation reported when *in vitro* electrophysiology is performed in cortical rather than hippocampal slices. Since neurons in MMC organize in complex anatomical patterns rather than the parallel arrangement reported in HIPP, interference and averaging of dipoles with diverse orientations produced complex waveforms with variable polarities hard to solve and attribute to specific microcircuit events. A particularly curious observation was the match between the polarities of the inhibitory responses and excitatory responses described when we performed MEA with the CAG virus. We could either be recordings systematically positive going potentials due to neuronal hyperpolarization, local positive potentials corresponding to disinhibition via interneuron-interneuron connections (preserved in our *in vitro* system), or remote negative potentials. A conservative explanation is that, once local excitation (and feedforward inhibition) is suppressed due to CNQX and APV, the non-blocked remote inhibition originated in HIPP long range projections would generate an active source corresponding to local, cortical hyperpolarization.

5. *In vivo* hippocampal-triggered MMC neural activity is consistent with the presence of diverse monosynaptic connectivity between HIPP and distinct levels of MMC

Our findings show that the spontaneous activity patterns in the HIPP and MMC in the awake-behaving rat follow what would be expected from the above-described connectivity. First, epochs of increased spiking from HIPP, are accompanied by short-term increases in MMC areas, with increased levels generally preceding and following the trigger point, indicative of complex time-dependent cross-talk between these regions (Jadhav et al. 2016; Kay et al. 2016; Yu et al. 2017; Remondes & Wilson 2015). Second, such increases are somewhat stronger in the anteriormost regions of MMC, something also apparent from LFP data analyzed in a similar manner, implying that the presence of LRIP interneurons in parallel with excitatory hippocampal inputs modulates RSC cortical responses *in vivo*. Our in vivo data further show that MMC responses to hippocampal spikes have an oscillatory component favoring frequencies known to play a significant role in hippocampal-cortical functions (Bieri et al. 2014; Buzsáki & Moser 2013; Colgin & Moser 2010; Engel & Fries 2010; O'Keefe 1993; Zheng & Colgin 2015). Contrary to the HIPP-triggered increase in cortical firing rate, the strength of oscillatory alignment to the hippocampal rhythms increases gradually along the MMC divisions, with the posteriormost RSC regions significantly more engaged to the hippocampal oscillations, which is consistent with RSC receiving denser hippocampal input, from all hippocampal layers, both excitatory and inhibitory. This is especially relevant since inhibitory inputs have widely been considered the main effectors of gamma oscillations and long-range gamma synchrony (Chen et al. 2017; Mann & Paulsen 2007; Paulsen & Moser 1998; Traub et al. 1996; Jinno et al. 2007), namely during SWM-dependent behaviors (Abbas et al. 2018). The fact that RSC receives long-range excitatory and inhibitory inputs from all hippocampal *strata*, matched by enhanced HIPP-RSC synchrony, is again consistent with the notion of continuous feedback and functional proximity between RSC and HIPP. These differences are the first evidence that the topographical gradients found in this work translate into functional differences *in vivo*, in freely-behaving rats.

While previous *in vivo* studies performed recordings in divisions of the MMC and in the HIPP, the present work introduced crucial aspects never attempted before. First, we

performed systematic recordings across the MMC, an essential aspect when looking for gradients and particularly when the structural boundaries of each MMC division are still debatable. Second, we recorded simultaneously from the HIPP and MMC (ACC, MCC, and RSC) in a SWM task, a technical achievement *per se*, made possible by the SLIQ drive with 32 independently movable tetrodes. Third, we performed the recordings while inhibiting the HIPP-MMC projections through expression of DREADDs in the HIPP.

Despite our technical achievements, the *in vivo* findings reported here resulted from a limited number of animals (n = 2 rats) and correspond to a preliminary analysis of the data collected. The three last aims of the dissertation (see *Aims*) are, therefore, unfinished, since we did not analyze the data at different stages of the DNMTP task (encoding, maintenance, and retrieval) and, more importantly, we did not show data concerning the MMC activity under hippocampal inhibition, both due to time and technical constraints. In order to analyze the neural activity at different stages of the DNMTP task and during DREADD-mediated hippocampal inhibition, we would need more animals and a better coverage of the maze in terms of single units. Even though the three last aims remain unfinished, the present dissertation provided the very first data on the DNMTP task (with and without DREADD-mediated hippocampal inhibition) and allowed protocol optimization in the lab. Future work will include the re-analysis of the data following the rationale established in the aims, replication of the *in vivo* recordings, and replication of the DREADD experiment, something that is ongoing in the lab.

As a final remark, and since we hypothesize the necessity of the HIPP-MMC interaction for SWM, it would be important to discuss a major limitation in our DREADD-based approach. The ideal experiment to address whether the HIPP-MMC interaction is necessary for SWM would require expressing an inhibitory DREADD or optogenetic tool in the HIPP, while implanting a CNO-delivering cannula or an optic fiber, respectively, in the MMC. By doing so, we would specifically target the HIPP-MMC projection, but the remaining HIPP and hippocampal projections would be preserved, avoiding confounders caused by inhibition of the whole HIPP. Equipment and technical constraints prevented us from performing this experiment, which is inherently difficult due to the extension of the MMC, requiring the putative implantation of several cannulas or optic fibers to effectively inhibit the HIPP-MMC projections. Alternatively, small-volume injections of a retrograde virus encoding an inhibitory DREADD or optogenetic tool across the MMC, followed by

implantation of a CNO-delivering cannula or optic fiber in the HIPP would avoid the use of several cannulas or fibers, but such vectors are not commercially available. Other Cre-based approaches could provide elegant ways to test our hypothesis, but they are only available in the mouse model. Irrespectively of the strategy, this ideal experiment imposes major challenges, for which we still do not have an effective solution.

VII

Conclusion

VII. CONCLUSION

SWM, the retention and use of behaviorally relevant spatial cues on a timescale of seconds, depends on complex, finely tuned interactions between HIPP and the cortical regions ACC and RSC, together hereby named MMC. In this circuit, the processing of hippocampal contextual information is hypothesized to follow a directional stream, from HIPP to cortex, providing depolarizing drive to MMC neurons. The functional circuitry underlying these interactions and the necessity of such interactions for SWM have not been established.

Using retrograde and anterograde tracings, we reported the existence of HIPP-MMC monosynaptic connections, and we characterized their topographic organization along the MMC. Our results provide anatomical support to distinct functional proximity between either ACC and RSC, and the HIPP. While the full extent of MMC receives monosynaptic inputs from diHIPP, each region of MMC receives distinct hippocampal inputs with diverse layer distributions. The HIPP-RSC projection includes glutamatergic axons conveyed by pyramidal and non-pyramidal neurons, which converge onto RSC superficial layers (L1-L4), and GABAergic axons conveyed by LRIP interneurons located at the SR-SLM border, which target RSC L1. RSC receives, therefore, stronger hippocampal input originating from all hippocampal *strata*, something reflected in their functional interdependence and coding properties, wherein RSC neurons exhibit significant activity changes in response to hippocampal lesions (Albasser et al. 2007), responds to visual-spatial variables required for contextual memory processing, and displays HIPP-like place selectivity (Mao et al. 2017). RSC would thus be a close hippocampal partner, contributing to spatial mapping. Conversely, the HIPP-ACC projection does not show layer specificity in ACC and only contains glutamatergic axons conveyed by pyramidal neurons from diHIPP, whose strongest behavioral correlate is the animal's position, required for task space coding and behavioral control, consistently with previous *in vivo* studies (Remondes & Wilson 2013; Remondes & Wilson 2015; Yu & Frank 2014). The distinct anatomical connectivity of ACC and RSC with HIPP is intermediated by the one with MCC which includes aspects of both.

Using multi-electrode *in vitro* electrophysiology combined with optogenetics and sequential pharmacology, we isolated significant synaptic responses on all the divisions of the MMC in response to stimulation of hippocampal terminals, and found that such responses are sensitive to selective AMPA, NMDA and $GABA_A$ channel blockers, like *bona fide* synapses, and also that the distribution of thus-analyzed responses is consistent with the abovementioned anatomical distribution of hippocampal axons at each MMC level.

Our results bring new light to an old controversy. Previous studies suggest the absence of dHIPP inputs onto CG (Jay & Witter 1991), others their presence (Lee A. Cenquizca & Swanson 2007), and also that most hippocampal projections towards RSC reportedly originate in the contiguous dorsal subiculum or from neurons in the CA1-subiculum border (van Groen & Wyss 1990; van Groen & Wyss 1992; van Groen & Wyss 2003; Lee A. Cenquizca & Swanson 2007). By systematically analyzing HIPP-MMC connectivity, we now present a quantitative account of hippocampal inputs to MMC divisions. We show that HIPP and MMC are indeed connected directly by a population of neurons from diHIPP, following a posterior-anterior gradient in which a dense, dual (excitatory/inhibitory) and layer-specific projection is progressively converted in a sparse, excitatory, and diffuse projection. These observations suggest that hippocampal activity informs CG and RSC computations at different levels. RSC receives multi-layer hippocampal inputs mainly in its superficial layers (L1-L4), where it sends and receives most corticocortical connections, and CG is targeted exclusively by pyramidal neurons with stronger potentials evoked in L5 whose large pyramids project descending axons to the striatum and other subcortical structures, consistent with executive functions and behavior control.

By using *in vivo* multi-site recordings of both neuronal spikes and LFP, we have shown that the spontaneous activity patterns in the HIPP and MMC in the awake-behaving rat follow what would be expected from the above-described connectivity. First, epochs of increased spiking from HIPP, are accompanied by short-term increases in MMC areas, with increased levels generally preceding and following the trigger point, indicative of complex time-dependent cross-talk between these regions (Jadhav et al. 2016; Kay et al. 2016; Yu et al. 2017; Remondes & Wilson 2015). Second, such increases are somewhat stronger in the anteriormost regions of MMC, something also apparent from LFP data analyzed in a similar manner, implying that the presence of LRIP interneurons in parallel with excitatory hippocampal inputs modulates RSC cortical responses *in vivo*. Our in vivo

data further show that MMC responses to hippocampal spikes have an oscillatory component favoring frequencies known to play a significant role in hippocampal-cortical functions (Bieri et al. 2014; Buzsáki & Moser 2013; Colgin & Moser 2010; Engel & Fries 2010; O'Keefe 1993; Zheng & Colgin 2015). Contrary to the HIPP-triggered increase in cortical firing rate, the strength of oscillatory alignment to the hippocampal rhythms increases gradually along the MMC divisions, with the posteriormost RSC regions significantly more engaged to the hippocampal oscillations, which is consistent with RSC receiving denser hippocampal input, from all hippocampal layers, both excitatory and inhibitory. This is especially relevant since inhibitory inputs have widely been considered the main effectors of gamma oscillations and long-range gamma synchrony (Chen et al. 2017; Mann & Paulsen 2007; Paulsen & Moser 1998; Traub et al. 1996; Jinno et al. 2007), namely during SWM-dependent behaviors (Abbas et al. 2018). The fact that RSC receives long-range excitatory and inhibitory inputs from all hippocampal *strata*, matched by enhanced HIPP-RSC synchrony, is again consistent with the notion of continuous feedback and functional proximity between RSC and HIPP. Conversely, more diffuse hippocampal inputs to GC, with stronger potentials around L5, would result in stronger responses guiding downstream executive behaviors via large pyramidal neural projections to the basal ganglia.

Time and technical constraints prevented us from fully achieving all aims proposed in the present dissertation, particularly in terms of *in vivo* recordings. Such obstacles hindered us from addressing the necessity of the HIPP-MMC interaction for SWM. Having in mind our unfinished work and the new questions brought about by the findings presented here, an immediate follow-up of this dissertation would include:

1. Replication of the *in vivo* recordings with and without DREADD-mediated hippocampal inhibition; *(ongoing work)*
2. Correlating the activity of the HIPP and MMC in the encoding, maintenance, and retrieval phases of the DNMTP task, in order to establish the temporal window for the interaction during SWM; *(ongoing work)*
3. Expanding the analysis to include single unit data; *(ongoing work)*

4. Addressing the necessity of the HIPP-MMC interaction for SWM through DREADD-mediated hippocampal inhibition in the DNMTP task; *(ongoing work)*
5. Refining the DREADD-mediated hippocampal inhibition to target specifically the HIPP-MMC projections by local CNO infusion in MMC, using one or more cannulas implanted in MMC.

In a long-term perspective, our DREADD-based approach would evolve to an optogenetic-based approach (see *Discussion*), consisting on hippocampal inhibition triggered by optic fibers implanted in MMC, following hippocampal expression of an inhibitory optogenetic tool. Such setup would allow reversible and online inhibition of the HIPP-MMC projection, providing a system to test additional questions, including:

1. The temporal window of the HIPP-MMC interaction in SWM, by online inhibiting the HIPP-MMC projections at different epochs of the DNMTP task;
2. The effect of hippocampal activity patterns in MMC coding properties, by online inhibiting the HIPP-MMC projections depending on hippocampal rhythms, for instance during SWR;
3. The role of LRIP interneurons targeting RSC, by online inhibiting these neurons following expression of an inhibitory optogenetic tool restricted to hippocampal GABAergic neurons.

VIII

References

VIII. REFERENCES

Abbas, A.I. et al., 2018. Somatostatin Interneurons Facilitate Hippocampal-Prefrontal Synchrony and Prefrontal Spatial Encoding. *Neuron*, 100(4), p.926–939.e3.

Albasser, M.M. et al., 2007. Hippocampal lesions halve immediate-early gene protein counts in retrosplenial cortex: distal dysfunctions in a spatial memory system. *European Journal of Neuroscience*, 26(5), pp.1254–1266.

Alexander, A.S. & Nitz, D.A., 2015. Retrosplenial cortex maps the conjunction of internal and external spaces. *Nature neuroscience*, 18(8), pp.1143–1151.

Amaral, D.G. & Witter, M.P., 1989. The three-dimensional organization of the hippocampal formation: a review of anatomical data. *Neuroscience*, 31(3), pp.571–91.

Andersen, P., 2007. *The hippocampus book*, Oxford University Press.

Auger, S.D., Zeidman, P. & Maguire, E.A., 2017. Efficacy of navigation may be influenced by retrosplenial cortex-mediated learning of landmark stability. *Neuropsychologia*, 104, pp.102–112.

Belluscio, M.A. et al., 2012. Cross-Frequency Phase-Phase Coupling between Theta and Gamma Oscillations in the Hippocampus. *Journal of Neuroscience*, 32(2), pp.423–435.

Bieri, K.W., Bobbitt, K.N. & Colgin, L.L., 2014. Slow and Fast Gamma Rhythms Coordinate Different Spatial Coding Modes in Hippocampal Place Cells. *Neuron*, 82(3), pp.670–681.

Brockmann, M.D. et al., 2011. Coupled oscillations mediate directed interactions between prefrontal cortex and hippocampus of the neonatal rat. *Neuron*, 71(2), pp.332–47.

Bubb, E.J., Kinnavane, L. & Aggleton, J.P., 2017. Hippocampal–diencephalic–cingulate networks for memory and emotion: An anatomical guide. *Brain and Neuroscience Advances*, 1(1), p.239821281772344.

Buckley, M.J. & Mitchell, A.S., 2016. Retrosplenial Cortical Contributions to Anterograde and Retrograde Memory in the Monkey. *Cerebral Cortex*, 26(6), pp.2905–2918.

Burgess, N., Maguire, E.A. & O'Keefe, J., 2002. The human hippocampus and spatial and episodic memory. *Neuron*, 35(4), pp.625–41.

Bush, Luu & Posner, 2000. Cognitive and emotional influences in anterior cingulate cortex. *Trends in cognitive sciences*, 4(6), pp.215–222.

Buzsáki, G., 2015. Hippocampal sharp wave-ripple: A cognitive biomarker for episodic memory and planning. *Hippocampus*, 25(10), pp.1073–1188.

Buzsáki, G., 2004. Large-scale recording of neuronal ensembles. *Nature Neuroscience*, 7(5), pp.446–451.

Buzsáki, G., 2006. *Rhythms of the brain*, Oxford University Press.

Buzsáki, G., 2002. Theta Oscillations in the Hippocampus. *Neuron*, 33(3), pp.325–340.

Buzsáki, G., Anastassiou, C.A. & Koch, C., 2012. The origin of extracellular fields and currents — EEG, ECoG, LFP and spikes. *Nature Reviews Neuroscience*, 13(6), pp.407–420.

Buzsáki, G. & Moser, E.I., 2013. Memory, navigation and theta rhythm in the hippocampal-entorhinal system. *Nature Neuroscience*, 16(2), pp.130–138.

Buzsáki, G. & Wang, X.-J., 2012. Mechanisms of Gamma Oscillations. *Annual Review of Neuroscience*, 35(1), pp.203–225.

Cabral, H.O. et al., 2014. Oscillatory Dynamics and Place Field Maps Reflect Hippocampal Ensemble Processing of Sequence and Place Memory under NMDA Receptor Control. *Neuron*, 81(2), pp.402–415.

Caracheo, B.F. et al., 2013. Abrupt changes in the patterns and complexity of anterior cingulate cortex activity when food is introduced into an environment. *Frontiers in Neuroscience*, 7, p.74.

Cenquizca, L.A. & Swanson, L.W., 2007. Spatial organization of direct hippocampal field CA1 axonal projections to the rest of the cerebral cortex. *Brain research reviews*, 56(1), pp.1–26.

Cenquizca, L.A. & Swanson, L.W., 2007. Spatial organization of direct hippocampal field CA1 axonal projections to the rest of the cerebral cortex. *Brain Research Reviews*, 56(1), pp.1–26.

Chen, G. et al., 2017. Distinct Inhibitory Circuits Orchestrate Cortical beta and gamma Band Oscillations. *Neuron*, 96(6), p.1403–1418.e6.

Chersi, F. & Burgess, N., 2015. The Cognitive Architecture of Spatial Navigation: Hippocampal and Striatal Contributions. *Neuron*, 88(1), pp.64–77.

Clark, B.J. et al., 2010. Impaired head direction cell representation in the anterodorsal thalamus after lesions of the retrosplenial cortex. *The Journal of neuroscience : the official journal of the Society for Neuroscience*, 30(15), pp.5289–302.

Colgin, L.L. et al., 2009. Frequency of gamma oscillations routes flow of information in the hippocampus. *Nature*, 462(7271), pp.353–357.

Colgin, L.L., 2016. Rhythms of the hippocampal network. *Nature Reviews Neuroscience*, 17(4), pp.239–249.

Colgin, L.L. & Moser, E.I., 2010. Gamma Oscillations in the Hippocampus. *Physiology*, 25(5), pp.319–329.

Conte, W.L., Kamishina, H. & Reep, R.L., 2009. Multiple neuroanatomical tract-tracing using fluorescent Alexa Fluor conjugates of cholera toxin subunit B in rats. *Nature Protocols*, 4(8), pp.1157–1166.

Corcoran, K.A. et al., 2016. Analysis of coherent activity between retrosplenial cortex, hippocampus, thalamus, and anterior cingulate cortex during retrieval of recent and remote context fear memory. *Neurobiology of Learning and Memory*, 127, pp.93–101.

Cowen, S.L., Davis, G.A. & Nitz, D.A., 2012. Anterior cingulate neurons in the rat map anticipated effort and reward to their associated action sequences. *Journal of Neurophysiology*, 107(9), pp.2393–2407.

Davidson, T.J., Kloosterman, F. & Wilson, M.A., 2009. Hippocampal Replay of Extended

Experience. *Neuron*, 63(4), pp.497–507.

Dégenètais, E. et al., 2003. Synaptic influence of hippocampus on pyramidal cells of the rat prefrontal cortex: an in vivo intracellular recording study. *Cerebral cortex (New York, N.Y. : 1991)*, 13(7), pp.782–92.

Deisseroth, K. & Hegemann, P., 2017. The form and function of channelrhodopsin. *Science*, 357(6356), p.eaan5544.

Devinsky, O., Morrell, M.J. & Vogt, B.A., 1995. Contributions of anterior cingulate cortex to behaviour. *Brain : a journal of neurology*, 118 (Pt 1, pp.279–306.

Doeller, C.F., King, J.A. & Burgess, N., 2008. Parallel striatal and hippocampal systems for landmarks and boundaries in spatial memory. *Proceedings of the National Academy of Sciences*, 105(15), pp.5915–5920.

Dolan, R.J. & Dayan, P., 2013. Goals and habits in the brain. *Neuron*, 80(2), pp.312–25.

Dong, H.-W. et al., 2009. Genomic–anatomic evidence for distinct functional domains in hippocampal field CA1. *Proceedings of the National Academy of Sciences*, 106(28), pp.11794–11799.

Dragoi, G. & Buzsáki, G., 2006. Temporal Encoding of Place Sequences by Hippocampal Cell Assemblies. *Neuron*, 50(1), pp.145–157.

Dudchenko, P.A., 2004. An overview of the tasks used to test working memory in rodents. *Neuroscience & Biobehavioral Reviews*, 28(7), pp.699–709.

Ego-Stengel, V. & Wilson, M.A., 2009. Disruption of ripple-associated hippocampal activity during rest impairs spatial learning in the rat. *Hippocampus*, 20(1), p.NA-NA.

Eichenbaum, H., 2014. Time cells in the hippocampus: a new dimension for mapping memories. *Nature reviews. Neuroscience*, 15(11), pp.732–44.

Eichenbaum, H. & Cohen, N.J., 2014. Can We Reconcile the Declarative Memory and Spatial Navigation Views on Hippocampal Function? *Neuron*, 83(4), pp.764–770.

Ekstrom, A.D. et al., 2003. Cellular networks underlying human spatial navigation. *Nature*, 425(6954), pp.184–8.

Engel, A.K. & Fries, P., 2010. Beta-band oscillations—signalling the status quo? *Current Opinion in Neurobiology*, 20(2), pp.156–165.

Fanselow, M.S. & Dong, H.-W., 2010. Are the Dorsal and Ventral Hippocampus Functionally Distinct Structures? *Neuron*, 65(1), pp.7–19.

Fenno, L., Yizhar, O. & Deisseroth, K., 2011. The Development and Application of Optogenetics. *Annual Review of Neuroscience*, 34(1), pp.389–412.

Fillinger, C. et al., 2017. Afferents to anterior cingulate areas 24a and 24b and midcingulate areas 24a' and 24b' in the mouse. *Brain Structure and Function*, 222(3), pp.1509–1532.

Finch, D.M., Derian, E.L. & Babb, T.L., 1984. Afferent fibers to rat cingulate cortex. *Experimental neurology*, 83(3), pp.468–85.

Foster, D.J. & Knierim, J.J., 2012. Sequence learning and the role of the hippocampus in rodent navigation. *Current opinion in neurobiology*, 22(2), pp.294–300.

Foster, D.J. & Wilson, M.A., 2007. Hippocampal theta sequences. *Hippocampus*, 17(11), pp.1093–1099.

Freund, T.F. & Buzsáki, G., 1996. Interneurons of the hippocampus. *Hippocampus*, 6(4), pp.347–470.

Friedel, E. et al., 2014. Devaluation and sequential decisions: linking goal-directed and model-based behavior. *Frontiers in human neuroscience*, 8, p.587.

Gigg, J., Tan, A.M. & Finch, D.M., 1994. Glutamatergic hippocampal formation projections to prefrontal cortex in the rat are regulated by GABAergic inhibition and show convergence with glutamatergic projections from the limbic thalamus. *Hippocampus*, 4(2), pp.189–198.

Gray, C.M. et al., 1995. Tetrodes markedly improve the reliability and yield of multiple

single-unit isolation from multi-unit recordings in cat striate cortex. *Journal of neuroscience methods*, 63(1–2), pp.43–54.

van Groen, T. & Wyss, J.M., 1992. Connections of the retrosplenial dysgranular cortex in the rat. *The Journal of comparative neurology*, 315(2), pp.200–16.

van Groen, T. & Wyss, J.M., 1990. Connections of the retrosplenial granular a cortex in the rat. *The Journal of comparative neurology*, 300(4), pp.593–606.

van Groen, T. & Wyss, J.M., 2003. Connections of the retrosplenial granular b cortex in the rat. *The Journal of comparative neurology*, 463(3), pp.249–63.

Hallock, H.L. et al., 2013. Dissociable roles of the dorsal striatum and dorsal hippocampus in conditional discrimination and spatial alternation T-maze tasks. *Neurobiology of Learning and Memory*, 100, pp.108–116.

Hass, C.A. & Glickfeld, L.L., 2016. High-fidelity optical excitation of cortico-cortical projections at physiological frequencies. *Journal of Neurophysiology*, 116(5), pp.2056–2066.

Hayden, B.Y. & Platt, M.L., 2010. Neurons in anterior cingulate cortex multiplex information about reward and action. *The Journal of neuroscience : the official journal of the Society for Neuroscience*, 30(9), pp.3339–46.

Hedberg, T.G., Simpson, G. V & Stanton, P.K., 1993. Microcircuitry of posterior cingulate cortex in vitro: electrophysiology and laminar analysis using the current source density method. *Brain research*, 632(1–2), pp.239–48.

Hedberg, T.G. & Stanton, P.K., 1995. Long-term potentiation and depression of synaptic transmission in rat posterior cingulate cortex. *Brain research*, 670(2), pp.181–96.

Heilbronner, S.R. & Hayden, B.Y., 2016. Dorsal Anterior Cingulate Cortex: A Bottom-Up View. *Annual Review of Neuroscience*, 39(1), pp.149–170.

Hill, D.N., Mehta, S.B. & Kleinfeld, D., 2011. Quality Metrics to Accompany Spike Sorting of Extracellular Signals. *Journal of Neuroscience*, 31(24), pp.8699–8705.

Holroyd, C.B. & Yeung, N., 2012. Motivation of extended behaviors by anterior cingulate cortex. *Trends in Cognitive Sciences*, 16(2), pp.122–128.

Hoover, W.B. & Vertes, R.P., 2007. Anatomical analysis of afferent projections to the medial prefrontal cortex in the rat. *Brain Structure and Function*, 212(2), pp.149–179.

Horga, G. et al., 2015. Changes in corticostriatal connectivity during reinforcement learning in humans. *Human Brain Mapping*, 36(2), pp.793–803.

Hyman, J.M. et al., 2012. Contextual encoding by ensembles of medial prefrontal cortex neurons. *Proceedings of the National Academy of Sciences of the United States of America*, 109(13), pp.5086–91.

Iaria, G. et al., 2003. Cognitive strategies dependent on the hippocampus and caudate nucleus in human navigation: variability and change with practice. *The Journal of neuroscience : the official journal of the Society for Neuroscience*, 23(13), pp.5945–52.

Iaria, G. et al., 2007. Retrosplenial and hippocampal brain regions in human navigation: complementary functional contributions to the formation and use of cognitive maps. *European Journal of Neuroscience*, 25(3), pp.890–899.

Ishikawa, A. & Nakamura, S., 2003. Convergence and interaction of hippocampal and amygdalar projections within the prefrontal cortex in the rat. *The Journal of neuroscience : the official journal of the Society for Neuroscience*, 23(31), pp.9987–95.

Izaki, Y. et al., 2003. Differences between paired-pulse facilitation and long-term potentiation in the dorsal and ventral hippocampal CA1-prefrontal pathways of rats. *Brain research*, 992(1), pp.142–5.

Jacob, P.-Y. et al., 2017. An independent, landmark-dominated head-direction signal in dysgranular retrosplenial cortex. *Nature Neuroscience*, 20(2), pp.173–175.

Jadhav, S.P. et al., 2012. Awake Hippocampal Sharp-Wave Ripples Support Spatial Memory. *Science*, 336(6087), pp.1454–1458.

Jadhav, S.P. et al., 2016. Coordinated Excitation and Inhibition of Prefrontal Ensembles

during Awake Hippocampal Sharp-Wave Ripple Events. *Neuron*, 90(1), pp.113–127.

Jay, T.M., Burette, F. & Laroche, S., 1995. NMDA receptor-dependent long-term potentiation in the hippocampal afferent fibre system to the prefrontal cortex in the rat. *The European journal of neuroscience*, 7(2), pp.247–50.

Jay, T.M., Burette, F. & Laroche, S., 1996. Plasticity of the hippocampal-prefrontal cortex synapses. *Journal of physiology, Paris*, 90(5–6), pp.361–6.

Jay, T.M. & Witter, M.P., 1991. Distribution of hippocampal CA1 and subicular efferents in the prefrontal cortex of the rat studied by means of anterograde transport ofPhaseolus vulgaris-leucoagglutinin. *The Journal of Comparative Neurology*, 313(4), pp.574–586.

Jezek, K. et al., 2011. Theta-paced flickering between place-cell maps in the hippocampus. *Nature*, 478(7368), pp.246–249.

Jinno, S. et al., 2007. Neuronal diversity in GABAergic long-range projections from the hippocampus. *The Journal of neuroscience : the official journal of the Society for Neuroscience*, 27(33), pp.8790–804.

Jinno, S., 2009. Structural organization of long-range GABAergic projection system of the hippocampus. *Frontiers in neuroanatomy*, 3, p.13.

Johnson, A. & Redish, A.D., 2007. Neural Ensembles in CA3 Transiently Encode Paths Forward of the Animal at a Decision Point. *Journal of Neuroscience*, 27(45), pp.12176–12189.

Johnston, D. & Wu, S.M., 1995. *Foundations of cellular neurophysiology*, MIT Press.

Joo, H.R. & Frank, L.M., 2018. The hippocampal sharp wave–ripple in memory retrieval for immediate use and consolidation. *Nature Reviews Neuroscience*, 19(12), pp.744–757.

Karlsson, M.P. & Frank, L.M., 2009. Awake replay of remote experiences in the hippocampus. *Nature Neuroscience*, 12(7), pp.913–918.

Kay, K. et al., 2016. A hippocampal network for spatial coding during immobility and sleep. *Nature*, 531(7593), pp.185–190.

Keene, C.S. & Bucci, D.J., 2009. Damage to the retrosplenial cortex produces specific impairments in spatial working memory. *Neurobiology of learning and memory*, 91(4), pp.408–14.

Kemere, C. et al., 2013. Rapid and Continuous Modulation of Hippocampal Network State during Exploration of New Places C. T. Dickson, ed. *PLoS ONE*, 8(9), p.e73114.

Klausberger, T. & Somogyi, P., 2008. Neuronal Diversity and Temporal Dynamics: The Unity of Hippocampal Circuit Operations. *Science*, 321(5885), pp.53–57.

Kloosterman, F. et al., 2009. Micro-drive array for chronic in vivo recording: drive fabrication. *Journal of visualized experiments : JoVE*, (26).

Kudrimoti, H.S., Barnes, C.A. & McNaughton, B.L., 1999. Reactivation of hippocampal cell assemblies: effects of behavioral state, experience, and EEG dynamics. *The Journal of neuroscience : the official journal of the Society for Neuroscience*, 19(10), pp.4090–101.

Lapish, C.C. et al., 2008. Successful choice behavior is associated with distinct and coherent network states in anterior cingulate cortex. *Proceedings of the National Academy of Sciences of the United States of America*, 105(33), pp.11963–8.

Lapish, C.C. et al., 2008. Successful choice behavior is associated with distinct and coherent network states in anterior cingulate cortex. *Proceedings of the National Academy of Sciences*, 105(33), pp.11963–11968.

Laroche, S., Jay, T.M. & Thierry, A.M., 1990. Long-term potentiation in the prefrontal cortex following stimulation of the hippocampal CA1/subicular region. *Neuroscience letters*, 114(2), pp.184–90.

Lee, A.K. & Wilson, M.A., 2002. Memory of sequential experience in the hippocampus during slow wave sleep. *Neuron*, 36(6), pp.1183–94.

Lee, S.W., Shimojo, S. & O'Doherty, J.P., 2014. Neural Computations Underlying Arbitration between Model-Based and Model-free Learning. *Neuron*, 81(3), pp.687–699.

Liang, L. et al., 2017. Scalable, Lightweight, Integrated and Quick-to-Assemble (SLIQ)

Hyperdrives for Functional Circuit Dissection. *Frontiers in neural circuits*, 11, p.8.

Lin, J.Y., 2011. A user's guide to channelrhodopsin variants: features, limitations and future developments. *Experimental physiology*, 96(1), pp.19–25.

Lopes, G. et al., 2015. Bonsai: an event-based framework for processing and controlling data streams. *Frontiers in Neuroinformatics*, 9.

Lovett-Barron, M. & Losonczy, A., 2014. Behavioral consequences of GABAergic neuronal diversity. *Current Opinion in Neurobiology*, 26, pp.27–33.

Lu, Y.-F. et al., 2014. Spatial and temporal plasticity of synaptic organization in anterior cingulate cortex following peripheral inflammatory pain: multi-electrode array recordings in rats. *Neuroscience Bulletin*, 30(1), pp.1–20.

Luk, C.-H. & Wallis, J.D., 2013. Choice coding in frontal cortex during stimulus-guided or action-guided decision-making. *The Journal of neuroscience : the official journal of the Society for Neuroscience*, 33(5), pp.1864–71.

MacLaren, D.A.A. et al., 2016. Clozapine N-Oxide Administration Produces Behavioral Effects in Long-Evans Rats: Implications for Designing DREADD Experiments. *eNeuro*, 3(5).

Mann, E.O. & Paulsen, O., 2007. Role of GABAergic inhibition in hippocampal network oscillations. *Trends in Neurosciences*, 30(7), pp.343–349.

Manns, J.R. & Eichenbaum, H., 2009. A cognitive map for object memory in the hippocampus. *Learning & memory (Cold Spring Harbor, N.Y.)*, 16(10), pp.616–24.

Manvich, D.F. et al., 2018. The DREADD agonist clozapine N-oxide (CNO) is reverse-metabolized to clozapine and produces clozapine-like interoceptive stimulus effects in rats and mice. *Scientific Reports*, 8(1), p.3840.

Mao, D. et al., 2017. Sparse orthogonal population representation of spatial context in the retrosplenial cortex. *Nature Communications*, 8(1), p.243.

Mao, J.B. & Robinson, J.K., 1998. Microinjection of GABA-A agonist muscimol into the dorsal but not the ventral hippocampus impairs non-mnemonic measures of delayed non-

matching-to-position performance in rats. *Brain research*, 784(1–2), pp.139–47.

Maviel, T. et al., 2004. Sites of Neocortical Reorganization Critical for Remote Spatial Memory. *Science*, 305(5680), pp.96–99.

Mitchell, A.S. et al., 2018. Retrosplenial cortex and its role in spatial cognition. *Brain and Neuroscience Advances*, 2, p.239821281875709.

Miyashita, T. & Rockland, K.S., 2007. GABAergic projections from the hippocampus to the retrosplenial cortex in the rat. *The European journal of neuroscience*, 26(5), pp.1193–204.

Morecraft, R.J. & Van Hoesen, G.W., 1998. Convergence of limbic input to the cingulate motor cortex in the rhesus monkey. *Brain research bulletin*, 45(2), pp.209–32.

Morellini, F., 2013. Spatial memory tasks in rodents: what do they model? *Cell and Tissue Research*, 354(1), pp.273–286.

Morgenstern, N.A., Bourg, J. & Petreanu, L., 2016. Multilaminar networks of cortical neurons integrate common inputs from sensory thalamus. *Nature Neuroscience*, 19(8), pp.1034–1040.

Morris, R.G.M. et al., 1982. Place navigation impaired in rats with hippocampal lesions. *Nature*, 297(5868), pp.681–683.

Moser, M.-B. & Moser, E.I., 1998. Functional differentiation in the hippocampus. *Hippocampus*, 8(6), pp.608–619.

Muenzinger, K.F. & Gentry, E., 1931. Tone discrimination in white rats. *Journal of Comparative Psychology*, 12(2), pp.195–206.

Nádasdy, Z. et al., 1999. Replay and time compression of recurring spike sequences in the hippocampus. *The Journal of neuroscience : the official journal of the Society for Neuroscience*, 19(21), pp.9497–507.

Nagel, G. et al., 2003. Channelrhodopsin-2, a directly light-gated cation-selective membrane channel. *Proceedings of the National Academy of Sciences of the United States of America*, 100(24), pp.13940–5.

Nakamura, H., Katayama, Y. & Kawakami, Y., 2010. Hippocampal CA1/subiculum-prefrontal cortical pathways induce plastic changes of nociceptive responses in cingulate and prelimbic areas. *BMC neuroscience*, 11(1), p.100.

Neave, N. et al., 1994. Lack of effect of lesions in the anterior cingulate cortex and retrosplenial cortex on certain tests of spatial memory in the rat. *Behavioural brain research*, 65(1), pp.89–101.

Newman, E.L. et al., 2013. Cholinergic Blockade Reduces Theta-Gamma Phase Amplitude Coupling and Speed Modulation of Theta Frequency Consistent with Behavioral Effects on Encoding. *Journal of Neuroscience*, 33(50), pp.19635–19646.

Nguyen, D.P. et al., 2009. Micro-drive array for chronic in vivo recording: tetrode assembly. *Journal of Visualized Experiments*, (26).

de Nò, L., 1934. Studies on the Structure of the Cerebral Cortex II. Continuation of the Study of the Ammonic System. *Journal für Psychologie und Neurologie*, 46, pp.113–117.

Nonaka, M. et al., 2017. Everyday memory: towards a translationally effective method of modelling the encoding, forgetting and enhancement of memory. *European Journal of Neuroscience*, 46(4), pp.1937–1953.

Norman, D.A. & Shallice, T., 1986. Attention to Action. In *Consciousness and Self-Regulation*. Boston, MA: Springer US, pp. 1–18.

O'Keefe, J., 1979. A review of the hippocampal place cells. *Progress in neurobiology*, 13(4), pp.419–39.

O'Keefe, J., 1991. An allocentric spatial model for the hippocampal cognitive map. *Hippocampus*, 1(3), pp.230–235.

O'Keefe, J., 1993. Hippocampus, theta, and spatial memory. *Current Opinion in Neurobiology*, 3(6), pp.917–924.

O'Keefe, J., 1976. Place units in the hippocampus of the freely moving rat. *Experimental neurology*, 51(1), pp.78–109.

O'Keefe, J. & Conway, D.H., 1978. Hippocampal place units in the freely moving rat: why they fire where they fire. *Experimental brain research*, 31(4), pp.573–90.

O'Keefe, J. & Dostrovsky, J., 1971. The hippocampus as a spatial map. Preliminary evidence from unit activity in the freely-moving rat. *Brain research*, 34(1), pp.171–5.

O'Keefe, J. & Recce, M.L., 1993. Phase relationship between hippocampal place units and the EEG theta rhythm. *Hippocampus*, 3(3), pp.317–330.

Papez, J.W., 1937. A Proposed Mechanism of Emotion. *Archives of Neurology And Psychiatry*, 38(4), p.725.

Parslow, D.M. et al., 2005. Allocentric spatial memory in humans with hippocampal lesions. *Acta Psychologica*, 118(1–2), pp.123–147.

Paulsen, O. & Moser, E., 1998. A model of hippocampal memory encoding and retrieval: GABAergic control of synaptic plasticity. *Trends in Neurosciences*, 21(7), pp.273–278.

Paus, T., 2001. Primate anterior cingulate cortex: Where motor control, drive and cognition interface. *Nature Reviews Neuroscience*, 2(6), pp.417–424.

Paxinos, G., 2004. *The rat nervous system*, Elsevier Academic Press.

Paxinos, G. & Watson, C., 2006. *The Rat Brain in Stereotaxic Coordinates* 6th ed., Academic Press.

Penfield, W. & Milner, B., 1958. Memory Deficit Produced by Bilateral Lesions in the Hippocampal Zone. *Archives of Neurology And Psychiatry*, 79(5), p.475.

Pothuizen, H.H.J. et al., 2010. Effects of selective granular retrosplenial cortex lesions on spatial working memory in rats. *Behavioural Brain Research*, 208(2), pp.566–575.

Ragozzino, M.E., Adams, S. & Kesner, R.P., 1998. Differential involvement of the dorsal anterior cingulate and prelimbic-infralimbic areas of the rodent prefrontal cortex in spatial working memory. *Behavioral neuroscience*, 112(2), pp.293–303.

Ramadan, W., Eschenko, O. & Sara, S.J., 2009. Hippocampal Sharp Wave/Ripples during

Sleep for Consolidation of Associative Memory C. T. Dickson, ed. *PLoS ONE*, 4(8), p.e6697.

Ramón y Cajal, S., 1909. *Histologie du système nerveux de l'homme & des vertébrés.*, Paris : Maloine,.

Redish, A.D., 2013. *The mind within the brain : how we make decisions and how those decisions go wrong*,

Redish, A.D., 2016. Vicarious trial and error. *Nature Reviews Neuroscience*, 17(3), pp.147–159.

Remondes, M. & Wilson, M.A., 2013. Cingulate-hippocampus coherence and trajectory coding in a sequential choice task. *Neuron*, 80(5), pp.1277–89.

Remondes, M. & Wilson, M.A., 2015. Slow-γ Rhythms Coordinate Cingulate Cortical Responses to Hippocampal Sharp-Wave Ripples during Wakefulness. *Cell Reports*, 13(7), pp.1327–1335.

Reverberi, C., Görgen, K. & Haynes, J.-D., 2012. Compositionality of Rule Representations in Human Prefrontal Cortex. *Cerebral Cortex*, 22(6), pp.1237–1246.

Rombo, D.M. et al., 2016. Adenosine A_1 Receptor Suppresses Tonic $GABA_A$ Receptor Currents in Hippocampal Pyramidal Cells and in a Defined Subpopulation of Interneurons. *Cerebral Cortex*, 26(3), pp.1081–1095.

Rombo, D.M. et al., 2014. Synaptic mechanisms of adenosine A2A receptor-mediated hyperexcitability in the hippocampus. *Hippocampus*.

Roth, B.L., 2016. DREADDs for Neuroscientists. *Neuron*, 89(4), pp.683–94.

Ruediger, S. et al., 2012. Goal-oriented searching mediated by ventral hippocampus early in trial-and-error learning. *Nature Neuroscience*, 15(11), pp.1563–1571.

Rushworth, M.F.S. et al., 2011. Frontal Cortex and Reward-Guided Learning and Decision-Making. *Neuron*, 70(6), pp.1054–1069.

Schall, J.D., Stuphorn, V. & Brown, J.W., 2002. Monitoring and control of action by the

frontal lobes. *Neuron*, 36(2), pp.309–22.

Schomburg, E.W. et al., 2014. Theta Phase Segregation of Input-Specific Gamma Patterns in Entorhinal-Hippocampal Networks. *Neuron*, 84(2), pp.470–485.

Scoville, W.B. & Milner, B., 1957. Loss of recent memory after bilateral hippocampal lesions. *Journal of neurology, neurosurgery, and psychiatry*, 20(1), pp.11–21.

Siegle, J.H. et al., 2017. Open Ephys: an open-source, plugin-based platform for multichannel electrophysiology. *Journal of Neural Engineering*, 14(4), p.045003.

Skaggs, W.E. et al., 1996. Theta phase precession in hippocampal neuronal populations and the compression of temporal sequences. *Hippocampus*, 6(2), pp.149–172.

Squire, L.R., 2004. Memory systems of the brain: A brief history and current perspective. *Neurobiology of Learning and Memory*, 82(3), pp.171–177.

Squire, L.R., 2009. The legacy of patient H.M. for neuroscience. *Neuron*, 61(1), pp.6–9.

Takita, M. et al., 1999. Induction of stable long-term depression in vivo in the hippocampal-prefrontal cortex pathway. *The European journal of neuroscience*, 11(11), pp.4145–8.

Tanaka, K.Z. et al., 2018. The hippocampal engram maps experience but not place. *Science*, 361(6400), pp.392–397.

Tavares, R.M. et al., 2015. A Map for Social Navigation in the Human Brain. *Neuron*, 87(1), pp.231–243.

Temido-Ferreira, M. et al., 2018. Age-related shift in LTD is dependent on neuronal adenosine A2A receptors interplay with mGluR5 and NMDA receptors. *Molecular Psychiatry*.

Tervo, D.G.R. et al., 2016. A Designer AAV Variant Permits Efficient Retrograde Access to Projection Neurons. *Neuron*, 92(2), pp.372–382.

Teyler, T.J. & DiScenna, P., 1986. The hippocampal memory indexing theory. *Behavioral*

neuroscience, 100(2), pp.147–54.

Teyler, T.J. & Rudy, J.W., 2007. The hippocampal indexing theory and episodic memory: Updating the index. *Hippocampus*, 17(12), pp.1158–1169.

Thomas, C.A. et al., 1972. A miniature microelectrode array to monitor the bioelectric activity of cultured cells. *Experimental cell research*, 74(1), pp.61–6.

Tierney, P.L. et al., 2004. Influence of the hippocampus on interneurons of the rat prefrontal cortex. *The European journal of neuroscience*, 20(2), pp.514–24.

Tolman, E.C., 1948. Cognitive maps in rats and men. *Psychological review*, 55(4), pp.189–208.

Tolman, E.C., 1939. Prediction of vicarious trial and error by means of the schematic sowbug. *Psychological Review*, 46(4), pp.318–336.

Traub, R.D. et al., 1996. A mechanism for generation of long-range synchronous fast oscillations in the cortex. *Nature*, 383(6601), pp.621–624.

Vann, S.D. & Aggleton, J.P., 2005. Selective dysgranular retrosplenial cortex lesions in rats disrupt allocentric performance of the radial-arm maze task. *Behavioral Neuroscience*, 119(6), pp.1682–1686.

Vann, S.D., Aggleton, J.P. & Maguire, E.A., 2009. What does the retrosplenial cortex do? *Nature reviews. Neuroscience*, 10(11), pp.792–802.

Vann, S.D., Aggleton, J.P. & Maguire, E.A., 2009. What does the retrosplenial cortex do? *Nature Reviews Neuroscience*, 10(11), pp.792–802.

Varela, C. et al., 2014. Anatomical substrates for direct interactions between hippocampus, medial prefrontal cortex, and the thalamic nucleus reuniens. *Brain structure & function*, 219(3), pp.911–29.

Vogt, B.A., Finch, D.M. & Olson, C.R., 1992. Functional heterogeneity in cingulate cortex: the anterior executive and posterior evaluative regions. *Cerebral cortex (New York, N.Y. : 1991)*, 2(6), pp.435–43.

Vogt, B.A. & Gabriel, M. eds., 1993. *Neurobiology of Cingulate Cortex and Limbic Thalamus*, Boston, MA: Birkhäuser Boston.

Vogt, B.A. & Paxinos, G., 2014. Cytoarchitecture of mouse and rat cingulate cortex with human homologies. *Brain Structure and Function*, 219(1), pp.185–192.

Vogt, B.A. & Peters, A., 1981. Form and distribution of neurons in rat cingulate cortex: Areas 32, 24, and 29. *The Journal of Comparative Neurology*, 195(4), pp.603–625.

Voon, V. et al., 2017. Model-Based Control in Dimensional Psychiatry. *Biological Psychiatry*, 82(6), pp.391–400.

Wang, Y. et al., 2015. Theta sequences are essential for internally generated hippocampal firing fields. *Nature Neuroscience*, 18(2), pp.282–288.

Wirt, R. & Hyman, J., 2017. Integrating Spatial Working Memory and Remote Memory: Interactions between the Medial Prefrontal Cortex and Hippocampus. *Brain Sciences*, 7(12), p.43.

Yamamoto, J. et al., 2014. Successful Execution of Working Memory Linked to Synchronized High-Frequency Gamma Oscillations. *Cell*, 157(4), pp.845–857.

Yamamoto, J. & Tonegawa, S., 2017. Direct Medial Entorhinal Cortex Input to Hippocampal CA1 Is Crucial for Extended Quiet Awake Replay. *Neuron*, 96(1), p.217–227.e4.

Young, C.K., Mcnaughton, N. & Canada, T.N., 2009. Coupling of Theta Oscillations between Anterior and Posterior Midline Cortex and with the Hippocampus in Freely Behaving Rats. , (January), pp.24–40.

Yu, J.Y. et al., 2017. Distinct hippocampal-cortical memory representations for experiences associated with movement versus immobility. *eLife*, 6.

Yu, J.Y. & Frank, L.M., 2014. Hippocampal-cortical interaction in decision making. *Neurobiology of learning and memory*, 117, pp.34–41.

Zheng, C. & Colgin, L.L., 2015. Beta and Gamma Rhythms Go with the Flow. *Neuron*, 85(2),

pp.236–237.

Zhu, H. & Roth, B.L., 2014. Silencing synapses with DREADDs. *Neuron*, 82(4), pp.723–5.

IX

Supplementary Material

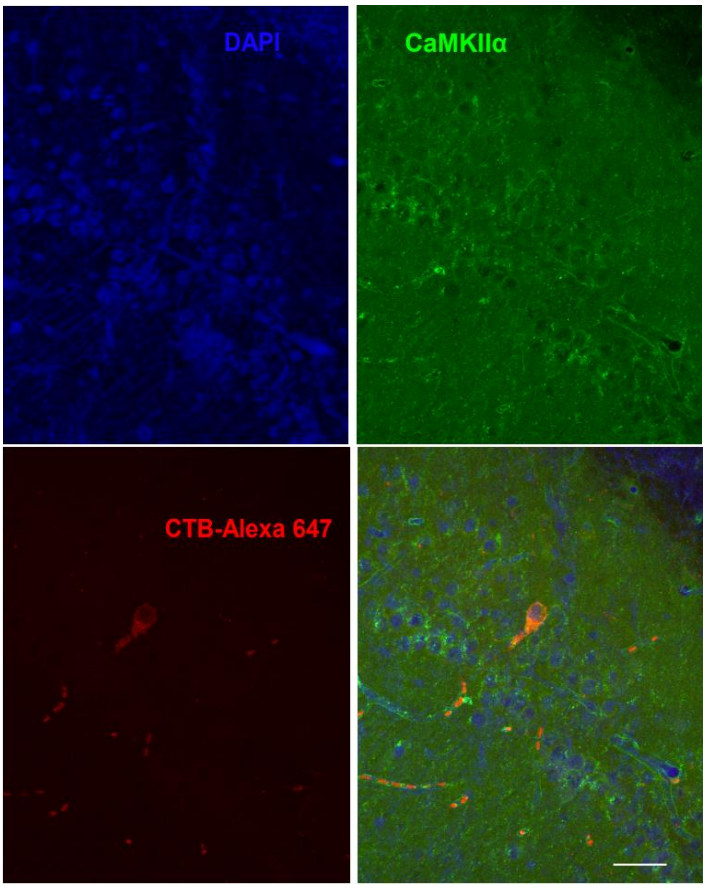

Figure 31 - CaMKIIa positive neuron in *stratum pyramidale* labeled after injection of CTB-Alexa 647 in RSC. Scale bar: 50 µm.

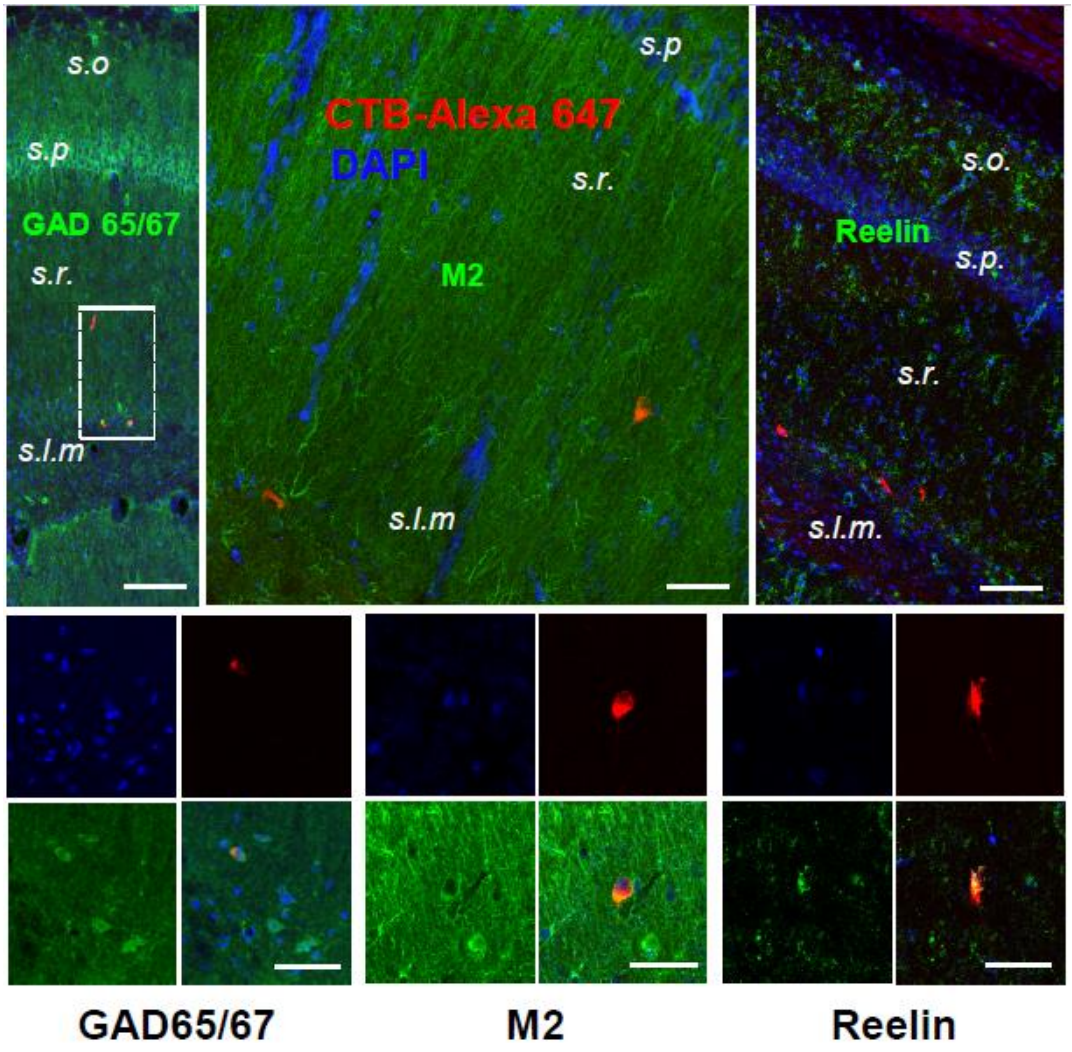

Figure 32 – LRIP interneurons located at the border between SR and SLM. Injection of CTB-Alexa 647 in the RSC labeled neurons testing positive for GAD65/67 (55.5%), M2 (80.5%), and Reelin (13.8%), restricted to the SR-SLM. Example slices in the top panels, labeled accordingly: CTB-Alexa 647 in red; GAD65/67, M2, or Reelin in green; DAPI in blue. One illustrative blown-up double-positive neuron of each class is depicted in the bottom sets of four arranged sub-panels, also labeled accordingly. Scale bars: 50 µm.

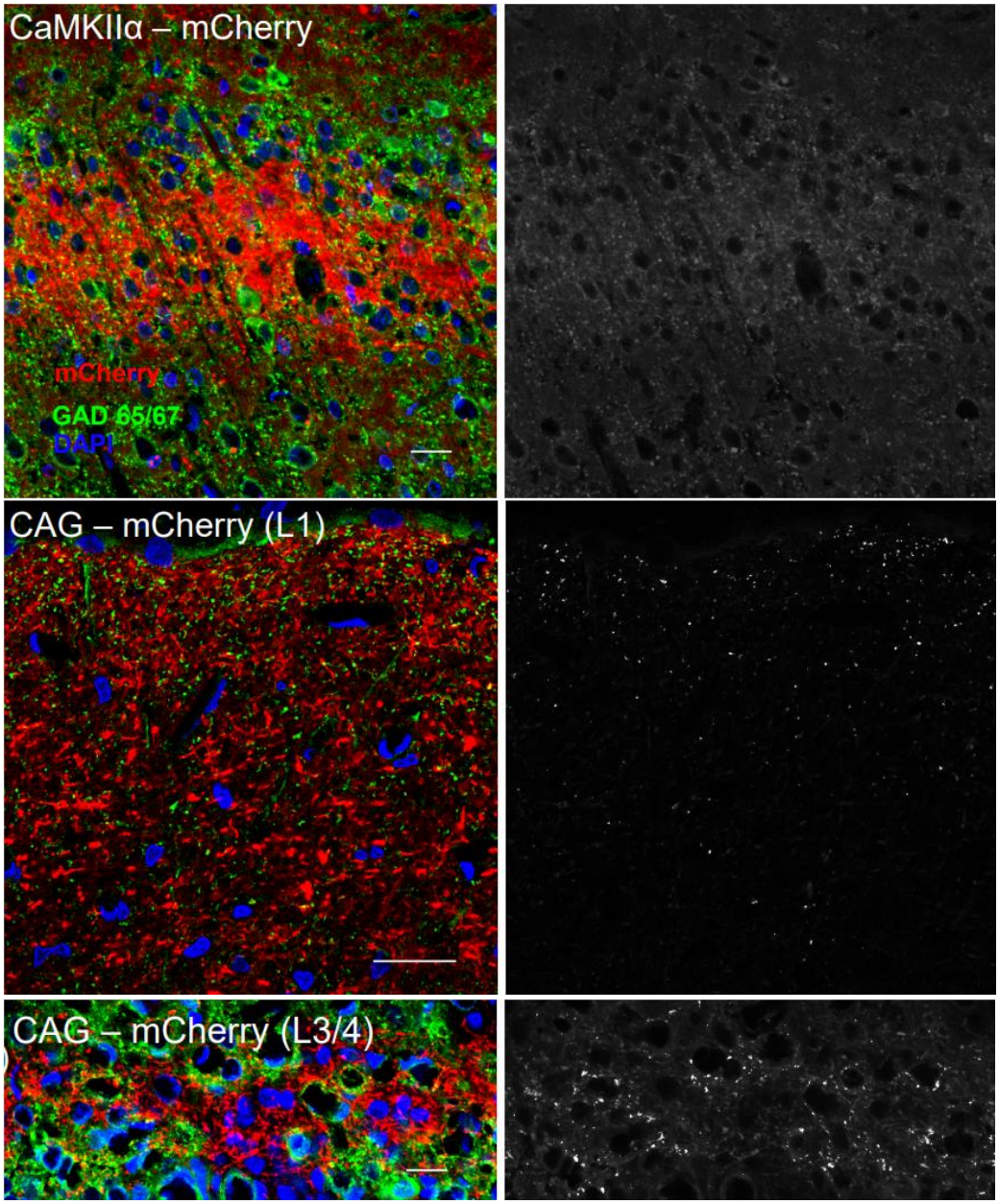

Figure 33 – GAD positive hippocampal axon terminals in RSC. GAD positive puncta in RSC significantly colocalize with mCherry labeled hippocampal axon terminals, only if mCherry is driven by CAG and not if driven by CaMKIIa, strongly suggesting that these are of inhibitory nature (please see Supplementary Material, Table 6, gray scales are panel-specific). Top, Single plane confocal picture from one example rat showing mCherry positive hippocampal axons expressed under CaMKIIa promoter (left), and the corresponding colocalization map (right). No co-occurring objects were identified, nor significant colocalization. Middle and bottom, Single plane confocal pictures from example RSC slices showing mCherry positive hippocampal axons in L1 (middle) and L3/4 (bottom) expressed under CAG promoter (left), and the corresponding colocalization map (right). Co-occurring objects are identified as white dots on the right panel. Scale bars: 20 µm.

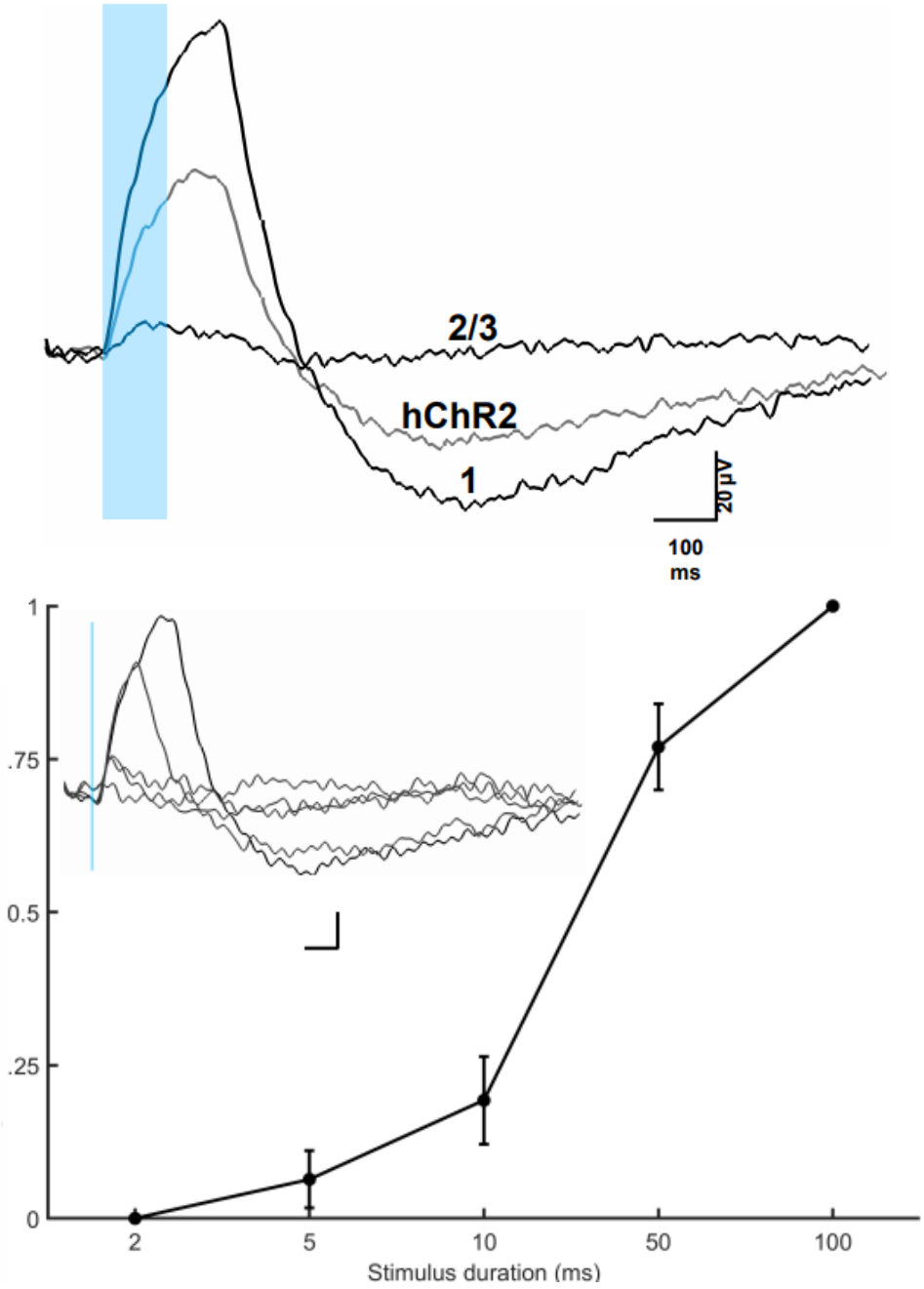

Figure 34 – In vitro electrophysiology control experiments and I/O analysis. Top, MEA response (labeled "hChR2") and controls. To validate the extracellular potentials recorded, 3 controls were performed. Trace 1, "Photoelectric Artifact", was produced by direct illumination of the MEA array. This artifact could only be evoked with the LED placed in close proximity to the contacts. Trace 2/3, "Negative Control", is the response obtained using a slice rendered non-viable by keeping it in aCSF for 120 minn, without oxygenation. Such slices were unable to produce extracellular potentials, but also prevented photoelectric artifacts. An equivalent trace was obtained by stimulating a viable slice infected with hChR2, responsive to blue light, but with a green LED, supporting the specificity of hChR2 responses to blue light. All negative controls were refractory to the action of the drugs used in the main experiments. Bottom, I/O analysis. Normalized amplitude of the extracellular potentials evoked with light pulses of 2, 5, 10, 50, and 100 ms (n = 3 rats). Inset, Light-evoked extracellular potentials from an example MMC slice stimulated with blue light, delivered in single pulses with increasing durations (2, 5, 10, 50, and 100 ms). The vertical blue line and bar mark the stimulus onset and duration, respectively; scale bar as in top panel. Error bars are SD.

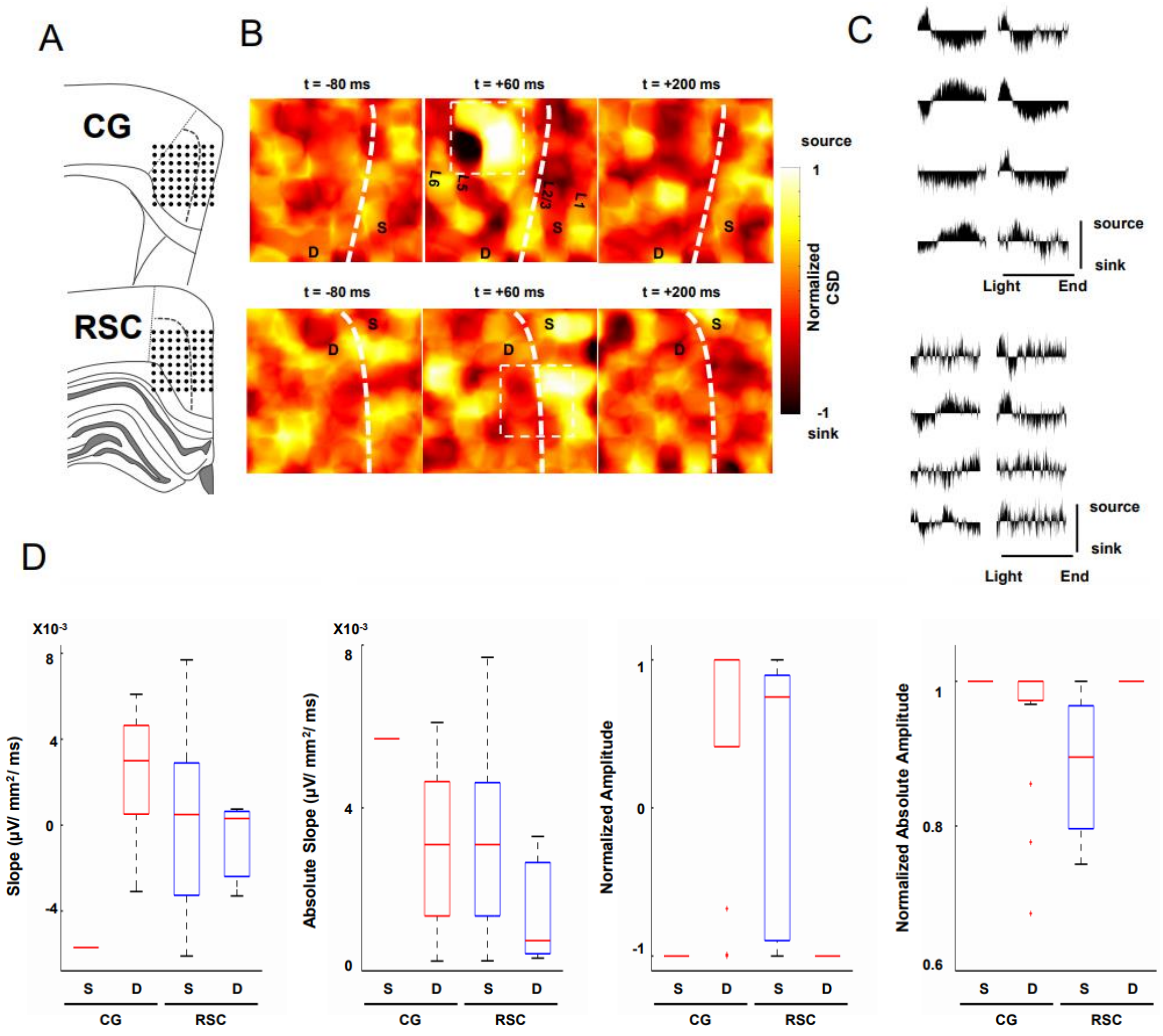

Figure 35 – In vitro electrophysiology: current source density analysis (CSD) performed on the data corresponding to Figure 22. (A-B) Representative example of the sources and sinks evoked in the CG (top) and in RSC (bottom). Heatmaps show the CSD distribution before, at the onset, and after the onset of stimulation. (C) CSD profiles (from light onset to the end of the experiment) in the contacts highlighted by a white square in panel B. (D) Boxplots summarize slope, absolute slope, amplitude, and absolute amplitude computed from the CSD profiles as depicted in panel C (4 rats per brain region). Note the predominance of sink-source pairs in deeper CG layers and superficial RSC layers, reflected in an MMC region-by-cortical layer interaction in both the slope (p=0.0272) and amplitude (p=0.0137) of the normalized CSD (N-way ANOVA, n = 8rats), in agreement with voltage results presented in the main figure.

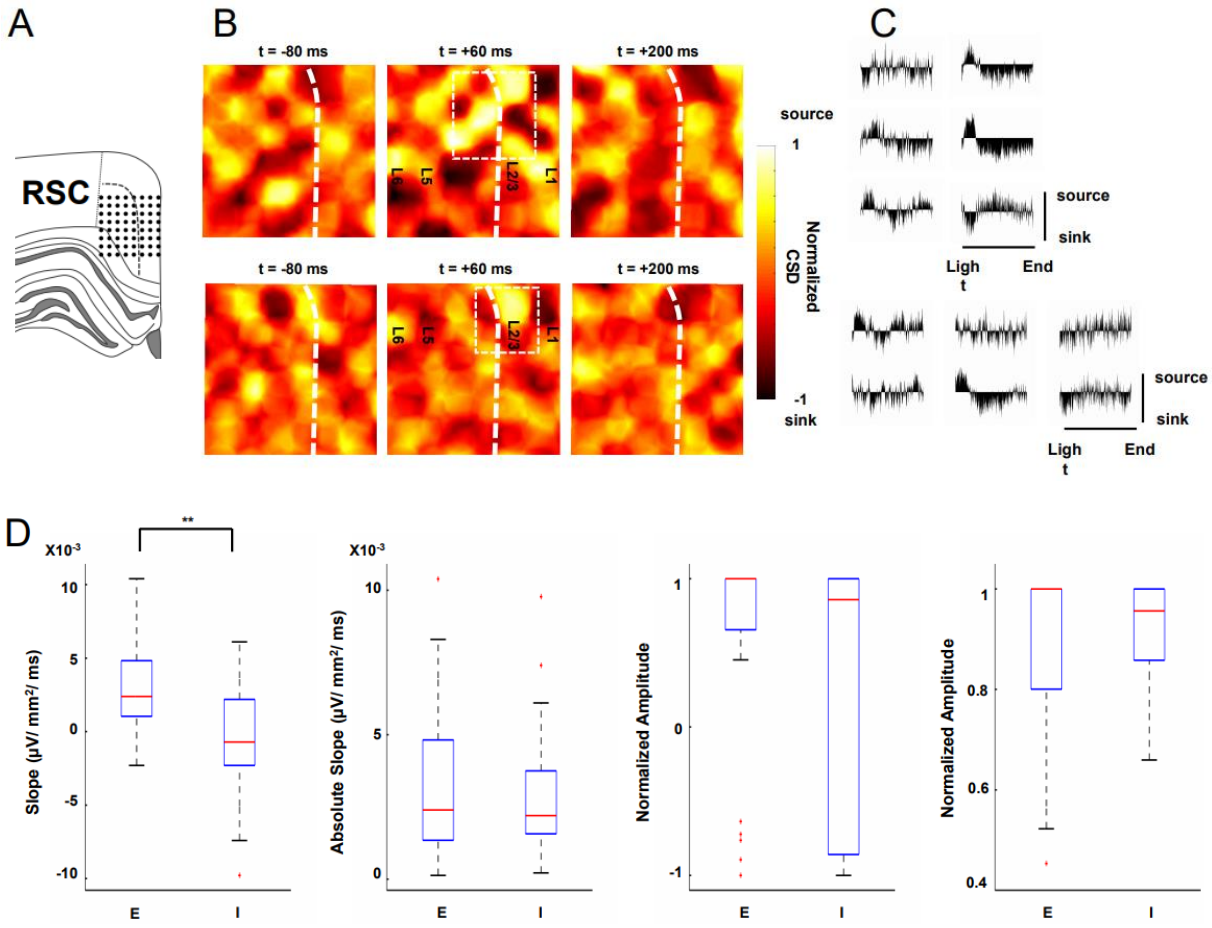

Figure 36 – In vitro electrophysiology: current source density analysis (CSD) performed on the data corresponding to Figure 24. (A-B) Representative example of the sources and sinks evoked in RSC. Heatmaps show the CSD distribution before, at the onset, and after the onset of stimulation. (C) CSD profiles (from light onset to the end of the experiment) in the contacts highlighted by a white square in panel B. (D) Boxplots summarize slope, absolute slope, amplitude, and absolute amplitude computed from the CSD profiles as depicted in panel C (n = 3 rats). Note the predominance of sink-source pairs in superficial RSC layers, and significantly higher slope of excitatory currents (**p<0.01; Wilcoxon signed rank test).

Table 6 - Colocalization analysis.

Layers	tM GAD	Th mCherry	th GAD	r<th
1 (n = 3)	0.47 ± 0.17	6.44 ± 2.51	41.11 ± 40.16	0.005 ± 0.016
3/4 (n = 3)	0.10 ± 0.08	92.44 ± 121.93	8.44 ± 2.83	0.001 ± 0.006
5 (n = 3)	≈0	<0	<0	-

tM, thresholded Mander's split colocalization coefficient; Th, Costes' threshold; r<th, correlation below the Costes' threshold.

Metrics' explanation:

- Thresholded Mander's split colocalization coefficient (tM): Indicates the proportion of signal in that channel (the GAD channel) that colocalizes with the other channel (the CTB channel). Zero is no colocalization, one means perfect colocalization.

- Costes' threshold (Th): Method of auto threshold determination. This method uses an iterative procedure to determine what pair of thresholds for the 2 channels gives a Pearson's correlation coefficient of zero for the pixels below such thresholds. All pixels which have intensities above the two thresholds have greater than zero correlation. Pixels below the thresholds have no correlation or anti-correlation.

- Correlation below the threshold (r<Th): It is computed together with the Costes' threshold. It is the Pearson's correlation coefficient for the pixels below the threshold defined by the Costes' method. It should be zero (no correlation) or negative (anti-correlation).